Springer ThesesRecognizing Outstanding Ph.D. Research

Kai Hermann Scherer

Grating-Based X-Ray Phase-Contrast Mammography



Springer Theses

Recognizing Outstanding Ph.D. Research

Aims and Scope

The series "Springer Theses" brings together a selection of the very best Ph.D. theses from around the world and across the physical sciences. Nominated and endorsed by two recognized specialists, each published volume has been selected for its scientific excellence and the high impact of its contents for the pertinent field of research. For greater accessibility to non-specialists, the published versions include an extended introduction, as well as a foreword by the student's supervisor explaining the special relevance of the work for the field. As a whole, the series will provide a valuable resource both for newcomers to the research fields described, and for other scientists seeking detailed background information on special questions. Finally, it provides an accredited documentation of the valuable contributions made by today's younger generation of scientists.

Theses are accepted into the series by invited nomination only and must fulfill all of the following criteria

- They must be written in good English.
- The topic should fall within the confines of Chemistry, Physics, Earth Sciences, Engineering and related interdisciplinary fields such as Materials, Nanoscience, Chemical Engineering, Complex Systems and Biophysics.
- The work reported in the thesis must represent a significant scientific advance.
- If the thesis includes previously published material, permission to reproduce this must be gained from the respective copyright holder.
- They must have been examined and passed during the 12 months prior to nomination.
- Each thesis should include a foreword by the supervisor outlining the significance of its content.
- The theses should have a clearly defined structure including an introduction accessible to scientists not expert in that particular field.

More information about this series at http://www.springer.com/series/8790

Kai Hermann Scherer

Grating-Based X-Ray Phase-Contrast Mammography

Doctoral Thesis accepted by the Technical University of Munich, Germany



Author
Dr. Kai Hermann Scherer
Department of Physics, Institute of Medical Engineering
Technical University of Munich
Garching
Germany

Supervisor
Prof. Franz Pfeiffer
Department of Physics, Institute of Medical
Engineering
Technical University of Munich
Garching
Germany

ISSN 2190-5053 ISSN 2190-5061 (electronic) Springer Theses ISBN 978-3-319-39536-4 ISBN 978-3-319-39537-1 (eBook) DOI 10.1007/978-3-319-39537-1

Library of Congress Control Number: 2016941093

© Springer International Publishing Switzerland 2016

This work is subject to copyright. All rights are reserved by the Publisher, whether the whole or part of the material is concerned, specifically the rights of translation, reprinting, reuse of illustrations, recitation, broadcasting, reproduction on microfilms or in any other physical way, and transmission or information storage and retrieval, electronic adaptation, computer software, or by similar or dissimilar methodology now known or hereafter developed.

The use of general descriptive names, registered names, trademarks, service marks, etc. in this publication does not imply, even in the absence of a specific statement, that such names are exempt from the relevant protective laws and regulations and therefore free for general use.

The publisher, the authors and the editors are safe to assume that the advice and information in this book are believed to be true and accurate at the date of publication. Neither the publisher nor the authors or the editors give a warranty, express or implied, with respect to the material contained herein or for any errors or omissions that may have been made.

Printed on acid-free paper

This Springer imprint is published by Springer Nature The registered company is Springer International Publishing AG Switzerland

Publications and Scientific Presentations

First-authored publications (peer-reviewed)

Scherer, K., Birnbacher, L., Chabior, M., Herzen, J., Mayr, D., Grandl, S., Sztrókay-Gaul, A., Hellerhoff, K., Bamberg, F. & Pfeiffer, F. Bi-directional X-ray phase-contrast mammography. *PLoS One* **9**, e93502 (2014). Available: http://journals.plos.org/plosone/article?id=10.1371/journal.pone.0093502

Scherer, K., Braig, E., Willer, K., Willner, M., Fingerle, A., Chabior, M., Herzen, J., Eiber, M., Haller, B., Straub, M., Schneider, H., Rummeny, E., Noël, P. & Pfeiffer, F. Non-invasive differentiation of kidney stone types using X-ray dark-field radiography. *Sci. Rep.* **5**, 9527 (2015). Available: http://www.nature.com/srep/2015/150409/srep09527/full/srep09527.html

Scherer, K., Willer, K., Gromann, L., Birnbacher, L., Braig, E., Grandl, S., Sztrókay-Gaul, A., Herzen, J., Mayr, D., Hellerhoff, K. & Pfeiffer, F. Toward clinically compatible phase-contrast mammography. *PLoS One* **10**, e0130776 (2015). Available: http://journals.plos.org/plosone/article?id=10.1371/journal.pone. 0130776

Scherer, K., Braig, E., Schock, J., Birnbacher, L., Chabior, M., Herzen, J., Mayr, D., Grandl, S., Sztrókay-Gaul, A., Hellerhoff, K. & Pfeiffer, F. Improved mammography diagnostics by assessing the micromorphology of breast calcifications via X-Ray dark-field radiography. *Sci. Rep.* [To be submitted].

Equally-contributed publications (peer-reviewed)

Grandl, S., <u>Scherer, K.</u>, Sztrókay-Gaul, A., Birnbacher, L., Willer, K., Chabior, M., Herzen, J., Mayr, D., Auweter, S., Pfeiffer, F., Bamberg, F. & Hellerhoff, K. Improved visualization of breast cancer features in multifocal carcinoma using phase-contrast and dark-field mammography—an ex-vivo study. *Eur. Radiol.* **25**, 3659–68 (2015). Available: http://link.springer.com/article/10.1007%2Fs00330-015-3773-5

Communications Arising (peer-reviewed)

Scherer, K., Birnbacher, L., Willer, K., Braig, E., Chabior, M., Herzen, J. & Pfeiffer, F. Correct quantitative evaluation of X-ray dark-field images for microcalcification analysis in mammography. *Nat. Commun.* **5**, 10863 (2016).

Co-authored publications (peer-reviewed)

Auweter, S., Herzen, J., Willner, M., Grandl, S., <u>Scherer, K.</u>, Bamberg, F., Reiser, F., Pfeiffer, F. & Hellerhoff, K. X-ray phase-contrast imaging of the breast-advances towards clinical implementation. *Br. J. Radiol.* **87**, 20130606 (2014). Available: http://www.ncbi.nlm.nih.gov/pmc/articles/PMC4064551

Matias Di Martino, J., Flores, J., Pfeiffer, F., Scherer, K., Ayubi, G. & Ferrari, A. Phase retrieval from one partial derivative. *Opt. Lett.* **38**, 4813–4816 (2013). Available: http://www.ncbi.nlm.nih.gov/pubmed/24322139

Co-authored publications (non-reviewed)

Auweter, S., Scherer, K., Pfeiffer, F. & Schirmer, T. Volkskrankheiten fest im Blick. *Technik in Bayern* **02/15**, 6–7 (2015)

Oral presentations

X-ray phase-contrast mammography—a case-study. 2nd International Workshop on X-ray and Neutron Phase Imaging with Gratings (XNPIG) and 3rd Symposium on Biomedical Phase-Contrast Imaging (IMXP), Garmisch-Partenkirchen, Germany, January 2014.

Assessment of breast microcalcifications via X-ray dark-field radiography. 4rd Symposium on Biomedical Phase-Contrast Imaging (IMXP), Garmisch-Partenkirchen, Germany, January 2015.

Poster presentations

A compact Talbot-Lau interferometer for mammography. 2rd Symposium on Biomedical Phase-Contrast Imaging (IMXP), Garmisch-Partenkirchen, Germany, January 2013.



Abstract

Phase-contrast and dark-field imaging utilizing Talbot-Lau interferometry is a novel and promising approach to provide radiologists with a strongly enhanced soft-tissue contrast in medical diagnostics. Especially in the case of mammography, conventional absorption-based imaging suffers from an inherently poor contrast, which results in high recall and unsatisfying cancer detection rates, most noticeably among young patients. The ultimate goal of this thesis is to answer the question whether phase-contrast mammography can address these shortcomings, while being applied to routine breast screening. Therefore, a compact phase-contrast mammography setup was specifically designed within a laboratory environment, where the retrieval of full-field mammograms is practicable. By means of a case study that investigated un-fixated breast abladates, we demonstrate that phase-contrast mammography in comparison to standard examination provides a significantly enhanced detection quality of tumor strands, lesion borders, and small nodules. Further, we propose dark-field mammography as an in vivo tool for the assessment of breast microcalcification, with the purpose of reducing the number of unnecessary invasive procedures. Moreover, we verify clinical compatibility of phase-contrast mammography, by presenting the very first dose-compatible phase-contrast mammograms of a freshly dissected, cancerous mastectomy specimen at a medically meaningful sample compression. Finally, we demonstrate that dark-field radiography is well suited for the differentiation of renal stones as well as detection of radiolucent calculi. Based on the results presented here, we are fully convinced that phase-contrast mammography has the potential to complement conventional screening and that the development of a clinical scanner should hence be of highest priority.

Supervisor's Foreword

Since the discovery of X-rays in the year 1895 by Wilhelm Conrad Röntgen, X-ray imaging has been an indispensable tool in medical diagnostics, and ranges from simple radiography applications to advanced CT imaging protocols. This thesis has focused on the research to improve radiography, and particularly mammography applications, by using a novel X-ray imaging modality, which exploits the wave nature of X-rays, rather than just their absorption in tissue. This novel phase-contrast approach has the potential to deliver significantly improved diagnostic information, especially also in the case where mammography is used for screening purposes. Here the novel scatter-sensitive dark-field signal opens up totally new possibilities in the assessment of various diseases and disorders of the human body.

Kai Scherer, in his thesis, has carried out several studies—in strong interdisciplinary collaboration with medical doctors at two university clinics in Munich—and has been able to demonstrate clearly this diagnostic potential in pre-clinical experiments. Thereby, a broad range of potential applications—ranging from the assessment of breast cancer over the evaluation of microcalcification clusters to the examination of renal stones—has been investigated. Further he addressed the key points for a successful implementation of this technique to a clinical routine in the near future, by presenting the very first dose-compatible and rapid scan time phase-contrast mammograms using a laboratory-based scanner.

He has published several solid and highly interesting publications in peer-reviewed journals, given a number of conference talks, and composed a sound and complete thesis document.

Garching January 2016 Prof. Franz Pfeiffer

Acknowledgments

First and foremost, I would like to thank my supervisor Prof. Dr. Franz Pfeiffer for giving me the opportunity to work on such a fantastic and exciting project—being of both medical and physical importance—for sharing his knowledge, for eagerly consulting me and providing me with a splendid working environment over the last 3 years. Further, I am in deep gratitude for Dr. Julia Herzen and Dr. Michael Chabior for their scientific input, their patience in supervising and working so closely with me.

I acknowledge the members of the examination committee of this thesis, Prof. Dr. Sibylle Ziegler and Prof. Dr. Ulrich Gerland.

I want to thank Dr. Susanne Grandl, Dr. Anikó Sztrókay-Gaul, and Dr. Karin Hellerhoff for their devoted help, which made this study possible in first place. The sample acquisition, the correct examination of the novel image contrasts, and the setting up of medical papers would have not been possible without your persistent effort. Same holds true for Dr. Sigrid Auweter for organizing the cooperation between TUM and LMU and making such a fruitful cooperation possible.

I would like to thank Prof. Dr. Doris Mayr who helped to verify our results by a rigid histopathological work-up and providing us with a collection of interesting samples.

I would further like to acknowledge the Microworks GmbH and the Institute of Microstructure Technology of the Karlsruhe Institute of Technology for providing us with high-quality gratings.

I would like to thank GE Healthcare, in particular Dirk Beque, Lukas Gromann, Jonathan Sperl, and Dr. Cristina Cozzini for a productive and interesting cooperation and Eduardo Coello for providing and helping with the image fusion algorithm.

I would like to thank T. Connall for providing the patients graphic.

I would like to thank the DFG Cluster of Excellence Munich-Centre for Advanced Photonics (MAP), the DFG Gottfried Wilhelm Leibniz program and the European Research Council (ERC, FP7, StG 240142) for financially supporting my studies and providing me with an interdisciplinary platform.

xiv Acknowledgments

I want to explicitly thank my bachelor and master students Lorenz, Konstantin, and Eva, for whom I had the one-time opportunity to supervise. It was great fun and pleasure working together with you. Thanks Lorenz for your strong commitment in assembling the dedicated mammography setup, for conducting the measurements and your efforts on consistently refining the scripts. Thanks Konstantin, for being so ambitious on optimizing the setup, which in the end enabled the first clinical compatible measurements and taking care of the sample examination. I further want to express my gratitude for Eva, for conducting many time-consuming experiments, among others the investigation of more than 30 calcifications and more than 100 kidney stones. Finally, I am very happy that you are taking over phase-contrast mammography.

I acknowledge Sebastian Allner for giving me a glimpse into the three-dimensional world of medical imaging and for helping me to operate phase-contrast tomosynthesis. Johannes Wolf, thanks for providing me with simulations and insights on dark-field signal generation of microcalcifications. Thanks Richard for reviewing my thesis and scientific work and Friedrich Prade and Florian Schaff for conducting high-energy measurements. Thanks Jonathan Schock for providing me with the segmentation algorithm.

I would particularly like to thank Martin Dierolf, Andreas Fehringer, and Björn Enders for patiently helping me with all issues regarding computing and SPEC.

A big shout-out to my office mates (Björn, Michael, Sebastian, Maite, Andreas, Klaus, Daniel) and the complete E17 team for many interesting discussions, proofreading of my work, a vivid working atmosphere, and most importantly many new good friends. Special thanks go to Nelly for turning a blind eye on my diffidence in comprehending bureaucracy. Thanks to Klaus, Brunhilde, Rudi, and Hans for helping me with the issues related to organization and device fabrication.

Finally, I want to thank my family, Jeanette, Omi, Nikki, Maik, and Theresa for consistently cheering and backing me up.

Contents

1	Prea	ımble.		1
	1.1	Motiv	ation and Historical Background	1
	1.2	Outlin	e	4
	1.3	Genera	al Remarks	6
	Refe	erences		7
2	Intr	oductio	on and Theoretical Background	9
	2.1	Interac	ctions of X-Rays with Matter	9
		2.1.1	Complex Refractive Index	10
		2.1.2	Attenuation of X-Rays	11
		2.1.3	Phase-Shift and Refraction of X-Rays	12
		2.1.4	Absorption and Phase-Shift Cross Section	14
	2.2	Gratin	g-Based Imaging	17
		2.2.1	The Talbot Effect	17
		2.2.2	X-Ray Talbot Interferometry	19
		2.2.3	Phase-Stepping	21
		2.2.4	Contrast Retrieval	23
		2.2.5	Adaptations for Clinical Use	26
	2.3	The F	emale Breast	29
		2.3.1	Breast Anatomy	29
		2.3.2	Breast Cancer	31
	Refe	erences		34
3	Exp	erimen	tal Setup and Methods Development	37
	3.1		-Contrast Mammography Setup	37
	3.2	Softwa	are Package mammolib	41
	Refe	erences		43
4	Bi-E	Direction	nal Phase-Contrast Mammography	45
	4.1		uction Limitations of Mono-Directional Phase-Contrast	
		Mamn	nography	45
	4.2	Result	S	47

xvi Contents

		4.2.1	Two-Dimensional Phase Retrieval	47
		4.2.2	Imaging Sensitivity of Mono- Versus Bi-Directional	~ 0
		4.0.0	Phase-Contrast Mammography	50
		4.2.3	"Directional" Dark-Field Mammography	52
		4.2.4	One- Versus Two-Directional Full-Field Phase-Contrast	
	4.3	Discus	Retrieval	53
		Phase-	-Contrast Mammography	55
	4.4	Mater	ials and Methods	57
		4.4.1	Imaging Dose	57
	Refe	rences		57
5	Scre	ening '	Value of Phase-Contrast Mammography	59
	5.1	Introd	uction Current Shortcomings of Clinical Screening	59
	5.2	Result	S	61
		5.2.1	Case I Dark-Field Mammography Reveals	
			Radiographically Undetectable Tumor Nodules	61
		5.2.2	Case II Dark-Field Mammography Reveals Pervasion	
			of the Breast with Partially Tumorous Soft-Tissue	
			Strands	64
		5.2.3	Case III Phase-Contrast Mammography Reveals	
			Tumor Margins with Special Cellular Characteristics	66
		5.2.4	Case IV Phase-Contrast Mammography Reveals	
			Actual Tumor Spread	68
	5.3		ssion Phase-Contrast Mammography as a Promising	
			date for Clinical Screening	70
	5.4	Mater	ials and Methods	72
		5.4.1	Study Design and Sample Acquisition	72
		5.4.2	Imaging Dose	73
		5.4.3	Preoperative Diagnostics	73
		5.4.4	Histological Work-Up	73
		5.4.5	Ex-Vivo Clinical Mammography	74
		5.4.6	Correlation Phase-Contrast Mammography, Ex-Vivo	
			Mammography, In-Vivo Imaging and Histology	74
	Refe	erences		74
6	Mici	rocalcif	fication Assessment with Dark-Field Mammography	77
			ation Limitations of Conventional Microcalcification	
		Analy	ses	77
	6.2		S	80
		6.2.1	In-Situ Microcalcification Assessment with Dark-Field	
			Mammography	80
		6.2.2	Dependence of Absorption $\bar{\mu}$ and Scattering Power	
			$\bar{\epsilon}$ of Microcalcification Clusters on Their Inherent	
			Micromorphology	82

Contents xvii

		6.2.3	Microtexture of Microcalcifications as a Potential	
			Indicator for Early Tissue Malignancy	86
	6.3		usion Microcalcification Assessment as a Diagnostically	
			sing Add-On Tool	88
	6.4	Mater	ials and Methods	91
		6.4.1	Pool of Specimens	91
		6.4.2	Data Normalization	91
		6.4.3	Micro-CT Measurements	91
		6.4.4	Voxel-Based Segmentation Algorithm	92
	Refe	erences		92
7	Tow	ard Cl	inically Compatible Phase-Contrast Mammography	95
	7.1		ation Status Quo of Phase-Contrast Mammography	95
	7.2		S	97
		7.2.1	Setup Optimization	97
		7.2.2	Experimental Verification	99
		7.2.3	Dark-Field Tomosynthesis	101
	7.3	Concl	usion Phase-Contrast Mammography Adaptable	
		to Cli	nical Requirements	104
	7.4	Mater	ials and Methods	106
		7.4.1	Image Processing	106
		7.4.2	Imaging Dose	106
		7.4.3	Tomosynthesis Protocol	107
		7.4.4	Image Fusion Protocol	107
	Refe	erences		109
8	Non	-invasi	ve Kidney Stone Differentiation Using Dark-Field	
			hy	111
	8.1		ation Limitations of Clinical Kidney Stone Diagnostics	111
	8.2		S	113
		8.2.1	Analytical Description	113
		8.2.2	Absorption Characteristics of Renal Calculi	114
		8.2.3	Scattering Characteristics of Renal Calculi	114
		8.2.4	X-Ray Dark-Field Radiography of Renal Calculi	116
		8.2.5	Statistical Analysis of Renal Calculi Classification	117
		8.2.6	Diagnostic Performance of Renal Calculi	
			Classification	117
	8.3	Concl	usion Highly Sensitive Kidney Stone Assessment via	
		Dark-Field Abdomen Radiography		
	8.4		ials and Methods	121
		8.4.1	Study Design	121
		8.4.2	Statistical Analysis	122
		843	Micro-CT Measurements	122

xviii Contents

		8.4.4	X-Ray Dark-Field Interferometer	122
		8.4.5	Imaging Dose	123
		8.4.6	Potential Clinical Implementation	123
	Refe	rences	3	124
9	Sum	mary	and Outlook	127
	9.1	Sumi	mary of Results	127
		9.1.1	Diagnostic Merit of Phase-Contrast Mammography	127
		9.1.2	Clinical Compatibility of Phase-Contrast	
			Mammography	128
		9.1.3	Renal Stone Assessment via X-Ray Dark-Field	
			Radiography	129
	9.2	Curre	ent Limitations and Future Challenges	129
	9.3	Outlo	ook and Next Steps	131
	Refe	rences	8	133
Aŗ	pend	ix A:	Supplementary Movies	135
Αŗ	pend	ix B:	Correct Quantitative Evaluation of X-ray	
			Dark-Field Images for Microcalcification Analysis	
			in Mammography	137
Re	feren	ces		140

Abbreviations

General Abbreviations

A-Mx Experimental absorption mammography

CNR Contrast-to-noise ratio CT Computed tomography

DF-Mx Experimental dark-field mammography

DPC-Mx Experimental differential phase-contrast mammography

EV-Mx Clinical ex vivo mammography

FFT Fast Fourier transform

IV-Mx Clinical in vivo mammography

MGD Mean glandular dose

mGy Milligray

PC-Mx Experimental (absolute) phase-contrast mammography

ROC Receiver operating characteristic curve

Medical Abbreviations

AP Anteroposterior

ACR American College of Radiology

BIRADS Breast imaging reporting and data system

CC Craniocaudal

DCIS Ductal carcinoma in situ
IDC Invasive ductal carcinoma
MRI Magnetic resonance imaging

MLO Mediolateral oblique

NST Cancer of nonspecific type

TNM Classification of malignant tumors

xx Abbreviations

Symbols

\boldsymbol{A}	Absorption signal
c	Kidney stone classifier
D	Dark-field signal
d_T	Full Talbot distance
d_n	Fractional Talbot distance

 \mathcal{F} Fourier transform

 \mathcal{F}^{-1} Inverse Fourier transform

Distance between source and phase grating
 Distance between X-ray source and sample
 Distance between phase and analyser grating

G Gaussian filter

 $G_{1,2,3}$ Source, phase, and analyser grating

 $p_{1,2,3}$ Grating period

 p_T Interference pattern period

s Source size

 s^* Projected source size T Transmission signal V Visibility signal

 $\begin{array}{lll} \bar{\epsilon} & & & & \text{(Projected) scattering coefficient} \\ \varepsilon_{\text{eff}} & & & & \text{Effective scattering coefficient} \\ \bar{\mu} & & & & \text{(Projected) absorption coefficient} \\ \mu_{\text{eff}} & & & & \text{Effective absorption coefficient} \\ \partial \phi & & & & \text{(One-dimensional) phase gradient} \\ \end{array}$

 Φ^{1d} One-dimensional integrated phase signal Φ^{2d} Two-dimensional integrated phase signal (Low-frequency) corrected phase signal

 Φ_s Sharpened phase signal

Chapter 1 Preamble

Ich fand ganz zufällig, dass die Strahlen schwarzes Papier durchdringen.

Wilhelm Röntgen

1

1.1 Motivation and Historical Background

In the year 1895, Wilhelm Röntgen discovered a novel electromagnetic radiation while investigating cathode rays, which he signified with an "X" for being of yet unknown type [1]. By accident, he found that the latter yield the capability of penetrating black paper which is typically opaque for visible light. This observation prompted him to repeat the experiments with optically intransparent matter. Utilizing a photographic plate, Röntgen managed to retrieve the first radiography of a human hand and phalanges, by which he unwittingly laid the foundation for all modern X-ray applications, including medical diagnostics, non-destructive testing, security screening and fundamental research. For a very long time, X-rays were solely utilized to reveal high density-fluctuations within a sample, by simply mapping differences in the transmission of photons through the investigated specimen, using photosensitive plates and later electronic detectors.

In contrast, for visible light already more than 200 years ago, first "dark-field" techniques were utilized to complement conventional bright-field microscopy [2]. While initial approaches did not use any additional optical devices, but instead relied on a special positioning of the background illumination, small animals and blood components could be successfully imaged. Modern techniques rely on a condenser which is directly placed in the beam path to prevent rays from reaching the ocular lens. When inserting an object, incident rays are scattered at sub-structures of the specimen and deflected into the ocular, which results in a bright, contoured depiction of the latter on a dark background. Figure 1.1a shows a dark-field micrograph of a thin paper-tissue (bottom) alongside with its respective bright-field contrast (top) [3]. A further breakthrough in conventional microscopy took place in the years 1934 and

2 1 Preamble

1936, when Frits Zernike invented and the Carl Zeiss AG built the first phase-contrast microscope, respectively [4, 5]. Especially for biomedical imaging, this development was of immense importance, since soft-tissue samples, which had so far been yet virtually transparent, could be visualized by mapping their refraction properties.

For a long time, a translation of this effort towards X-ray imaging was unsuccessful, contingent on the fact that phase-shift induced refraction angles are in the range of nano-radians. This, as well as the circumstance that the fabrication of X-ray optics is even nowadays complex, makes a direct measurement of these angles difficult. The very first X-ray interferometer was developed by Bonse and Hart in the year 1965 comprising a beam-splitter optics composed of three single crystals [6]. Crystal-interferometry grounds on a collimated, monochromatic beam which is split-up into sample-probing and reference beam. By coherently re-combining both beams, after being deflected by the specimen, distortions imprinted on the reference interference pattern can be analysed, by which information on the phase-shifting properties of the specimen are deduced. This technique, however proved to be unsuitable for a broad clinical implementation, being too sensitive for even moderate phase-shift differences, requiring an extremely high system stability in range of sub-Ångström, offering a very limited field-of-view, while additionally requiring long exposure times.

Within the 1990s, additional phase-sensitive methods have been steadily developed, including analyser-based (diffraction-enhanced) imaging [7, 8]. Here an analyzer crystal, is positioned behind the sample in Bragg-geometry, which is then subsequently rotated with respect to the incident beam to obtain the angular distribution of the refracted X-rays. The obtained rocking curves can then be related to the differential phase properties of the specimen. Furthermore, in the year 1995 propagation-based phase-contrast imaging (in-line holography) gained major interest, as it does not require any kind of X-ray optics [9, 10]. By taking multiple images at various propagation distances, the wave-front is sampled in spatial and frequency domain, by which a decomposition in phase-shift and absorption contributions becomes feasible.

Considering a broad integration into a clinical routine, the aforementioned phase-sensitive techniques, however, share one common obstacle: they are mostly restricted to synchrotron facilities, since demanding very high standards with respect to either beam quality (spatial and/or temporal coherence, collimation), flux or setup stability. While micro-focus tubes would be compact enough for a clinical environment, and also provide sufficient spatial coherence, they exhibit a very limited photon flux only, which would result in unacceptable examination times when performing mammography.

A first step towards overcoming these limitations was undertaken by the invention of a Talbot interferometer, which offers a large field-of-view, while being rather insensitive with respect to the X-ray polychromaticity of conventional sources [11, 12]. These interferometers make use of a beam-splitter grating, which creates an interference pattern at distinct beam propagation distances. If operated with clinical detectors, a second, highly-absorbing grating is required to accurately sample the

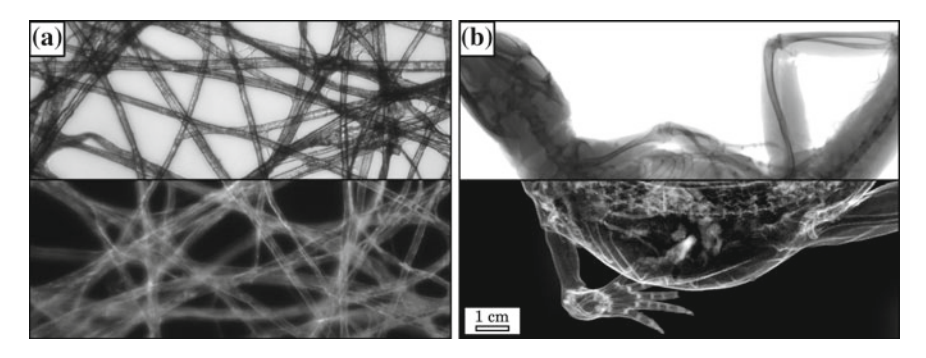


Fig. 1.1 Bright-field/Transmission and dark-field imaging with visible light and X-rays. **a** Bright-(top) and dark-field (bottom) micrograph of a tissue-paper at tenfold magnification. Images adapted from Wheeler, R. (2010) [3]. **b** Large field-of-view X-ray transmission (top) and dark-field radiography (bottom) of a lizard obtained with a laboratory Talbot-Lau interferometer. In comparison to visible light microscopy, X-ray radiography offers the possibility to probe optically dense and extended samples

evoked intensity modulations. When introducing a sample, the wave-front is modified which results in a distortions of the interference pattern and the generation of so-called "Moiré fringes". Initially, signal extraction relied on Fourier Analyses of the latter, whereas the achievable spatial resolution is restricted to the fringe period [13]. With the goal of providing a higher spatial resolution, a phase-stepping procedure was developed later on, which relies on a step-wise sampling of the intensity modulations through translation of the grating. The key-milestone for a future clinical implementation of phase-sensitive X-ray interferometry was accomplished in 2006, with the introduction of a third, highly-absorbing grating [14, 15]. This element essentially decouples the X-ray source from the stringent beam coherence requirements for phase-sensitive X-ray imaging, rendering the latter compatible with compact, high-flux sources as used in clinical systems.

Of special diagnostic interest is the fact, that this so-called "Talbot–Lau" arrangement, is not only sensitive to beam refractions, but in addition also to diffuse angular deflections caused by a specimen [16]. Similar to the dark-field contrast in the case of visible-light microscopy, X-ray dark-field imaging relies on small-angle scattering caused by substructures on the (sub)-micron scale, however with the advantage of being capable of penetrating through optically dense matter. Figure 1.1b shows a large field-of-view, side-by-side illustration of a formalin-fixed lizard once depicted in the X-ray dark-field channel (bottom) and once illustrated by the transmission signal (top), obtained by the Talbot–Lau interferometer implied for this thesis.

Current research is mostly focusing on the identification of diagnostic applications arising from phase-contrast and dark-field imaging, including, among others, diseases and disorders of the lung, bones, arteries and kidneys [17–19]. Here, great

4 1 Preamble

potential is expected, since pathological changes do not necessarily imply an alternation of tissue density, but instead are frequently accompanied by structural changes on the cellular level. Further, immense effort is put in the translation of lab-based setups into (pre)-clinical systems, in order to address concerns regarding radiation dose and scan time, with the ultimate goal of enabling first reader studies and verifying results in a statistically relevant framework. Recently, the first radiography and tomography studies on living mice have been reported [20].

Within the assembly of clinical diagnostics, the female breast holds a special position with respect to phase-sensitive radiography: it is routinely and in first instance investigated with radiographic screening, which however suffers from a low sensitivity and specificity, particularly pronounced among the examination of young women. While MRI and sonography avoid ionizing radiation and provide an overall enhanced sensitivity, they are time-consuming and costly and therefore only applied as a supplemental screening modality. Further, phase-sensitive imaging offers new possibilities in the assessment and detection of microcalcifications, tissue borders and architectural distortions, which play an essential role in breast disease diagnostics. Therefore, phase-sensitive mammography is considered to yield enormous potential to revolutionize current diagnostic reliability while being applicable as a screening modality without increasing clinical examination time, costs or efforts regarding infrastructure. Finally, the female breast is an exterior organ, hence can be investigated with rather soft X-rays, which relaxes requirements with respect to grating fabrication, X-ray sources and polychromaticity.

Yielding favourable capabilities and preconditions, phase-contrast mammography attracted major interest in scientific and industrial research, which recently resulted in the development of a first pre-clinical, slit-scanning mammography unit, built by the Philips GmbH [21]. While encouraging, since intrinsically avoiding the phase-stepping procedure, concerns arise with respect to imaging sensitivity and phase-retrieval accuracy.

1.2 Outline

Ensuing from this recent milestone, the ultimate goal of this thesis is to push phase-contrast mammography towards a potential clinical implementation. This is done, by first verifying its diagnostic surplus value as a screening modality and then subsequently demonstrating that phase-contrast mammography can be operated in a clinically compatible manner. For this purpose, a general check-list was put up a priori, summarizing the key-requirements, which a novel imaging technique has to fulfil in order to replace/refine conventional screening mammography.

1.2 Outline 5

Key requirements

- **#1** Must be a modality-integrated one-step approach.
- #2 Should be an upgrade/similar to a conventional system.
- #3 Must provide isotropic detection sensitivity.
- **#4** Must provide an enhanced visualization of high-frequency image contents.
- #5 Must provide an increased soft-tissue contrast in dense breast.
- **#6** Must provide a refined classification of microcalcifications, if detection-rates/sensitivity are increased.
- #7 Must meet dose requirements according to international guidelines.
- **#8** Must fulfil image quality/detection criteria set by the American College of Radiology.
- **#9** Should not increase examination time and staff resources.
- **#10** Must be compatible with tomosynthesis.
- #11 Should be a multi-purpose application.

Each chapter aims at addressing certain points of the check-list, while additionally providing the reader with the necessary background information. After this introduction the thesis is organized as follows:

Chapter 2 gives an overview on the interaction between X-rays and matter and elucidates on a physical basis, why phase-contrast and dark-field imaging exhibit the potential to excel conventional absorption-based mammography. Afterwards the theoretical background underlying the imaging technique used in this study is introduced. Talbot–Lau interferometry intrinsically provides three image contrasts at once, among these also the conventional absorption image (#1), which renders it compatible with the existing, clinical data-pool as well as the education of radiologists. Finally, this chapter concludes with a brief summary of the female breast, its structure and pathological changes associated with the latter.

Chapter 3 is devoted to the development of a compact, grating-based X-ray phase-contrast mammography setup. Here, we show that the systems yields a hardware design very similar to a conventional mammography unit, while also being capable of performing within a laboratory environment (#2). The second part of this chapter briefly introduces the python-library mammolib, which is used for obtaining comprehensive, full-field phase-contrast mammograms.

Chapter 4 presents the first two-directional, phase-contrast mammograms of a cancerous mastectomy sample, which in combination succeed at providing full feature sensitivity, independently from grating direction (#3). We further illustrate that the phase image enables an extraordinary good depiction of high-frequency features, yet unseen within the absorption channel (#4). This chapter concludes with a benchmark of mono- vs. bi-directional measurements alongside with a comparison of various phase-retrieval algorithms.

6 1 Preamble

Chapter 5 comprises the central results regarding the diagnostic value of phase-contrast mammography as a screening modality. By means of a case study including the investigation and work-up of four freshly dissected ablates, we show that phase-sensitive imaging provides image content (both cancerous and non-cancerous) yet unseen in conventional, clinical examination, including magnetic resonance imaging and sonography, nevertheless being of high diagnostic value (#5).

Chapter 6 presents a dose-compatible, diagnostic tool for the assessment and risk stratification of breast microcalcifications using dark-field mammography (#6). Based on microtexture analysis, we propose a refined grading of calcifications to promote a reduction of breast-biopsies and recall-rates. This is of special importance considering that an increase in microcalcification detection sensitivity, provided by scatter-sensitive imaging, is only beneficial if accompanied by a corresponding gain in specificity.

Chapter 7 is dedicated to the clinical compatibility of laboratory-based, phase-contrast mammography. Here, we present the very first dose-compatible (#7) and rapid scan time phase-contrast mammograms of both a freshly dissected mastectomy specimen and a mammographic accreditation phantom (#8). The trimodal image contrast is presented in a comprehensive manner and benchmarked with conventional, state-of-the-art mammograms and verified with respect to current detection criteria (#9). This chapter concludes with a proof-of-principle study on dark-field tomosynthesis (#10).

Chapter 8 elucidates scatter-sensitive, dark-field radiography as a tool for the assessment of renal calculi (#11). Here we show that a highly sensitive and specific differentiation of calcium oxalate and uric acid stones is feasible, utilizing their inherent differences with respect to chemical composition, microscopic growth structure and morphology. Finally, we investigate in-vivo transferability of this technique by measuring a preliminary abdomen phantom.

Chapter 9 gives a summary of the result presented in this thesis. Further, current shortcomings, challenges and potential next steps associated with phase-contrast mammography are discussed.

1.3 General Remarks

This thesis is written in book-style, comprising two background chapters and five result chapters, which can be read independently from each other. Correspondingly, each chapter contains its own introduction and bibliography. Additionally, the result chapters include a short abstract as well as an overview of three core statements, which are framed for better readability. Figures that have a supplementary movie are indicated by a tape-sign and can be accessed using the corresponding link or QR-code in Appx. A. Following clinical conventions the mammograms presented here are generally not accompanied by a quantitative colormap, contingent on an

1.3 General Remarks 7

extensive post-processing applied to the latter. Further, measurements underlying this thesis were conducted with different scan directions. Single and crossed arrows within the figures indicate mono- and bi-directional measurements, respectively. Unless specified otherwise, the standard scan direction is horizontal, i.e. from left to right.

Finally, this study includes the investigation of human specimens; hence was conducted in accordance with the Declaration of Helsinki and was approved by the local ethics committee (Ethikkommission of the Ludwig-Maximilian-University, Munich). All participants gave written informed consent before inclusion after adequate explanation of the study protocol.

References

- Novelline, R. (1997). Squire's fundamentals of radiology. Cambridge: Harvard University Press.
- 2. Quekett, J. (1852). A Practical treatise on the use of the microscope. London: H. Bailliere.
- 3. Wheeler, R. (2010). Micrograph of Whatman lens tissue paper. Bright/Dark-field illumination. http://de.wikipedia.org/wiki/File:Paper_Micrograph_Bright/Dark.png.
- 4. Zernike, F. (1942). Phase-contrast, a new method for microscopic observation of transparent objects. *Physica*, *9*, 974–986.
- 5. Zernike, F. (1955). How I discovered phase contrast. Science, 121, 345–349.
- 6. Bonse, U., & Hart, M. (1965). An X-ray interferometer. Applied Physics Letters, 6, 155–157.
- 7. Davis, T., et al. (1995). Phase-contrast imaging of weakly absorbing materials using hard X-rays. *Nature*, *373*, 595–598.
- 8. Chapman, L., et al. (1997). Diffraction enhanced X-ray imaging. *Physics in Medicine and Biology*, 42, 2015–2025.
- 9. Snigirev, A., et al. (1995). On the possibility of X-ray phase contrast microimaging by coherent high-energy synchrotron radiation. *Review of Scientific Instruments*, 66, 5486–5492.
- Wilkins, S., et al. (1996). Phase-contrast imaging using polychromatic hard X-rays. *Nature*, 384, 335–338.
- 11. David, C., Nöhammer, B., & Ziegler, E. (2002). Differential X-ray phase contrast imaging using a shearing interferometer. *Applied Physics Letters*, 81, 3287–3290.
- 12. Takeda, T., et al. (2002). Vessel imaging by interferometric phase-contrast X-ray technique. *Circulation*, 105, 1708–1712.
- 13. Bevins, N., Zambelli, J., Li, K., Qi, Z., & Chen, G. (2012). Multicontrast X-ray computed tomography imaging using Talbot-Lau interferometry without phase stepping. *Medical Physics*, *39*, 424–428.
- 14. Pfeiffer, F., Weitkamp, T., Bunk, O., & David, C. (2006). Phase retrieval and differential phase-contrast imaging with low-brilliance X-ray sources. *Nature Physics*, 2, 258–261.
- 15. Pfeiffer, F., Kottler, C., Bunk, O., & David, C. (2007). Hard X-Ray phase tomography with low-brilliance sources. *Physics Review Letters*, 98, 108105.
- Pfeiffer, F., et al. (2008). Hard-X-ray dark-field imaging using a grating interferometer. *Nature Materials*, 7, 134–137.
- 17. Yaroshenko, A., et al. (2013). Pulmonary emphysema diagnosis with a preclinical small-animal X-ray dark-field scatter-contrast scanner. *Radiology*, 269, 427–433.
- 18. Eggl, E., et al. (2015). Prediction of vertebral failure load by using X-ray vector radiographic imaging. *Radiology*, 275, 553–561.
- Hetterich, H., et al. (2014). Phase-Contrast CT: qualitative and quantitative evaluation of atherosclerotic carotid artery plaque. *Radiology*, 271, 870–878.

8 1 Preamble

20. Bech, M., et al. (2013). In-vivo dark-field and phase-contrast X-ray imaging. *Scientific Reports*, 3, 3209.

 Koehler, T., et al. (2015). Slit-scanning differential X-ray phase-contrast mammography: proofof-concept experimental studies. *Medical Physics*, 42, 1959–1965.

Chapter 2 Introduction and Theoretical Background

If the facts don't fit the theory, change the facts.

Albert Einstein

Abstract In this chapter the theoretical background underlying this thesis is presented to the reader. Hereby, special focus is put on interpreting and motivating theoretical considerations directly in the context of mammography. At first a description on how X-rays interact with matter alongside with the respective interaction cross sections is given, which follows considerations made by Als-Nielsen and McMorrow (Elements of modern X-ray physics, 2011, [1]) and Willmott (An introduction to synchrotron radiation: Techniques and applications, 2011, [2]). The drawn conclusions exemplify why phase-sensitive imaging techniques yield the potential to prevail conventional absorption-based methods in the field of soft-tissue assessment. Afterwards the theoretical framework for grating-based imaging utilizing X-ray Talbot interferometry is introduced. Moreover, the adjustments which are necessary to translate "idealized" grating-based imaging towards clinical implementation are outlined. Finally, this chapter concludes with a brief overview on the morphology and pathological changes of the female breast as well as the clinical diagnostics and the options of treatment associated with the latter.

2.1 Interactions of X-Rays with Matter

X-rays are electromagnetic waves with wavelengths ranging from 0.1 to 100 Å. One differentiates "hard" from "soft" X-rays, if they exceed an energy of 5–10 keV. In the case of medical imaging, hard X-rays are used to achieve a sufficient penetration of tissue. Here, X-rays can interact with the tissue, more precisely its atoms, in various ways. The impinging photon can either be scattered and/or photoelectrically absorbed. In the case of scattering, elastic processes (wavelength of the photon is preserved during interaction) are distinguished from inelastic interactions (wavelength of the photon is altered during interaction). Elastic scattering at a free, charged

particle is called Thomson scattering, while the sum of coherent scattering at bound electrons is described by the Rayleigh formalism. In a semi-classical picture this process can be understood as an incident photon accelerating an electron, which in turn emits a photon with the same wavelength, albeit of different direction of propagation. In contrast, in the case of inelastic scattering, which is termed as the Compton effect, the photon "collides" with the electron, by which energy is transferred to the electron, while the photon experiences a respective decrease in frequency.

Conventional absorption-based imaging comprises mostly contribution from inelastic processes, namely photoelectric absorption and Compton scattering (elastic Rayleigh scattering is of minor impact only), while phase-contrast formation solely relies on elastic contributions. Utilizing the phenomenological concept of the complex refractive index, adapted from the description of visible light, the aforementioned interactions, which cause wave diffraction when encountering an object, can be summarized. A more detailed description of the respective absorption and phase-shift cross sections and their dependency on X-ray energy and target material characteristics is given the following subsections.

2.1.1 Complex Refractive Index

In the case of X-rays ($\delta \ll 1$), the complex refractive index of a medium is typically written as

$$n = \underbrace{1 - \delta}_{\text{[elastic]}} + \underbrace{i\beta}_{\text{[inelastic]}}, \tag{2.1}$$

where δ denotes the refractive index decrement, which is associated with elastic interactions between the photon and the penetrated medium, and β is the imaginary part of the refractive index, which is predominately related to the respective inelastic processes. Consider an ideal, plane wave-front Ψ_{ν} propagating in z-direction within vacuum $(n=1, \delta=0, \beta=0)$, which can be written as

$$\Psi_{v}(\vec{r},t) = \Psi_{0} e^{i(\vec{k}\vec{r}-\omega t)} = \Psi_{0} e^{i(kz-\omega t)},$$
 (2.2)

where $\vec{k}=(0,0,k=\frac{2\pi}{\lambda})$ denotes the wave-vector, λ is the wavelength, ω is the angular frequency, and Ψ_0 is the wave-amplitude. When the wave-front enters a medium with complex refractive index n the wave-vector k is modified to kn, as schematically depicted in Fig. 2.1a. Therefore the modified wave can be re-written in terms of the incident wave by

$$\Psi_m(z,t) = \Psi_0 e^{i(nkz - \omega t)} = \Psi_0 e^{-i\omega t} e^{(1-\delta)ikz} e^{-\beta kz} = \Psi_v(z,t) \cdot \underbrace{e^{-i\delta kz}}_{\text{[phase-shift]}} \cdot \underbrace{e^{-\beta kz}}_{\text{[attenuation]}}.$$
(2.3)

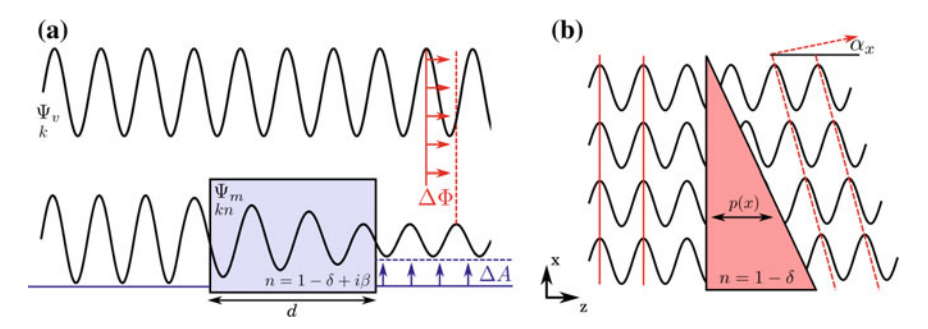


Fig. 2.1 Attenuation and phase-shift of X-rays. **a** When a wave-front Ψ_v travels through a medium with complex refractive index n, it experiences a decrease in wave-amplitude by ΔA as indicated by blue arrows, which is associated with the imaginary part of the refractive index. Further the perturbed wave Ψ_m receives a shift in the wave-phase by $\Delta \Phi$ as indicated by red arrows, which is associated with the decrement of refractive index. **b** When a wave-front travels through a phase prism ($\beta = 0$), a local variation in wave-shift implies a refraction of the wave by an angle α_x , with respect to the incident wave-front. Note that peaks of the excited waves are aligned on a line (dashed line), which is titled by the angle α_x with respect to the horizontal

Hence, after travelling through a medium with thickness d, the wave-amplitude and wave-phase of the exit-wave are modified by a factor $e^{-\beta kd}$ and $e^{-i\delta kd}$, respectively.

2.1.2 Attenuation of X-Rays

The intensity I of an electromagnetic wave is given by the square of the absolute value of its wave-function. Accordingly, the transmission value T can be calculated from the ratio of beam intensities before $I_v(z=0)$ and after traversing a medium $I_m(z=d)$ with thickness d, using

$$T(d) = \frac{I_m(d)}{I_n(0)} = \frac{|\Psi_m(d,t)|^2}{|\Psi_n(0,t)|^2} = e^{-2k\beta d}.$$
 (2.4)

Comparing this result to the Beer-Lambert equation

$$T(d) = \frac{I_m(d)}{I_v(0)} = e^{-\mu d},$$
 (2.5)

with μ denoted the linear attenuation coefficient, shows that μ equals $2k\beta$. Note that the decrease in wave-amplitude caused by a medium is given by

$$\Delta A = \Psi_v - \Psi_m = \Psi_v (1 - e^{-k\beta d}). \tag{2.6}$$

2.1.3 Phase-Shift and Refraction of X-Rays

From Eq. 2.3, we can see that a wave-front, that passes through a medium experiences a relative phase-shift $\Delta\Phi$, which equals

$$\Delta \Phi = \delta k z. \tag{2.7}$$

As a consequence thereof the perturbed wave is additionally refracted by an angle α_x with respect to the horizontal, incident wave-front. This effect becomes understandable when considering a plane of waves, that travels in z-direction through a phase prism ($\beta = 0$), as schematically depicted in Fig. 2.1b. With respect to their x-coordinate each of the waves undergoes a different phase-shift $\Delta\Phi(x)$, which is dependent on the actual optical path length of the prism p(x), and given by

$$\Delta\Phi(x) = k\delta p(x). \tag{2.8}$$

From Fig. 2.1b, we can see that the phase-shifted waves have their peaks mutually aligned on a line, that is tilted by α_x with respect to the horizontal. Hence, the exciting wave-front can be considered as an array of in-phase waves with altered direction of propagation. Using geometrical considerations and small-angle approximation, the refraction angle α_x can be directly associated with the induced phase-shift, more precisely its first derivative, by [3]

$$\alpha_x \approx \sin(\alpha_x) = \frac{1}{k} \frac{\partial \Phi(x, y)}{\partial x}.$$
 (2.9)

In the more general case of three-dimensional objects, where material entities change throughout the object, the aforementioned equations have to be extended by an integral in propagation direction, i.e.

$$T(x, y) = e^{-2k \int \beta(x, y, z) dz},$$
 (2.10)

$$\Delta\Phi(x,y) = k \int \delta(x,y,z) \, dz, \tag{2.11}$$

and

$$\alpha_x(x, y) = \frac{1}{k} \frac{\partial \Phi(x, y)}{\partial x} = \frac{\partial}{\partial x} \int \delta(x, y, z) \, dz. \tag{2.12}$$

In the following, we estimate typical refraction angles of X-rays in the case of soft-tissue. Consider a wave in medium (n_m) , that is impinging on the interface between the medium and vacuum (n_v) at an incident angle γ_{in} (with respect to the interface orthogonal): after refraction the exit-wave exhibits an angle γ_{ex} (with respect to the interface orthogonal), that is determined by Snell's law as

$$n_m \sin(\gamma_{in}) = n_v \sin(\gamma_{ex}). \tag{2.13}$$

Assuming that the reflections are of minor magnitude only, which is justified by the fact that δ is much smaller than unity and defining the refraction angle α as difference between the exit (γ_{ex}) and the incident angle (γ_{in}), shows that α is given as

$$n_m \gamma_{in} = \gamma_{ex} = \alpha + \gamma_{in}, \tag{2.14}$$

$$\alpha = \gamma_{in}(n_m - 1) = -\gamma_{in}\delta. \tag{2.15}$$

Since α is negative, γ_{in} is larger than γ_{ex} , which implies a refraction of the wave towards the surface orthogonal. For energies typically used for phase-contrast mammography, i.e. $\leq 40 \, \text{keV}$, δ ranges in the order of 10^{-7} – 10^{-5} (Fig. 2.2b), which accounts for refraction angles being in the regime of micro-degrees/nano-radians. Hence, to directly resolve X-ray refractions, either a long propagation distance or detectors with ultra-small pixel pitch are required, both being incompatible with clinical requirements. More advanced methods, which utilize optical elements to indirectly retrieve the phase information, are explained in Sect. 2.2.

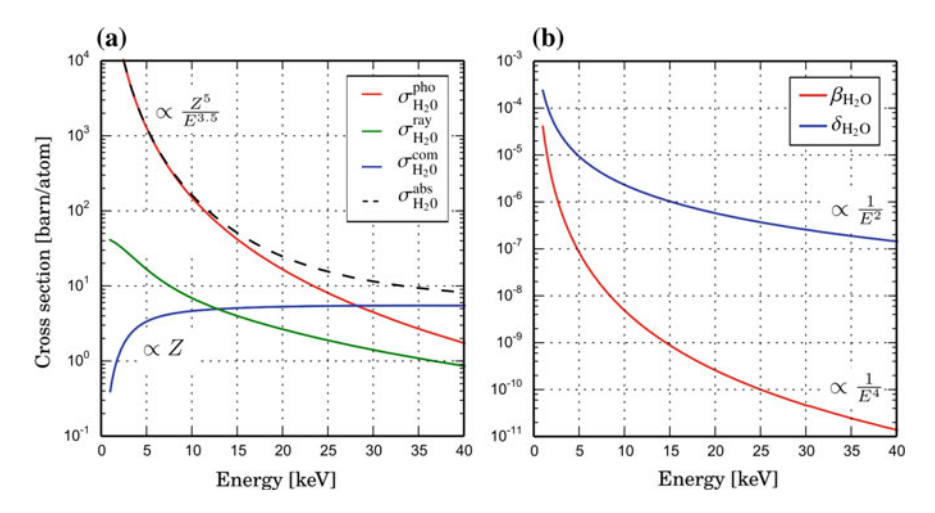


Fig. 2.2 Absorption and phase-shift characteristics of water at clinical X-ray energies. a Contributions to the total absorption cross section of water $\sigma^{abs}_{H_20}$, as indicated by dashed line. Up to an energy of 30 keV the photoelectric absorption ($\sigma^{pho}_{H_20}$) is the prevailing interaction between photons and water atoms. In the case of higher X-ray energies, the Compton effect ($\sigma^{com}_{H_20}$) is the dominating interaction. Rayleigh scattering ($\sigma^{ray}_{H_20}$) is hardly contributing to the absorption cross section, albeit is the prominent interaction for the generation of the phase-shift. b Decrement δ and imaginary part β of the refractive index of water. Note that, δ exceeds β by up to four orders of magnitude. Besides, δ decreases proportionally to the square energy E^{-2} , in comparison to β which decreases proportionally to E^{-4} . Data obtained from XOP [4]

2.1.4 Absorption and Phase-Shift Cross Section

With the goal of illustrating the benefits arising from phase-contrast in comparison to attenuation-based imaging the underlying interactions of photons with matter are investigated in more detail in the following. In a semi-classical picture, the interaction of X-rays with matter can be considered as a scattering process of an incoming electric field $\varepsilon_{in}(\vec{k})$ at the charge distribution of an atom. Here, the incoming electric field $\varepsilon_{in}(\vec{k})$ forces the bound electrons of an atom to harmonically oscillate. In return, they emit an outgoing electric field, which exhibits the shape of spherical waves $\varepsilon_{out}(\vec{k}') \propto \varepsilon_{in}(\vec{k}) \frac{e^{ikR}}{R}$, more precisely determined to

$$|\varepsilon_{out}(P, \vec{k}, E, R)| = -r_e \hat{P} f(\vec{q}, E) \underbrace{|\varepsilon_{in}|}_{\text{spherical wave}} e^{ikR}. \tag{2.16}$$

Here r_e denotes the classical electron radius, \hat{P} is a factor, which accounts for the polarisation of the field, $f(\vec{q}, E)$ is the atomic scattering factor, $\vec{q} = \vec{k}' - \vec{k}$ is the scattering vector and R is the distance from the scattering event. The atomic scattering factor, which defines the interaction process, is termed to

$$f(\vec{q}, E) = f_0(\vec{q}) + f_1(E) - if_2(E),$$
 (2.17)

where $f_0(\vec{q})$ is the energy-independent form factor, which describes scattering at free electrons and $f_1(E)$ and $if_2(E)$ are dispersions corrections, which account for energy-dependent interactions with the bound electrons of the atom, respectively. In the case of elastic scattering, which is confined to the forward direction ($\vec{q} \approx 0$), the complex refractive index n can be directly associated with the atomic scattering factor $f(\vec{q} \approx 0, E)$, utilizing

$$n(E) = 1 - \frac{r_e \lambda^2 N}{2\pi} (f_0(0) + f_1(E) - if_2(E)), \qquad (2.18)$$

where N denotes the atomic number density. Further the form factor f_0 is defined as the Fourier Transform of the charge distribution $\rho(r)$. In the considered case where scatter prevails in the forward direction the Fourier Transform equals an integration in real space. And therewith corresponds to the overall number of charges incorporated by the atom, which is equivalent to the atomic number Z, since

$$f_0(\vec{q} \approx 0) = \int \rho(r)e^0 d^3r = Z.$$
 (2.19)

Further, the real part of the dispersion coefficient f_1 can be neglected if X-ray energies are far from the absorption edges of the investigated material. This holds

true for soft-tissue, which typically comprises low Z elements only, with absorption edges being far below the X-ray energies utilized for breast imaging. Carbon, oxygen and calcium for instance show characteristic absorption edges at 0.28, 0.53 and 4.0 keV, respectively. Correspondingly, Eq. 2.18 can be simplified to

$$n(E) \approx 1 - \frac{r_e \lambda^2 N}{2\pi} (Z + 0 - if_2(E)) = 1 - \underbrace{\frac{r_e \lambda^2 N}{2\pi} Z}_{[\delta]} + i \underbrace{\frac{r_e \lambda^2 N}{2\pi} f_2}_{[\beta]}. \quad (2.20)$$

When we compare Eq. 2.20 derived above against Eq. 2.1, introduce the atomic absorption σ^{abs} and phase-shift cross section σ^{pha} , and additionally substitute NZ with the electron density ρ_e , we see that β and δ are given by

$$\beta(Z, E) = \frac{r_e \lambda^2 N}{2\pi} f_2 = \frac{\lambda N \sigma^{\text{abs}}}{4\pi}, \qquad (2.21)$$

$$\delta(Z, E) = \frac{r_e \lambda^2 \rho_r}{2\pi} = \frac{\lambda N \sigma^{\text{pha}}}{2\pi}.$$
 (2.22)

In comparison to the phase-shift cross section, which solely relies on elastic scattering the total absorption cross section σ^{abs} comprises multiple energy-dependent contributions

$$\sigma^{\text{abs}}(Z, E) = \sigma^{\text{ray}} + \sigma^{\text{pho}} + \sigma^{\text{com}} + \sigma^{\text{pai}},$$
 (2.23)

where $\sigma^{\rm ray}$ is the Rayleigh scattering cross section, which denotes elastic scattering at the bound electrons of an atom. Photoelectric absorption (σ^{pho}) describes the effect of a photon being completely absorbed by an inner-shell electron. If the photon energy exceeds the electron binding energy, the atom is ionized and the respective photo-electron emitted from the atom. Compton scattering (σ^{com}) corresponds to inelastic scattering and is given as the incoherent sum of scattering at the electrons of an atom. Here, the photon collides with an electron, which accompanies an energy transfer from the photon to the recoiling electron. Contingent on the conservation of energy and momentum the photon further experiences an increase in wavelength during the scatter event. Pair production (σ^{pai}) requires photon energies above 1 MeV and hence does not play any role for soft-tissue X-ray imaging. Figure 2.2 gives an exemplary overview on the energy dependency of the various cross sections in the case of water, which is chosen as a soft-tissue representative. Up to an energy of approximately 30 keV photoelectric absorption is the dominating interaction. For X-ray energies exceeding this value, the Compton effect is on the onset of prevailing the total absorption cross section. Finally, Rayleigh scattering is only of minor impact for the generation of absorption-based imaging contrast, albeit it is the prominent interaction for the phase-shift cross section.

The photoelectric cross section itself is heavily dependent on the atomic number of the absorbing material and rapidly decays with X-ray energy. Far from absorption edges the following proportionality holds true [5]:

$$\sigma^{\text{pho}} \propto \frac{Z^5}{E^{3.5}}.\tag{2.24}$$

Note that in the case of very hard X-rays the photoelectric cross section is proportional to Z^5E^{-1} . In comparison to Eq. 2.24, the phase-shift cross section is directly proportional to the atomic number and decreases only linearly with photon energy by

 $\sigma^{\rm pha} \propto \frac{Z}{E}.$ (2.25)

This distinct difference in energy dependence renders phase-sensitive techniques beneficial for soft-tissue (low Z materials) imaging applications such as mammography: one possibility to reduce the radiation dose is to increase the mean X-ray energy. While the absorption cross section is rapidly decreasing, hence a deposition of radiation dose within the breast minimized, the phase-shift cross section remains nearly unaltered. Besides, exhibiting a "beneficial" energy dependence, phase-sensitive imaging further profits from an intrinsically increased contrast generation: δ strongly exceeds the corresponding β with respect to the absolute value, e.g. in the case of water the ratio of the latter amount to up to four orders of magnitude (Fig. 2.2b).

The Compton scattering cross section $\sigma^{\rm com}$ can be obtained by multiplying the relativistic Klein–Nishina cross section with the number of interacting electrons Z and is therefore proportional to

$$\sigma^{\rm com} \propto \frac{Z}{E + m_e} \stackrel{E \ll m_e}{\propto} Z,$$
 (2.26)

where m_e denotes the electron rest mass [6]. Note that within the energy regime investigated here, which is well below the rest energy of an electron, the Compton σ^{com} and phase-shift cross section σ^{pha} yield both a linear dependency in Z. This circumstance is of major importance for the multi-modality of phase-sensitive imaging. In the case of low X-ray energies, absorption-based and phase-sensitive imaging yield complementary images, since probing intrinsically different contrasts. In the case of high X-ray energies, i.e. when the Compton effect prevails the total absorption cross section, this complementarity is lost in a step-wise manner, as Eq. 2.26 shows that both cross sections only rely on the electron density of the probed sample. Nevertheless, phase-sensitive imaging is still attractive at very hard X-rays, since δ is decreasing much slower than β with respect to photon energy [7].

2.2 Grating-Based Imaging

2.2.1 The Talbot Effect

In the year 1836 Henry Fox Talbot discovered that periodically absorbing structures (like gratings) produce a self-imaging phenomenon if illuminated with coherent, visible light. Hereby, the induced intensity modulations re-occur after certain propagation distances (Talbot distances) downstream of the absorber in beam direction [8]. Lord Rayleigh analytically demonstrated that the Talbot effect arises from Fresnel diffraction (near-field diffraction) and that the full Talbot distance d_T is determined by

$$d_T = \frac{\lambda}{1 - \sqrt{1 - \frac{\lambda^2}{p_1^2}}},\tag{2.27}$$

where λ denotes the wave length of the illuminating ray and p_1 corresponds to the period of the absorbing structure [9]. In the case of X-rays, λ ranges in between 0.1 and 100 Å, and hence is much smaller than the period of gratings implied for phase-sensitive imaging, which are typically in the size of microns. Thus, the Taylor series expansion can be used to approximate the square root in Eq. 2.27, resulting in a Talbot distance of

$$d_T = \frac{\lambda}{1 - \left(1 - \frac{\lambda^2}{2p_1^2}\right)} \stackrel{\lambda \ll p_1}{=} \frac{2p_1^2}{\lambda}.$$
 (2.28)

An intuitive verification of the Talbot effect can be given by calculating the propagation of a plane wave $\Psi_0(x)$, which impings on a binary grating, dependent on the propagation distance z, using the Fresnel transform

$$\Psi_z(x) = \mathcal{F}^{-1}[\hat{P}_z(k_x)\mathcal{F}[\Psi_0(x)]]. \tag{2.29}$$

Here $\hat{P}_z(k_x)$ denotes the Fresnel propagator function, which is given as

$$\hat{P}_{z}(k_{x}) = e^{ikz}e^{-izk_{x}^{2}/2k}, \tag{2.30}$$

where k_x and k are the x-component and the norm of the wave vector, respectively [10]. Further, the Fourier transform of the periodic wave function $\mathcal{F}[\Psi_0(x)]$ can be considered as a sum of delta-functions, which are only non-zero at frequencies k_x , that are multiple integers m of the term $2\pi/p_1$. Hence we can simplify Eq. 2.29 to

$$\Psi_z(x) = \Psi_0(x)\mathcal{F}^{-1}\left[\hat{P}_z\left(k_x = \frac{2\pi m}{p_1}\right)\right].$$
 (2.31)

Considering the case that the propagation distance z equals one full Talbot distance d_T , the modified Fourier space propagator function of Eq. 2.31 can be re-written as

$$\hat{P_{d_T}}\left(k_x = \frac{2\pi m}{p_1}\right) = \underbrace{e^{ikd_T}}_{\text{[phase-factor]}} \underbrace{e^{-i2\pi m^2}}_{\text{[1]}}.$$
 (2.32)

Hence $\hat{P_{d_T}}(k_x = \frac{2\pi m}{p_1})$ corresponds to a constant phase-factor only, that is independent from both k_x and m, i.e. does not alter the amplitude/intensity of the wave. Consequently the incident wave-front repeats itself with a periodicity of d_T .

Since absorption gratings reduce the photon flux by a factor of two, which is undesirable for imaging with respect to scan time and radiation dose, it is beneficial to use phase-shifting gratings. Here the wave-front is "patterned" by alternatingly shifting its phase, rather than attenuating its amplitude [11, 12]. It is important to note that, when using a phase-shifting grating, the imprinted phase modulation does not imply an immediate change in wave-amplitude, but instead is converted into an intensity modulations downstream the grating. Thereby maximal intensity modulations are found for so-called "fractional Talbot distances" [13, 14]. Here the phase grating functions as a beam-splitter, which diffracts the incoming X-ray beam into "sub-bundles" that yield diffraction orders of mostly -1 and 1 (The unperturbed wave yields the order 0, respectively). Correspondingly, the divided beams can then reinterfere at these fractional Talbot distances d_n , which are dependent on the imprinted phase-shift by

$$d_n = \begin{cases} n \frac{p_1^2}{8\lambda} = n \frac{d_T}{16} & \text{for } \pi\text{-shift, } n = 1, 3, 5 \dots \\ n \frac{p_1^2}{2\lambda} = n \frac{d_T}{4} & \text{for } \frac{\pi}{2}\text{-shift, } n = 1, 3, 5 \dots \end{cases}$$
(2.33)

Contingent on Eq. 2.7 a desired phase-shift of $\Delta\Phi=\pi$ or $\Delta\Phi=\pi/2$ can be achieved by tuning the sample material and its thickness according to the respective X-ray design energy. Typically, materials with a high electron density are used, among others nickel and gold, to relax requirements with respect to the material thickness, i.e. grating height. The aforementioned interference effect can be visualized by simulating the propagation of a fully coherent wave-front after transversing a phase grating. Figure 2.3a, b show the so-called "Talbot carpet" in the case of a $\pi/2$ -shifting and π -shifting grating with a duty-cycle of 0.5 (phase-shifting material incorporates a width of $p_1/2$) up to a propagation distance of one full Talbot distance d_T , respectively. Maximum beam interference comes to existence for odd numbers of n only, as indicated by dashed lines. In the case of a $\pi/2$ -shifting grating the 1st (n=1) and 3rd (n=3) fractional Talbot distances are displayed. Further, the interference pattern yields a longitudinal periodicity of $d_T/4$ and a transversal periodicity p_t of p_1 . In contrast, in the case of a π -shifting grating the longitudinal and transversal periodicity are quartered and halved, respectively, and given as

$$p_t = \begin{cases} \frac{p_1}{2} & \text{for } \pi\text{-shift} \\ p_1 & \text{for } \frac{\pi}{2}\text{-shift} \end{cases}$$
 (2.34)

Note that the displayed Talbot carpets correspond to a mono-energetic and spatially coherent wave-front. In the case of a source with limited transverse (extended source

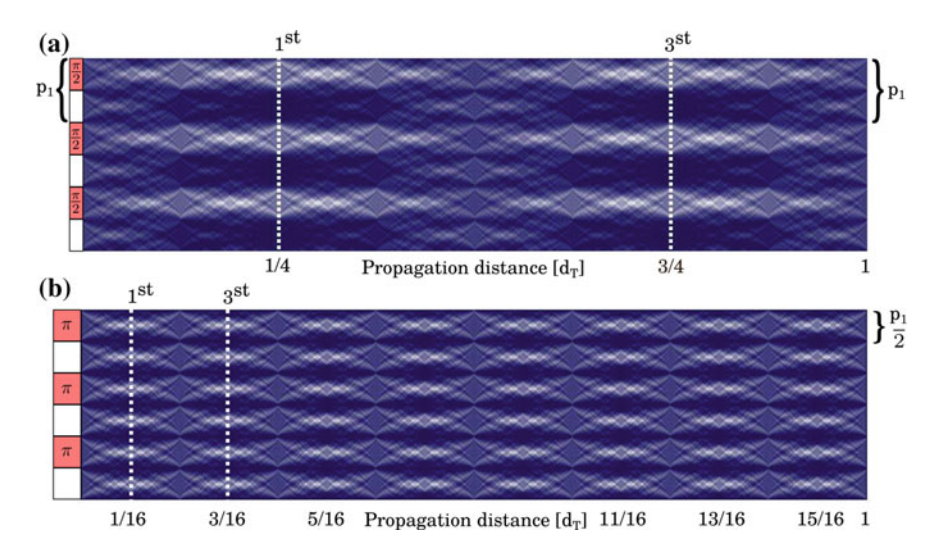


Fig. 2.3 Talbot carpets of coherently illuminated phase-shifting gratings. Talbot carpet generated by a $\pi/2$ -shifting (**a**) and π -shifting phase grating (**b**), yielding maximal intensity modulations at fractional Talbot distances d_n , as exemplarily indicated by *dashed lines*. Note that the period of the evoked intensity modulation p_t is halved in the case of a π -shifting phase grating. Figure adapted from Weitkamp T. et al. (2006) [13]

size) and temporal coherence (finite bandwidth), the Talbot carpet is blurred with increasing propagation distance and is given as superposition of energy-dependent contributions, respectively [15, 16].

2.2.2 X-Ray Talbot Interferometry

As calculated above (cf. Eq. 2.15), typical refraction angles induced by soft-tissue components are in the regime of micro-degrees. Hence, when using clinical detectors with pixel-sizes of hundreds of microns together with a compact setup geometry, the aforementioned refraction and small-angle scattering effects remain unnoticed. The basic idea of a Talbot grating interferometer is to track changes of the interference pattern (as described in Sect. 2.2.1) when introducing a specimen into the beam path, and relate these to the intrinsic sample properties [17]. This approach is practicable only if the interference pattern itself yields transverse intensity modulations, which are of the same order of magnitude as the evoked alternations. According to Eq. 2.34, this requirement can be fulfilled by using phase gratings with periods in the range of (sub)-microns [18].

While it is possible to directly resolve the intensity pattern with a high-resolution detector, the obtainable field-of-view is very limited, contingent on the fact that the usage of high-flux point sources is assumed [19]. In order to overcome this constraint,

(2.35)

i.e. to accurately sample the intensity modulations and quantify the impact of the specimen on the interference pattern with a coarsely-pixelated detector, a second so-called "analyser" grating with period p_2 , is implemented downstream the X-ray beam [20]. By moving the analyser grating perpendicular to the propagation distance over one full grating-period the intensity pattern can be sampled step-wise, which is referred to as the phase-stepping scan [21]. It is of crucial importance that the analyser grating is placed at a fractional Talbot distance d_n so that the reference pattern yields maximal intensity modulations and respective alternations of the latter can be tracked accurately. Further the analyser grating has to be matched with the transverse periodicity of the interference pattern

 $p_2 \stackrel{!}{=} p_t$.

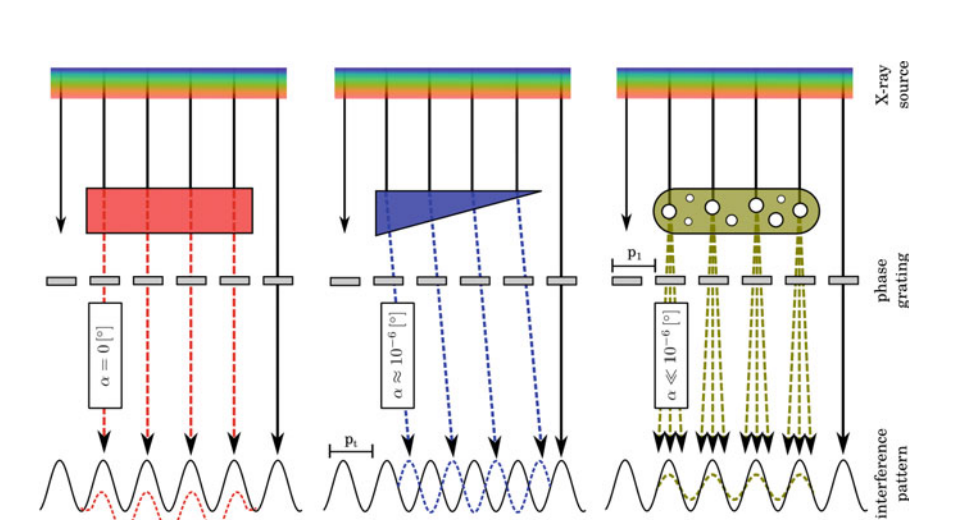


Fig. 2.4 Working principle of a Talbot grating interferometer. A phase grating creates an interference pattern with transverse intensity modulations downstream of the interferometer, arising from the Talbot self-imaging effect. When introducing a specimen the wave-front experiences local distortions, that result in changes of the intensity pattern: decrease of the overall (mean) intensity of the inference pattern, due to absorption ($red\ block$). Transverse shift of the interference pattern due to wave-refraction ($blue\ prism$). Decrease of the interference pattern amplitude, contingent on a loss of local coherence, due to diffuse, uncorrelated small-angle scattering ($green\ oval$). Since the evoked alternations are in (sub)-micron regime an analyser grating is implemented to precisely track the latter, if clinical detectors with a limited spatial resolution are utilized. Note that the angle α is given as a rough estimate, which is dependent on the sensitivity of the interferometer. Further the interference pattern is sine-shaped, since a X-ray generator with extended source size is assumed

Figure 2.4 gives an overview on how a specimen can alter wave-characteristics of an impinging X-ray beam, alongside with the accompanied changes introduced to the interference pattern.

Wave modifications

- Decrease of the overall (mean) intensity of the inference pattern due to absorption, as indicated by the red block.
- Transverse shift of the interference pattern, due to local refraction, as indicated by the blue phase prism.
- Decrease of the interference pattern amplitude, caused by a loss of local coherence due to small-angle scattering, as indicated by the green oval.

Note that small-angle scattering can be considered as a beam refraction process which however surpasses the sensitivity of the interferometer. In comparison to phase-shift related beam deviations, small-angle scattering yields uncorrelated, diffuse angular deflections of very small magnitude, which results in a "smearing" rather then shifting of the interference pattern, attributed to a local degradation of wave-front coherence.

2.2.3 Phase-Stepping

Within the phase-stepping scan either of the gratings is moved over one full grating period perpendicular to the beam direction and multiple images are taken at intermediate grating positions x_g . One can easily imagine that the phase-stepping curve yields minimal intensity, if the absorber grating bars superimpose the interference pattern maxima and yields a maximum, if the latter are conveniently displaced by half a grating period. To assure a meaningful sampling of the interference pattern a sufficient attenuation of the X-rays is required. Therefore the analyser grating is typically made of highly absorbing materials such as gold, with grating heights of $50-160 \,\mu\text{m}$. Such microstructures can be fabricated by applying deep-etching or photolithography to a substrate layer, i.e. definition of the grating pattern, followed by a subsequent filling of the mask with the desired material via electro plating (a detailed description can be found in David C. et al. (2007) [22]).

In the case of an idealized illumination the interference pattern features an intensity modulation that is box-shaped (as sketched in Fig. 2.3). Correspondingly the phase-stepping curve yields a triangular shape if sampled (convoluted) with an analyser grating that exhibits a flat-top absorption profile. However, considering that X-ray sources have a finite source size, which can be modelled by a Gaussian distribution, the generated intensity modulations and phase-stepping curve exhibit a wave- and sine-shape, respectively. Figure 2.5 shows the respective phase-stepping curves of a blank scan (solid line), which maps the pure interference pattern and a respective sample scan (dashed line) sampling the interference pattern, which is modified

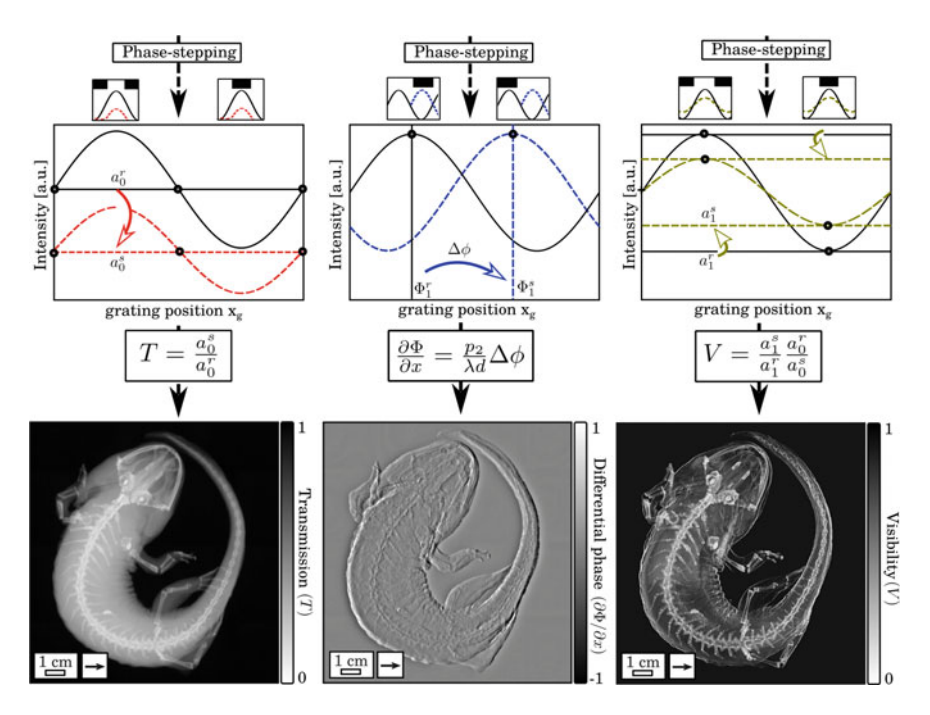


Fig. 2.5 Retrieval of the trimodal image contrast via phase-stepping. In order to precisely analyse and record the interference pattern, one of the two gratings is subsequently moved in a step-wise manner perpendicular to the alignment of the grating bars. By comparing the flat-field (blank line) and sample phase-stepping curve (dashed line) through Fourier analysis, the transmission image T, differential phase signal $\frac{\partial \Phi}{\partial x}$ and the visibility map V of the specimen can be simultaneously retrieved. Following clinical conventions the absorption and dark-field image are displayed, which are derived as transmission and visibility signal with an inverted gray-scale, respectively

by attenuation, refraction and small-angle scattering processes. In order to utilize grating-based imaging with clinical, large field-of-view detectors, a reference scan over the full active imaging area (flat-field) is conducted prior to measurements, in order to account for imperfections, such as Moiré Fringes (see Chap. 3) and an irregular beam illumination.

The intensity $I(x_g, x, y)$ measured during a phase-stepping scan at interlaced grating positions x_g , can be described using a Fourier-series

$$I(x_g, x, y) = \sum_{n=0}^{\infty} a_n(x, y) \cos\left(2\pi n \frac{x_g}{p_t} - \phi_n(x, y)\right),$$
 (2.36)

where x, y denote the detector coordinates and a_n , ϕ_n are the amplitude and phase coefficients, respectively. In the case of limited beam coherence, where the projected source size s^* itself is not significantly smaller than the interference pattern period p_t , it is sufficient to consider only the first two order terms $(n \le 1)$ [23]:

$$I(x_g, x, y) \stackrel{s^* \ge \frac{p_t}{2\pi}}{=} a_0(x, y) + a_1 \cos \left(2\pi \frac{x_g}{p_t} - \phi_1(x, y) \right). \tag{2.37}$$

Here, the projected source size s^* is defined as

$$s^* = s \frac{d}{L},\tag{2.38}$$

where s is the source size, l' is the distance between the X-ray source (see also Sect. 2.2.5) and phase grating, and d the distance between phase and analyser grating, respectively (note that the phase grating is considered as a "sample" in this case). When using conventional X-ray sources, where the aforementioned condition $s^* \geq \frac{p_l}{2\pi}$ holds true, the phase-stepping curve is consequently of sinusoidal shape (oscillation amplitude a_1 , phase ϕ_1) additionally yielding an offset a_0 . The "quality" of the interference pattern, which is an important performance parameter of the grating interferometer, is given by how pronounced the intensity oscillation a_1 is in comparison to the mean intensity value a_0 . This parameter is associated with the so-called "flat-field visibility" V^r , i.e. normalized oscillation amplitude, by

$$V^{r}(x, y) = \frac{a_1(x, y)}{a_0(x, y)}.$$
 (2.39)

From an analytic point of view at least three data points have to be acquired, for the purpose of accurately fitting the stepping curve with a sine-function. To enhance computing speed the retrieval of the phase-stepping curve is typically implemented via Fourier analysis.

2.2.4 Contrast Retrieval

Since soft-tissue samples generally attenuate, refract and scatter an incident beam at the same time, it is necessary to retrieve and separate the underlying contributions from a single phase-stepping curve. In the following the superscript (r) and (s) denote the curve parameters related to the reference (flat-field) and sample scan, respectively.

Absorption

The transmission *T* through a sample is given by the relative decrease of the curve's mean intensity, determined by the ratio of the zero-order Fourier coefficients, by

$$T(x, y) = \frac{a_0^s(x, y)}{a_0^r(x, y)}. (2.40)$$

Further, following Eq. 2.6 the transmission shows an exponential behaviour and can be related to the linear attenuation coefficient μ of a sample by

$$T(x, y) = e^{-\int \mu(x, y, z)dz}$$
. (2.41)

Within this thesis—following clinical conventions—the absorption image *A* rather than transmission image is displayed and is given by

$$A(x, y) = 1 - T(x, y), \tag{2.42}$$

i.e. by inverting the gray-scale of the transmission image, strongly absorbing structures yield high image signal and are color-coded white on a non-absorbing, black background.

• Differential phase

The transverse shift S introduced to the interference pattern by a refracting sample, is given by the radian measure, hence obtained by the multiplication of the refraction angle α (small-angle approximation) and the inter-grating distance d, as

$$S(x, y) = d\alpha. (2.43)$$

Accordingly, the transverse shift S is converted into a displacement of the stepping curve, namely phase position $\Delta \phi$, which is encoded by the analyser grating and dependent on its period p_2

$$\Delta\phi(x,y) = \phi_1^s(x,y) - \phi_1^r(x,y) = 2\pi \frac{S(x,y)}{p_2}.$$
 (2.44)

In Sect. 2.1.3 we demonstrated that a variation (perpendicular to the propagation distance) in the decrement of refractive index of a specimen imposes local variations on the phase of the penetrating wave. Further these are directly proportional to the angle, by which the transmitted wave is refracted. Combination of Eqs. 2.12, 2.43 and 2.44 shows that the retrieved signal maps the differential-phase of the refracted wave and the differential, projected decrement of refractive index of the sample, by

$$\frac{\partial \Phi(x, y)}{\partial x} = k \frac{\partial}{\partial x} \int \delta(x, y, z) dz = \frac{p_2}{d\lambda} \Delta \phi(x, y). \tag{2.45}$$

Dark-field

The local scatter power of a sample is given by the relative decrease in the normalized oscillation amplitude, hence can be calculated from the ratio of sample and reference visibility, using

$$V(x,y) = \frac{V^s(x,y)}{V^r(x,y)} = \frac{a_1^s(x,y)}{a_1^r(x,y)} \frac{a_0^r(x,y)}{a_0^s(x,y)}.$$
 (2.46)

In analogy to the absorption signal, the dark-field image D is obtained as

$$D(x, y) = 1 - V(x, y), \tag{2.47}$$

i.e. corresponds to the visibility map with inverted gray-scale. Strongly scattering structures yield high image signal and are color-coded white on a non-scattering, black background.

The dark-field image maps (incoherent) ultra-small and small-angle scattering of a sample incorporating high density fluctuations on the (sub)-micron scale [24]. It is of major importance that the imaging sensitivity itself is decoupled from the actual, spatial resolution of the interferometer. This so-called "sub-resolution sensitivity" hence enables the retrieval of microstructural properties of a specimen using clinically compatible pixel sizes. This circumstance is illustrated by Fig. 2.6. Here, the visibility signal is simulated for different numbers and sizes of calcium-oxalate grains on the supposition that the overall volume of calcium-oxalate is fixed [25]. While the transmission is constant for all different configurations, contingent on an unaltered amount of attenuating material, the most pronounced dark-field signal is found for calcium oxalate grains, that exhibit sizes similar to the analyser grating period p_2 . Correspondingly, grain sizes strongly exceeding p_2 , evoke scattering with diffraction angles being too small for causing sufficient loss in beam coherence. Besides, the dark-field image is found to exhibit an exponential dependence, if the angular scattering distribution is Gaussian shaped [26]. Hence, by introducing the linear diffusion coefficient ϵ —in analogy to the linear attenuation coefficient μ —the visibility signal is given by

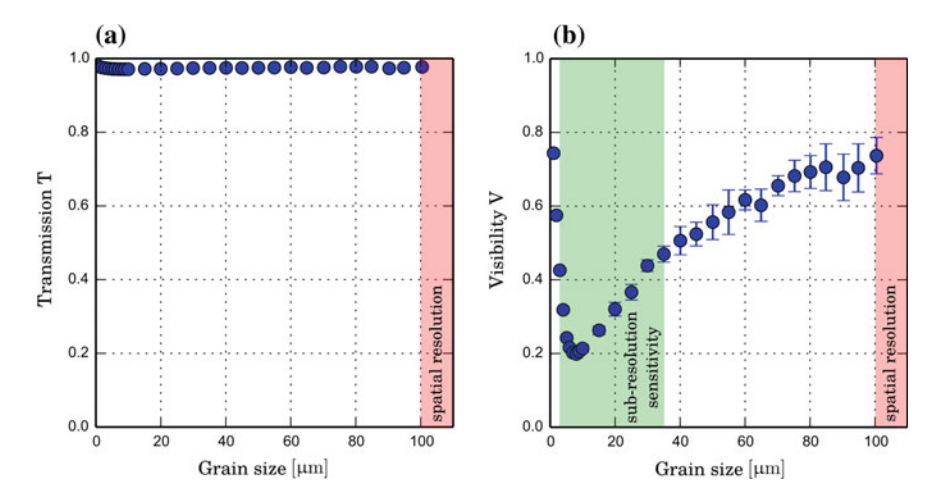


Fig. 2.6 Sub-resolution sensitivity of grating-based dark-field imaging. **a** Transmission and **b** visibility signal simulated for an assembly of calcium grains with varying grain size. The overall amount of calcium, given by the number and size of grains, is fixed for all configurations. The absorption signal is non-sensitive towards variations in the grain size. In comparison, the visibility signal yields a minimum for grains which are similar in size to the analyser grating period (green), even if strongly exceeding the spatial resolution (red) of the interferometer. Hence, dark-field imaging provides an efficiency gain in terms of spatial sensitivity by two orders of magnitude

$$V(x, y) = e^{-\frac{2\pi^2 d^2}{p_2^2} \int \epsilon(x, y, z) dz},$$
(2.48)

where $\frac{2\pi^2 d^2}{p_2^2}$ corresponds to a setup-specific pre-factor. More precisely, Strobl et al. showed that the inter-grating distance, beam energy and analyser grating period determine the so-called "autocorrelation length" of the interferometer [27]. By adapting the latter the sensitivity towards certain sized scattering structures and therewith clinical applications can be tuned to a certain extent. In Chaps. 6 and 8, we utilize the circumstance that both the dark-field and absorption signal yield an exponential dependence for the quantitative (thickness-independent) retrieval of microstructural properties of microcalcifications and kidney stones, respectively. A more detailed investigation of the origin of the dark-field contrast and its dependence on sample properties can be found in Yashiro W. et al. (2010) [28].

2.2.5 Adaptations for Clinical Use

2.2.5.1 Incoherent X-Ray Sources

As stated above, the flat-field visibility V^r of a grating interferometer is an important performance parameter and is preferably tuned as high as possible. Firstly, a high visibility provides a large dynamic range for the detection of scattering until the signal saturates, i.e. the retrieval of the phase-stepping curve is only practicable if V^r is different from zero. Secondly, the photon noise of the measured differential phase scales linearly with the visibility; hence the differential-phase channel exhibits a contrast-to-noise ratio that is directly proportional to the interferometer visibility [29].

The theory presented in the last section assumed a fully coherent and parallel beam illumination, which however is not provided by compact X-ray tubes as used in clinical practice. In case of the latter an extended source size *s* with strongly limited transverse beam coherence is inherent, which ad-hoc prevents the Talbot interference effect to appear. A detailed theory on optical coherence can be found in Born M. et al. (1999) [30].

Transverse Coherence (Extended Source)

This is intuitively comprehensible, considering the extended source size s as an array of independent point sources as schematically depicted in Fig. 2.7a. Following Eq. 2.38, all of these create interference patterns at the analyser grating plane, which are displaced with respect to each other up to a distance equal to the projected source size s^* . If the transverse displacement between two interference patterns is nonnegligible in comparison to the period of the intensity modulation p_t , the intensity oscillations are superimposed in a destructive manner, resulting in a smearing out of the combined interference pattern. More precisely, the (flat-field) visibility in case of monochromatic illumination is determined by the convolution of source size and

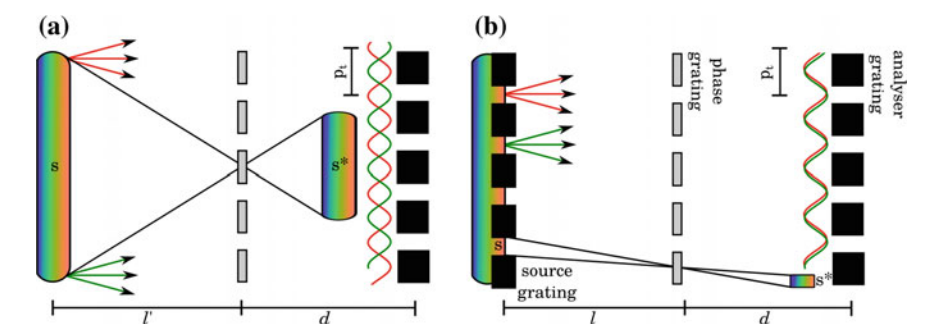


Fig. 2.7 Talbot interferometry using incoherent X-ray sources. **a** An extended sources size creates multiple interference patterns at the analyser grating plane, which are shifted against each other up to a distance of the projected source size s^* . If s^* exceeds the period of the intensity modulations p_t , the shifted patterns overlap in a destructive manner, resulting in a visibility being zero as exemplarily indicated by the *red* and *green curve*. **b** By implementing a highly absorbing source grating the extended source size is shaped into an array of fine slit sources, where each of the latter meets the coherence requirements. As a consequence, the generated intensity modulations overlap in a constructive manner as indicated by the *red* and *green curve*

interference pattern and is analytically described by [23]

$$V^{r}\left(\frac{s^{*}}{p_{t}}\right) = \frac{8}{\pi^{2}} e^{-2\pi^{2} \left(\frac{s^{*}}{p_{t}}\right)^{2}}.$$
 (2.49)

For projected source sizes being equal to or exceeding half the period of the interference pattern the visibility can be considered as zero, as exemplarily indicated in Fig. 2.7a. Hence to render phase-sensitive imaging with a Talbot interferometer possible, the projected source size s^* needs to be considerably small in comparison to p_t and p_2 , respectively

$$\left[s^* = s\frac{d}{l'}\right] \stackrel{!}{\ll} \frac{p_t}{2}.\tag{2.50}$$

This requirement is fulfilled for synchrotron beam-lines, which provide a high spatial and temporal coherence, however are space- and cost-intensive facilities. While micro-focus X-ray tubes can provide sufficiently small focal spots, they only yield little photon flux, a limited anode current and power output, and hence are only suitable for the investigation of optically thin samples. Finally, a small projected source size can also be achieved by tuning the *d*-over-*l'* ratio, for instance by increasing the distance between X-ray source and the phase grating. This however comes at the expense of extending the setup and reducing the photon flux per solid angle.

To overcome this restriction and to utilize phase-sensitive imaging within a clinical environment (compact systems, high-power sources with intrinsically large focal spots $\geq 100 \,\mu$ m, short exposure times), a third so-called "source" grating with period p_0 is introduced just downstream the X-ray emission source, which decouples the

source size from the spatial coherence constraint [31]. Similar in design to the analyser grating, the source grating preferably exhibits a flat-top attenuation profile, by which the extended source is shaped into an array of fine slit sources. Here each slits meets the transverse coherence requirement given by Eq. 2.50. By matching the projected periodicity of the source grating p_0^* with the analyser grating period p_2

 $\[p_0^* = p_0 \frac{d}{l} \] \stackrel{!}{=} p_2, \tag{2.51}$

where l denotes the distance between source and phase grating, the evoked interference modulation superimpose in a constructive manner at the detector plane as schematically shown in Fig. 2.7b. This effect is known as "Lau-effect", which is why a three grating interferometer is referred to as a "Talbot–Lau interferometer". Note that the effective spatial resolution of the system, i.e. sample magnification, is not altered by the presence of the gratings, but instead is determined by the projected source size, the sample position and the detector characteristics.

Temporal Coherence (Finite Bandwidth)

In comparison to the strict requirements for spatial coherence, Talbot–Lau Interferometry is compatible and successfully operated with temporally incoherent X-ray sources. However, since the phase-shift and the Talbot distances are wavelength dependent, the resulting Talbot carpet is blurred in the case of polychromatic illumination, given as a superposition of multiple, longitudinally displaced interference patterns. The visibility spectrum, which describes to what extent certain X-ray wavelengths contribute to the overall fringe visibility, thus needs to be matched to the utilized X-ray source spectrum.

To maximize the interferometer visibility the implemented gratings need to meet the following design criteria [32]:

- 1. The phase grating design energy must be matched to the mean X-ray energy in both the sample and flat-field scan.
- 2. The absorber gratings must block high energy parts of the X-ray spectrum to a sufficient extent. Note that this is of special importance in the case of integrating detectors, which give high energy photons more weight.

Since the visibility spectrum furthermore is dependent on the imprinted phase-shift as well as the Talbot-order, following considerations are essential:

- 3. In the case of high fractional Talbot-orders (n > 3) a π -shift is favourable, since the visibility spectrum yields only positive contributions. Contrasting, in the case of a $\pi/2$ -shifting grating, the evoked intensity modulations are alternating out-of-phase, resulting in a cancellation of visibility contributions.
- 4. In the case of low fractional Talbot-orders ($n \le 3$) a $\pi/2$ -shift is favourable, being less sensitive to variations in the duty-cycle as in comparison to a π -shift.

2.2.5.2 Cone-Beam Geometry

Since mammography systems require a large field-of-view at a compact system length, a divergent beam is inherent and magnification effects need to be considered. Above derived equations assumed a fully parallel beam and need to be refined if the geometrical magnification of an interferometer is different from unity. In the case of cone- or fan-beam geometry the interference pattern experiences a magnification in lateral direction, which has to be matched by the analyser grating period as indicated by the superscript $\binom{M}{2}$. The interference pattern magnification M is given by

$$M = \frac{d+l}{l},\tag{2.52}$$

with d and l being the inter-grating distances as depicted in Fig. 2.7b. Following Eqs. 2.34 and 2.35, the requirements with respect to the magnified interference pattern p_t^M and adapted analyser grating period p_2^M are fulfilled, if

$$p_2^M \stackrel{!}{=} p_t^M = Mp_t = \begin{cases} M\frac{p_1}{2} & \text{for } \pi\text{-shift} \\ Mp_1 & \text{for } \frac{\pi}{2}\text{-shift} \end{cases}$$
 (2.53)

holds true. Furthermore, the (fractional) Talbot distances d_n^M are increased in longitudinal direction by

$$d_n^M = Md_n. (2.54)$$

Finally, contingent on Eq. 2.51 the period of the source grating needs to be adapted to

$$p_0^M \stackrel{!}{=} p_2^M \frac{l}{d}. {(2.55)}$$

Note that a cone-beam setup exhibits further challenges which need to be addressed. The cone-beam is shadowed in the outer regions of the source and analyser grating, where grating bars are not parallel to the beam path. Correspondingly, within the affected areas the beam intensity is reduced, noise increased and the X-ray spectrum hardened, respectively. Besides, with increasing beam divergence, the effective grating profile is flattened, which results in a loss of visibility [33].

2.3 The Female Breast

2.3.1 Breast Anatomy

The female breast is a complex organ comprising, among others, mostly adipose and glandular tissue, as schematically depicted in Fig. 2.8a. Overlaying the pectoralis

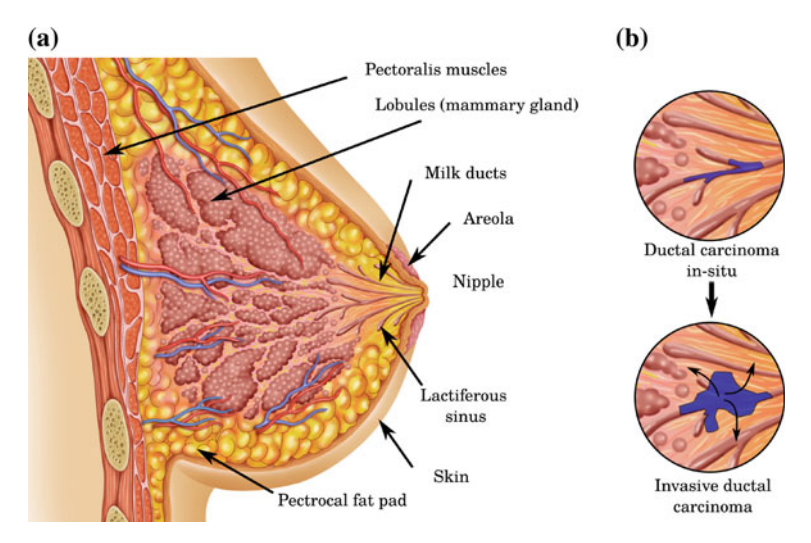


Fig. 2.8 Anatomy of the female breast. a Sketch of the female breast with mammary gland, lobules and ducts being embedded within adipose tissue. Figure adapted from Lynch, J. (2007) [36]. b Soft-tissue breast cancer mostly occurs within the milk ducts or within the lobules. Pre-invasive, so-called "in-situ" lesions are confined to inner compartments of the ducts, albeit bear a high risk of developing into invasive carcinomas

major muscle, the breast consists of a core of 14–18 lactiferous lobes. These are interconnected with the nipple by multiple milk ducts, which are 2–4.5 mm in diameter. Each lobe itself is composed of 20–40 terminal ductal lobular units, which are responsible for the generation of the fatty breast milk. The mammary gland is supported by a framework of connective tissue, comprising collagen, elastin and white fat. Further so-called "Cooper's ligaments", which are fibrous-tissue prolongations, perfuse from the muscle to the skin, maintaining the firmness and shape of the breast. The glandular tissue core is embedded in subcutaneous adipose tissue and a superficial tissue layer [34].

The (optical) density of the female breast highly varies interindividually, mainly depending on age and hormonal factors like menopausal state or external hormone replacement therapy. Usually, in the case of young women breast tissue is highly (optical) dense, contingent on a prevailing amount of glandular tissue. This circumstance and the higher sensibility of the breast towards X-rays in young women, render this group rather unsuitable for screening mammography. In postmenopausal women however, the ovarian estrogen production decreases. Since the estrogen functions as a biochemical stabilizer of glandular tissue, the latter withers and a subsequent replacement with adipose tissue occurs. Note that the fatty degeneration of elderly breasts is the decisive point in the diagnostic performance of mammography, enabling an easy detection of soft-tissue lesions in the otherwise fatty tissue. According to the American College of Radiology (ACR) four different breast density types are

2.3 The Female Breast 31

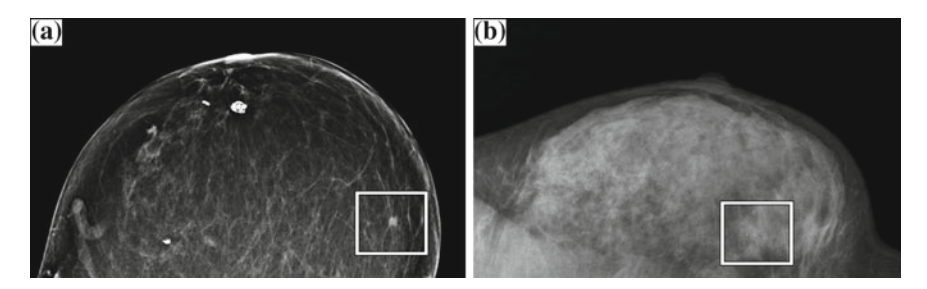


Fig. 2.9 *Mammographic appearance of ACR 1 and ACR 3 breasts.* **a** Clinical in-vivo mammogram of an entirely fatty breast (ACR 1) in craniocaudal (CC) view. Note that the tumor nodule (*white frame*) can be easily differentiated from the surrounding adipose tissue as a strongly absorbing spot. **b** Clinical in-vivo mammogram of a heterogeneously dense breast (ACR 3) in mediolateral oblique (MLO) view (rotated). Note that the tumorous region (*white frame*) can hardly be differentiated from the surrounding healthy tissue, being superimposed by dense breast tissue, i.e. anatomical noise

distinguished in mammographic examinations [35].

Breast density classification (ACR)

- 1. Fatty—The breast is considered as almost entirely adipose, i.e. the amount of glandular tissue is less than 25 %.
- 2. Scattered fibroglandular—The breast yields a volume of 25–50% of well separated fibrous and glandular tissue.
- 3. Heterogeneously dense—The volume of breast parenchyma accounts to 51–75 %, while the breast exhibits clear features and a distinct tissue variation in the mammogram.
- 4. Extremely dense—Fibroglandular tissue occupies more than 75% of the breast, which results in a homogeneous breast density and poor differentiation of features in the mammogram.

Note that an increased breast density does not only reduce the detection quality of cancer and architectural distortions resulting in a restricted diagnostic accuracy in dense breasts (cf. Fig. 2.9b), but is also associated with an increased risk of developing cancer [37].

2.3.2 Breast Cancer

Breast cancer is the most common type of invasive cancer in woman and accounted for the second most cancer deaths among woman (13.7%) in the year 2008, being of special severity in the 3rd world countries [38]. In low-income countries survival-rates are below 40% in comparison to more than 60% in first world coun-

tries, contingent on a lack of early detection possibilities, with an accordingly high proportion of women presenting with late-stage cancer [39]. The Global Health Estimates (WHO) assessed a number of more than half a million of breast cancer deaths in the year 2011.

Like any other cancer, malignant changes in the breast mainly occur in elderly woman as natural cell processes, where cell repair or apoptosis (process of programmed cell death) are malfunctioning. Here, cells can proliferate and grow in an uncontrolled and disorganized manner. Risk factors promoting breast cancer are among others a lack of physical exercise, drinking alcohol, hormone replacement therapy during menopause and childlessness, family history of breast or ovarian cancer. Of major importance are further mutations in the BRCA1 (Breast cancer antigen 1) and BRCA2 (Breast cancer antigen 2) genes, which are known as the "breast cancer susceptibility proteins" (to a certain extent also the p53 gene), which are responsible for 5-10% of all breast cancer incidents reported and mainly account for breast cancer in young women [40]. These genes are common in mammal species, hence are not of oncogenic nature, but instead function as tumor suppressors within the healthy body [41]. BRCA1 and BRCA2 are part of a complex-group that repairs double-strand breaks in the DNA double helix [42]. Women with a mutated BRCA1/2 gene have a malfunctioning/disabled DNA repair system rendering them exposed to an 80% risk of developing life-time breast and ovarian cancer, depending on the generation on mutating cells.

Most commonly breast cancer originates from cells of the mammary gland, namely ductal and lobular carcinomas. In early or pre-cancerous stages, abnormal cell proliferation is per definition confined to the inner compartments of the ducts and lobules and carcinomas are labelled as "in-situ" (Fig. 2.8b). Although, in-situ indications are considered rather harmless if remaining in their constitution, since patients usually do not develop distant metastases, they yield a high life-time risk of becoming "invasive carcinomas", i.e. bursting the basal membrane and infiltrating surrounding tissue. Development of invasive behaviour is of high diagnostic importance, considering destruction of healthy tissue but also potential dissemination and metastasis formation of cancer cells in the lymph nodes, bones, liver, lung and brain. While an early detection of ductal carcinomas in-situ is hence desirable in young patients, a potential over-diagnosis and treatment of the latter in the case of elderly patient is currently under discussion [43]. This is due to the fact that the development from in-situ into invasive carcinomas may last up to 10 years and older women will not benefit from therapy considering the overall survival. In addition to more then 18 malignant tumor histological types and sub-types also benign changes are found in the female breast such as (fibro-)cystic lumps. The most common mass found in young, adolescent woman are benign fibroadenomas which grow in the terminal duct lobular units of the breast [44]. However, benign changes routinely require little action and excision is only indicated in the case of rapid growth or patient discomfort.

2.3 The Female Breast 33

The treatment and prognosis of breast cancer is versatile and heavily depends on the specific tumor characteristics. Breast cancer diagnosis has a complementary structure: a physical examination is followed by two-field mammography, ultrasound and in certain indications contrast-enhanced MRI. In rare case, e.g. if a dissemination and metastasis formation of the tumor are suspected, an examination with 18F-Fluorodeoxyglucose Positron Emission Tomography may be indicated [45]. In Germany, a biennial screening mammography is recommended for women aged 50–79 (for more details see Chap. 5). The "Breast Imaging Reporting and Data System" (BIRADS), which is the standard risk assessment and quality assurance tool in breast diagnostics, classifies mammographic findings into BIRADS I-VI categories [35].

BIRADS classification (ACR)

- I —negative finding, i.e. no architectural disorder, abnormalities or suspicious microcalcifications are present in the mammogram.
- II —benign finding, including fibroadenomas, oil cysts, lipomas and galactoceles.
- III —Probably benign finding with a low malignancy risk of $\leq 2\%$.
- IV —Suspicious finding with an intermediate malignancy risk of 2–95 %.
- V —Highly suspicious finding with a high malignancy risk of \geq 95 %.
- VI —Histopathologically verified carcinoma.

In the case of a III–V finding, a core or vacuum-assisted biopsy of the suspicious mass is taken under local anaesthesia (guided by mammography or ultrasound) and histopathological work-up is performed. The classification of tumors is complex and comprises a multi-layered assessment. Histologically, different tumor types are defined according to the WHO classification depending from the tissue type they originate from: the most frequent histological type is the invasive ductal carcinoma, not otherwise specified (NST), accounting for 70% of all invasive breast cancers. Less common types are among others the invasive lobular carcinoma, tubular, medullary and mucinous carcinoma [46]. Grading further compares to what extent cancer cells and their core are still differentiated in comparison to healthy cells (well differentiated—low grade, moderately differentiated—intermediate grade, and poorly differentiated—high grade). Breast cancer staging according to the TNM system describes macroscopical properties of the tumor within the breast, including tumor size (T), a potential invasion of the axillary lymph nodes in the armpits (N), and whether the tumor exhibits a metastatic behaviour (M) [47]. Besides, also a description of the tumor cells with respect to their biochemical entities (Receptor status, DNA assays) is available.

Breast cancer therapy is increasingly individualized depending on tumor type and biology, size, nodal state, distant metastases as well as age of the patient. Nevertheless, the standard therapy of breast cancer is the surgical removal of the lesions and, if indicated, an adjuvant or neoadjuvant medication with cytostatica. Although also affecting healthy cells, cytostatica predominately destroy cancerous cells, which

yield a strongly increased self-replication rate. After surgery, radiotherapy may be applied to the surrounding soft-tissue as well as the adjacent lymph nodes with the goal of destroying spread tumor cells and preventing a recurrence of the tumor [48]. In tumors expressing hormonal receptors and/or growth factor receptors, antihormonal and/or antibody therapy is recommended, in which tumor cells are deprived of their basis of cell growth via blocking the production of oestrogen and growth factors.

References

- 1. Als-Nielsen, J., & McMorrow, D. (2011). Elements of modern X-ray physics. Hoboken: Wiley.
- 2. Willmott, P. (2011). An introduction to synchrotron radiation: Techniques and applications. Chichester: Wiley.
- 3. Paganin, D. (2006). Coherent X-Ray optics. Oxford: Oxford University Press.
- Sanchez del Rio, M., & Dejus, R. (2011). XOP v2.4: recent developments of the X-ray optics software toolkit. *Proceedings of SPIE*, 8141, 814115.
- 5. Wang, Y. (2007). Intuitive dimensional analyses of the energy and atomic number dependences of the cross sections for radiation interaction with matter. *Journal of X-Ray Science and Technology*, *15*, 169–175.
- Klein, O., & Nishina, Y. (1929). Über die Streuung von Strahlung durch freie Elektronen nach der neuen relativistischen Quantendynamik von Dirac. Zeitschrift für Physik, 52, 853–869.
- 7. Thüring, T., Abis, M., Wang, Z., David, C., & Stampanoni, M. (2014). X-ray phase-contrast imaging at 100 kev on a conventional source. *Scientific Reports*, 4, 5198.
- 8. Talbot, H. (1836). Facts relating to optical science. Philosophical Magazine IV, 9.
- 9. Edgar, R. (1969). The Fresnel diffraction images of periodic structures. *Optica Acta*, 16, 281–287.
- 10. Saleh, B., & Teich, M. (2007). Fundamentals of photonics. Hoboken: Wiley-Interscience.
- 11. Guigay, J., et al. (1971). On Fresnel diffraction by one-dimensional periodic objects, with application to structure determination of phase objects. *Optica Acta*, 18, 677–682.
- 12. Arrizon, V., & Ojeda-Castaneda, J. (1994). Multilevel phase gratings for array illuminators. *Applied Optics*, *33*, 5925–5931.
- 13. Weitkamp, T., David, C., Kottler, C., Bunk, O., & Pfeiffer, F. (2006). Tomography with grating interferometers at low-brilliance sources. *Proceedings of SPIE*, 6318, 63180.
- 14. Suleski, T. (1997). Generation of Lohmann images from binary-phase Talbot array illuminators. *Applied Optics*, *36*, 4686–4691.
- 15. Xin, L., Jin-Chuan, G., Xiang, P., & Han-Ben, N. (2007). Visibility in differential phase-contrast imaging with partial coherence source. *Chinese Physics*, 16, 1632.
- 16. Hipp, A., et al. (2014). Energy-resolved visibility analysis of grating interferometers operated at polychromatic X-ray sources. *Optics Express*, 22, 30394–30409.
- 17. Momose, A. (2003). Phase-sensitive imaging and phase tomography using X-ray interferometers. *Optics Express*, 11, 2303–2314.
- 18. Wen, H., et al. (2013). Subnanoradian X-ray phase-contrast imaging using a far-field interferometer of nanometric phase gratings. *Nature Communications*, 4, 2659.
- Takeda, Y., et al. (2007). X-Ray phase imaging with single phase grating. *Japanese Journal of Applied Physics*, 46, 89–91.
- 20. Momose, A., et al. (2003). Demonstration of X-Ray Talbot interferometry. *Japanese Journal of Applied Physics*, 42, 866–868.
- 21. Weitkamp, T., et al. (2005). X-ray phase imaging with a grating interferometer. *Optics Express*, 13, 6296–6304.

References 35

22. David, C., et al. (2007). Fabrication of diffraction gratings for hard X-ray phase contrast imaging. *Microelectronic Engineering*, 84, 1172–1177.

- 23. Bech, M. (2009). *X-ray imaging with a grating interferometer*. Copenhagen: University of Copenhagen.
- Pfeiffer, F., et al. (2008). Hard-X-ray dark-field imaging using a grating interferometer. *Nature Materials*, 7, 134–137.
- Malecki, A., Potdevin, G., & Pfeiffer, F. (2012). Quantitative wave-optical numerical analysis
 of the dark-field signal in grating-based X-ray interferometry. Europhysics Letters, 99, 48001.
- Bech, M., et al. (2010). Quantitative X-ray dark-field computed tomography. *Physics in Medicine and Biology*, 55, 5529.
- 27. Strobl, M. (2014). General solution for quantitative dark-field contrast imaging with grating interferometers. *Scientific Reports*, 4, 7243.
- 28. Yashiro, W., Terui, Y., Kawabata, K., & Momose, A. (2010). On the origin of visibility contrast in X-ray Talbot interferometry. *Optics Express*, *18*, 16890–16901.
- 29. Köhler, T., Jürgen Engel, K., & Roessl, E. (2011). Noise properties of grating-based X-ray phase contrast computed tomography. *Medical Physics*, 38, 106.
- 30. Born, M., & Wolf, E. (1999). *Principles of optics—electromagnetic theory of propagation, interference and diffraction of light*. Cambridge: Cambridge University Press.
- 31. Pfeiffer, F., Weitkamp, T., Bunk, O., & David, C. (2006). Phase retrieval and differential phase-contrast imaging with low-brilliance X-ray sources. *Nature Physics*, 2, 258–261.
- 32. Engelhardt, M., et al. (2008). The fractional talbot effect in differential X-ray phase-contrast imaging for extended and polychromatic X-ray sources. *Journal of Microscopy*, 232, 145–157.
- 33. Thuering, T., et al. (2011). High resolution, large field of view X-ray differential phase contrast imaging on a compact setup. *Applied Physics Letters*, 99, 041111.
- 34. Kopans, D. (2006). Breast imaging. Baltimore: Lippincott Williams & Wilkins.
- 35. D'Orsi, C., et al. (2013). ACR BIRADS atlas, breast imaging reporting and data system. Preston: American College of Radiology.
- Lynch, J. (2007). The Breast: cross section scheme of the mammary gland. http://en.wikipedia. org/wiki/File:Breast_anatomy_normal_scheme.png.
- McCormack, V., & Silva, I. (2006). Breast density and parenchymal patterns as markers of breast cancer risk: A meta-analysis. Cancer Epidemiology, Biomarkers and Prevention, 15, 1159–1169.
- 38. World cancer report (2008). (International Agency for Research on Cancer, Lyon, 2008)
- 39. Coleman, M., et al. (2008). Cancer survival in five continents: A worldwide population-based study. *The Lancet Oncology*, *9*, 730–756.
- 40. Campeau, P., Foulkes, W., & Tischkowitz, M. (2008). Hereditary breast cancer: New genetic developments, new therapeutic avenues. *Human Genetics*, 124, 31–42.
- 41. Duncan, J., Reeves, J., & Cooke, T. (1998). BRCA1 and BRCA2 proteins: Roles in health and disease. *Molecular Pathology*, *51*, 237–247.
- 42. Friedenson, B. (2007). The BRCA1/2 pathway prevents hematologic cancers in addition to breast and ovarian cancers. *BMC Cancer*, 7, 152–162.
- 43. Kumar, A., Bhatia, V., & Henderson, I. (2005). Overdiagnosis and overtreatment of breast cancer: Rates of ductal carcinoma in situ: A US perspective. *Breast Cancer Research*, 7, 271–275.
- 44. Jayasinghe, J., & Simmons, P. (2009). Fibroadenomas in adolescence. *Current Opinion in Obstetrics and Gynecology*, 21, 402–406.
- 45. Bellon, J., et al. (2004). Evaluation of the internal mammary lymph nodes by FDG-PET in locally advanced breast cancer. *American Journal of Clinical Oncology*, 27, 407–410.
- Mammakarzinom der Frau: Diagnostik, Therapie und Nachsorge S3 Leitlinie Mammakarzinom. (AWMF, 2012).
- 47. Denoix, P. (1946). Enquete permanent dans les centres anticancereaux. *Bulletin Institut National d'Hygiene*, 1, 70–75.
- 48. Massarut, S., et al. (2006). Intraoperative radiotherapy impairs breast cancer cell motility induced by surgical wound fluid. *Journal of Clinical Oncology*, 24, 10611.

Chapter 3 Experimental Setup and Methods Development

Ein Mann, der recht zu wirken denkt, muß auf das beste Werkzeug halten.

Johann Wolfgang von Goethe

Abstract In this chapter, the development of a compact laboratory grating-based X-ray phase-contrast mammography setup is presented. In order to meet the design criteria of a clinical system, the setup was built from scratch and mainly optimized for full-field imaging. The respective hardware developments and software tools are separately shown in two sections, and provide the reader with comprehensive knowledge on the image acquisition process. With the goal of enabling the very first clinically compatible phase-contrast mammography measurements, the setup was continuously optimized. The latest setup configuration is presented in this chapter, while Chap. 7 illustrates which changes were necessary to facilitate clinical applicability of phase-contrast mammography.

3.1 Phase-Contrast Mammography Setup

The design of the Talbot–Lau interferometer was perceived on the specifications of a conventional system in order to prove clinical transferability of phase-contrast mammography and verify medical significance of the results presented in the further study. A compact layout with a total setup length of approximately 1.6 m (including the detector, excluding the X-ray source), in the third fractional Talbot order (π -shifting) and a design energy of 27 keV was chosen. The respective asymmetric (2:1) inter-grating distances amount to l=100 cm between source G_0 and phase grating G_1 and d=48 cm between phase G_1 and analyser grating G_2 , respectively. The corresponding grating periods are $p_0 = 10 \,\mu\text{m}$, $p_1 = 6.48 \,\mu\text{m}$ and $p_2 = 4.8 \,\mu\text{m}$ (Mikroworks GmbH, Germany). An overview of the current grating specifications is given in Table 3.1. The Nonius FR 591 rotating anode X-ray generator with a molybdenum target is typically operated at $40 \,\text{kVp/70} \,\text{mA}$. The focal spot size is

Parameter	G_0	G_1	G_2
Period [µm]	10	6.48	4.8
Active area [cm]	round, Ø 7	round, Ø 7	round, Ø 10
Active material	Au	Au	Au
Substrate thickness [µm]	200 (Si)	200 (Si)	200 (Si)
Duty cycle	0.51	0.61	0.49
Filling height [μm]	>35	5.2	50

Table 3.1 Overview of grating parameters

Table summarizing the technical parameters of the source G_0 , phase G_1 , and analyser grating G_2 of the phase-contrast mammography setup

approximately $0.3 \times 0.3 \, \text{mm}^2$ at the anode and estimated to $0.15 \times 0.15 \, \text{mm}^2$ at the detector plane, respectively. A distinctively higher peak voltage is chosen than typically utilized for conventional mammography (28–30 kVp), in order to compensate for a loss of flux due to the gratings [1]. Besides no additional k-edge filters are implemented as typically done in mammography (for the purpose of shaping the X-ray spectrum), considering the presence of a total of 600 µm silicon due to grating substrates [2]. In order to avoid severe beam-shadowing at the outer regions of the gratings, gold filling heights of below 50 µm are used, which reason a relatively low interferometer visibility of approximately 18%. Note that 50 µm Au are transparent for 8% of all 30 keV photons. Besides, the source spectrum alongside with the characteristic X-ray lines of 17.5 keV and 19.6 keV strongly differ from the design energy itself, which leaves room for further visibility optimizations. For a detailed discussion find Gromann, L. (2014) [3]. An indirect X-ray conversion Varian Paxscan 2550DX flat panel with DRZ-Plus Gadox screen (Gd₂O₂S : Tb, 208 µm phosphor layer) coupled with a silicon TFT and $127 \times 127 \,\mu\text{m}^2$ -pixel size is implemented as a detector. A Gadox screen was preferred over a Caesium-Iodine screen offering an enhanced sensitivity and detective quantum efficiency for the aforementioned X-ray energy spectrum [4]. The sample was positioned at 2.6 cm directly downstream G_1 in order to optimize the sensitivity of the interferometer [5]. The sample magnification was determined to 1.40, resulting in an effective pixel-size of approximately $91 \times 91 \,\mu\text{m}^2$.

Figure 3.1a shows the current, optimized setup with a dose-saving arrangement of phase grating and breast sample holder. In order to minimize the usage of moving parts, all gratings were fixed with compact mountings, mutually arranged in-line with the center of the X-ray beam. One common center of rotation was defined, to avoid a rearranging of gratings after their alignment. Linear actuators (TRA-series, Newport GmbH, Germany) and rotation/goniometer stages (Newport GmbH, Germany) were implemented to enable rotation around both the z- and y-axis. With the purpose of fine-tuning the inter-grating distance, the phase grating was additionally equipped with a linear stage (Newport GmbH, Germany, Fig. 3.1b), enabling translation in direction of the X-ray beam. Further a nano-converter, operated with a high-load actuator (LTA-series, Newport GmbH, Germany), was used with a gear reduction ratio of

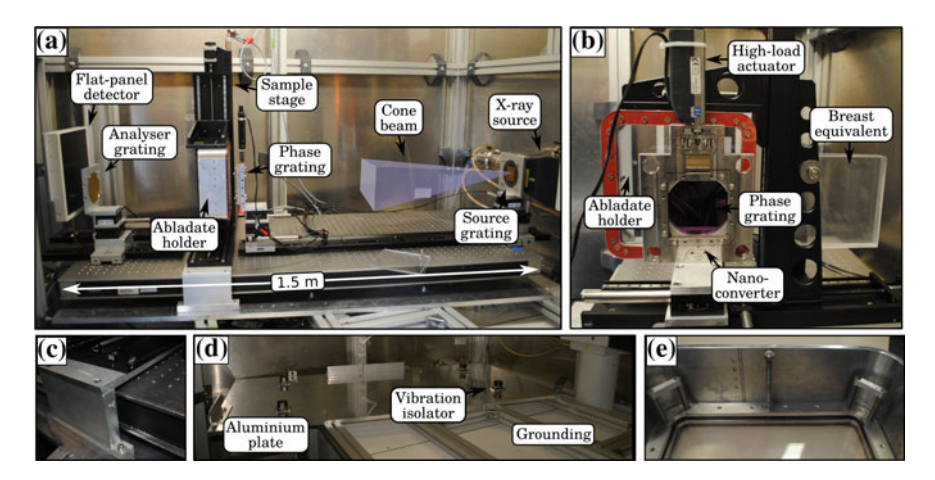


Fig. 3.1 Laboratory X-ray phase-contrast mammography setup. **a** Lateral view of the current laboratory X-ray phase-contrast mammography system with dose-saving arrangement of phase grating and sample holder. A compact system length, rotating X-ray anode and conventional flat-panel detector meet the design criteria of clinical mammography systems. **b** Close-up view in the direction of the X-ray beam showing the phase-stepping instruments and breast equivalent material for flat-field measurements. **c** Bridge construction which decouples the optical table from the sample stage, in order to avoid a tilting of the optical breadboard and transmission of motion-induced vibrations. **d** Aluminium grounding and framework of the interferometer with elastomer vibration isolators. **e** Back view of the sample holder with easy-to-read breast compression thickness ruler

100, to achieve an accurate phase-stepping process. Besides, a breast equivalent (PMMA) was mounted on the posterior side of the sample stage, with the purpose of mimicking the breast tissue during flat-field acquisition. Implementation of the latter allows the retrieval of images, that are free of beam-hardening artefacts, which provides consistency between different data sets, as demonstrated in more detail in Chap. 7.

Two linear stages LT 120 (Owis GmbH, Germany) were combined to enable translation of the sample holder in both x- and y-direction and provide a scan-able area of up to 17×17 cm². To avoid the generation of vibrations and tilting of the optical breadboard, induced by the movement of the linear stages and accompanied weight displacement, the latter was decoupled from the optical table by means of a bridge construction (Fig. 3.1c).

Figure 3.1d shows the grounding of the mammography setup on which the optical table (Thorlabs GmbH, Germany) was placed. In a first step, a framework of aluminium bars was built and connected with the hutch walls. Afterwards, the beam center and the inclination of the X-ray beam were determined using a photosensitive foil. The aluminium plate, which serves as a second grounding, was aligned according to the beam path. Finally, four elastomer vibration isolators (ND01-Series, Newport GmbH, Germany) were mounted to reduce the transmission of high-frequency noise to the interferometer. Note that the vibration isolators were placed on small aluminium blocks of varying thickness to compensate for the inclination of the beam.

To enable a proper fixation of the breast specimen at a medically reasonable sample compression a customized sample holder was designed. Therefore an aluminium frame with corresponding lid was shaped and two polycarbonate windows (thickness of 5 mm each) bordered. These offer a higher rigidity in comparison to PMMA at similar attenuation properties. Figure 3.1e shows the back view of the sample holder with an easy-to-read breast compression thickness ruler (3–6 cm) and bars connected to the lid, which allow a quick disassembly of both parts.

In order to conduct tomosynthesis, the sample stage was additionally equipped with a rotation stage (Newport GmbH, Germany) and connected with the sample holder using a sledge construction. At first an initial full-field radiography of the breast abladate is obtained, by which a region of interest is determined. Afterwards the determined volume is manually moved into the center of rotation using the sledge construction and then tomosynthesis executed.

Prior to measurements the gratings have to be aligned until a preferably flat detector image is obtained. Due to imperfections of the gratings, a remaining tilt as well as the fact that the gratings are planar, hence do not adapt the beam curvature, a complete vanish of Moiré fringes is considered unlikely (for a detailed overview on the generation of Moiré fringes find Chabior, M. (2011) [6]). The following protocol was used for the grating alignment and is partially illustrated in Fig. 3.2.

- 1. The source grating G_0 is solely placed into the beam and rotated around the y-axis, until a Gaussian shaped intensity profile is obtained perpendicular to the grating lines. This way the grating is aligned perpendicular to the beam and shadowing of photons minimized.
- 2. Step #1 is repeated for the analyser grating G_2 , to assure that both absorption gratings are parallel to each other.
- 3. In the next step all gratings, more precisely their bars, have to be aligned vertically, which is achieved by rotating the latter around the *z*-axis. A coarse alignment can be achieved by illuminating the gratings with a laser and adjusting the resulting

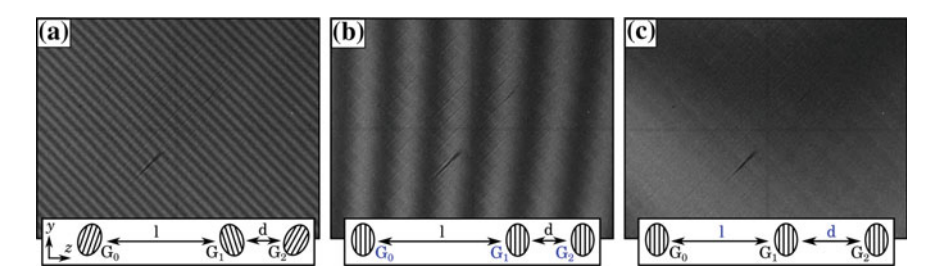


Fig. 3.2 Alignment of gratings and generation of Moiré fringes. **a** If gratings are slightly rotated against each other with respect to the z-axis, multiple tilted Moiré fringes are present in the detector image. **b** After a precise vertical alignment of the gratings, the Moiré fringes yield a mutual vertical orientation. **c** By fine-tuning the inter-grating distance, i.e. ratio between l and d, the period of interference pattern and analyser grating are matched, by which the Moiré fringes vanish and a preferably flat background is achieved

- diffraction patterns on a mutual line. A remaining misalignment of the gratings around the *z*-axis is identifiable by rotated Moiré fringes as shown in Fig. 3.2a.
- 4. Two out of the three gratings are carefully rotated around the *z*-axis until the Moiré fringes exhibit a vertical orientation as shown in Fig. 3.2b.
- 5. If the Moiré fringes vary in thickness from left to right, the phase grating G_1 is misaligned and has to be rotated with respect to the *y*-axis, until an uniform magnification is reached. Note that the phase grating can not be aligned by probing the evoked intensity profile, since the phase-shifting bars are hardly absorbing.
- 6. In a final step, the inter-grating distance, i.e. ratio of *l* and *d*, is tuned until the remaining Moiré fringes are minimized, that is the case if Eqs. 2.53 and 2.55 are fulfilled as illustrated in Fig. 3.2c.

3.2 Software Package mammolib

To provide a convenient data processing and visualization especially for large field-of-view applications the mammolib-package was created. It contains functions for signal retrieval, stitching and correction of data in radiographic imaging mode. This section presents the tools necessary to obtain comprehensive absorption, differential phase and dark-field images of complete breast samples, whereas Chap. 4 focusses on advanced phase-retrieval methods. Using the mam_processing-routine the following steps are automatically executed:

- 1. At first, each projection is separately processed and the three image modalities are retrieved via Fourier analysis as described in Chap. 2 using the mam. FFT_analysis-function. Alternatively, a least square algorithm is available through the mam.LSQ_analysis-function, which minimizes the occurrence of fringes within the processed data at the expense of computing time.
- 2. The breast abladate is scanned in a zigzag manner, in order to avoid a readjustment of the sample holder and save scan time. Hence prior to stitching the initial projections are resorted executing the mam.resort_fields-function.
- 3. As a next step, the overlap of adjacent projections is determined. Therefore, a least square optimization algorithm is utilized, which shifts adjacent absorption images against each other until the overall discrepancy in intensity is minimized (mam.shift_best). This step is executed for all absorption projections and a respective mean value determined. Alternatively the overlap value can be manually tuned until the final stitched image yields interconnected tissue borders and features. Since the three image modalities are co-registered it is sufficient to determine the overlap for one data set only.
- 4. In order to retrieve comprehensive full-field mammograms, artefacts present within the initial projections have to be corrected. In the case of the absorption and dark-field images a ramp or polynomial background may superimpose the images, which arises from shadowing and beam-hardening effects [7]. While these artefacts can be corrected utilizing the mam.correction-function, knowledge on

the background or a flat image region such as air is required to enable a proper fitting of the latter. However, by implementing an breast-equivalent absorber during flat-field acquisition the generation of aforementioned artefacts associated with beam polychromaticity can be avoided, which renders a correction of absorption and dark-field data obsolete.

Nevertheless, in the case of the differential phase-contrast signal artefacts remain. With the purpose of saving scan time, only one flat-field is acquired prior to the sample scan, by which all projections are processed. Due to thermal instabilities (grating heat-up, change in hutch temperature) and mechanical vibrations, the fringe pattern is slightly drifting over time [8]. Hence by applying the flat-field to subsequent projections an offset in the differential phase-contrast channel is inherent as illustrated in Fig. 3.3a. This offset can be corrected for by comparing the cumulative sum of differential signal in the region of overlap of adjacent projections, as exemplarily shown in Fig. 3.3b. Since both images should contain the same data values, the difference between both is expected to be zero within the region of overlap. Thereby the constant offset value can be determined and then subsequently subtracted from one of the projections. The mam.correction_DPC-function performs this comparison first for each row then column-wise, whereas the first projection (top left) is considered as the initial value.

5. In order to enhance the visual appearance of the full-field mammograms, a stitching tool with blending operator was implemented, which is accessed by the mam.stitching_all_signals-function. Within the region of overlap, the input images are linearly weighted in both *x*- and *y*-direction and then summed by which a smooth transition between adjacent projections is achieved.

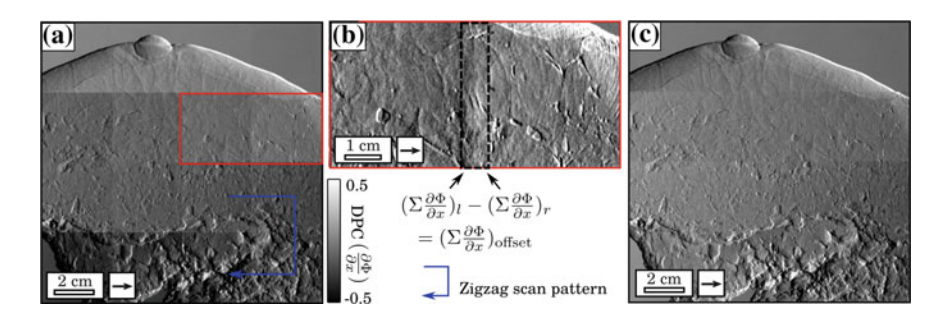


Fig. 3.3 Differential phase-contrast correction procedure. **a** Subsequently conducted, differential phase-contrast projections yield a growing offset, if processed with a single flat-field only. This is contingent on mechanical and thermal instabilities affecting the stability of the gratings, which to its end cause a drift of the Moiré fringes. **b** By comparing the cumulative sum of differential phase-contrast data of adjacent projections (*red framed*) within the region of overlap (*dashed black line*), the offset value per pixel can be determined. **c** Thereby each pair of projections is corrected each row-wise and then column-wise, by which full-field differential phase-contrast mammograms can be obtained. Note that **a**–**c** yield an identical color bar. *Arrows* indicate one-directional measurements

- 6. Finally, to account for "salt-and-pepper" noise as well as for hot and dead pixels a de-speckle routine is available through the mam.despeckle-option [9]. In a first step, the original image and a Gaussian blur of the latter are compared, by which noisy pixels are detected if they exceed a certain threshold within the difference image. In a second step, noisy pixels are selectively replaced by the corrected values, which are obtained from a 2D-median filtered version of the input image. Note that the despeckle-routine is preferred over directly applying a median-filter to the input image, since not decreasing the effective image resolution.
- 7. If desired, the differential data can be integrated to obtain absolute phase images. For a more detailed description of the steps #7-9 please find Chap. 4. Depending on the number of scan directions either an one- or a two-dimensional integration algorithm is available, which can be assessed via the mam.phase_integration_1D- and mam.phase_integration_2D-functions, respectively.
- 8. The retrieved phase images typically comprise low-frequency artefacts, especially in the case where boundary conditions are lacking, e.g. if the sample exceeds the field-of-view. By subtracting a Gaussian-filtered version of the image from the original these artefacts can be corrected for. Since this operation may also decrease the detectability of extended breast features it is favourable to use a selective, edge-preserving Gaussian (mam.filter_collection). Hereby an anisotropic diffusion algorithm is used to sufficiently blur important features while preserving the artefacts [10].
- 9. Finally, an unsharp masking filter can be applied to the images, in order to increase image acutance and enhance the depiction of high-frequency features, using the mam.unsharp_mask-function [11].

References

- 1. Di Maria, S., et al. (2014). Optimal photon energy comparison between digital breast tomosynthesis and mammography: a case study. *Physica Medica*, *30*, 482–488.
- 2. Siedband, M., Jennings, R., Eastgate, R., & Ergun, D. (1977). X-ray beam filtration for mammography. *Proceedings of SPIE*, 127, 204–207.
- 3. Gromann, L. (2014). Optimization of planar differential X-ray phase contrast imaging for mammography. Munich: Technische Universität München.
- 4. Cha, K., et al. (2012). Design and image-quality performance of high resolution CMOS-based X-ray imaging detectors for digital mammography. *Journal of Instrumentation*, 7, C04020.
- 5. Donath, T., et al. (2009). Inverse geometry for grating based X-ray phase-contrast imaging. *Journal of Applied Physics*, 106, 054703.
- Chabior, M. (2011). Contributions to the characterization of grating-based X-ray phasecontrast imaging. Dresden: Technische Universität Dresden.
- Chabior, M., et al. (2011). Beam hardening effects in grating-based x-ray phase-contrast imaging. Medical Physics, 38, 1189–1195.
- Tapfer, A., et al. (2012). Experimental results from a preclinical X-ray phase-contrast CT scanner. PNAS, 109, 15691–15696.
- 9. Jayaraman, S., Esakkirajan, S., & Veerakumar, T. (2009). *Digital image processing*. New Delhi: Tata McGraw Hill Education.

- 10. Perona, P., & Malik, J. (1990). Scale-space and edge detection using anisotropic diffusion. *IEEE Transactions on Pattern Analysis and Machine Intelligence*, 12, 629–639.
- 11. Polesel, A., Ramponi, G., & Mathews, V. (2000). Image enhancement via adaptive unsharp masking. *IEEE Transactions on Image Processing*, 9, 505–510.

Chapter 4 Bi-Directional Phase-Contrast Mammography

Every truth has two sides; it is as well to look at both, before we commit ourselves to either.

Aesop

Abstract In this chapter, the first bi-directional phase-contrast mammography measurements investigating fresh breast tissue are presented. First, disadvantages of a mono-directional scanning approach with respect to imaging sensitivity and usability of differential data are pointed out. By revealing both benign and malignant breast features, that exhibit highly anisotropic imaging contrast, we demonstrate the indispensable diagnostic necessity of a multi-directional scanning approach. Finally, this chapter is complemented by a section on bi-directional full-field mammography and a benchmark of one- versus two-dimensional phase retrieval techniques. Note that some of the results presented in the following have been earlier published as "Scherer, K. et al. Bi-directional X-ray phase-contrast mammography. *PLoS One* **9**, e93502 (2014)".

4.1 Introduction | Limitations of Mono-Directional Phase-Contrast Mammography

Despite the introduction of extensive screening programs in the 80's and a rapid promotion of mammography systems, breast cancer is still the second most common cause of cancer death for women worldwide [1]. The most prevailing difficulties of modern diagnostic mammography are a non-negligible number of false-positive diagnoses, accompanied by redundant medical follow-up (10.7%) and a relatively high rate of undetected tumors (21.9%), most prevalent in the examination of younger women [2]. Especially, dense breast soft-tissue exhibits only minor deviations with respect to attenuation characteristics, resulting in a poor imaging contrast for conventional mammography. Phase-sensitive X-ray imaging methods show the potential

to circumvent this problem by utilizing the intrinsically enhanced electron density contrast [3].

Initial mammography studies confirming diagnostic benefits of the superior softtissue contrast of phase-sensitive techniques were carried out with synchrotron radiation [4, 5]. The introduction of so-called Talbot-Lau interferometers in combination with a conventional laboratory X-ray source pushed phase-contrast imaging towards possible clinical applications [6]. In grating-based differential phase-contrast (DPC) imaging, phase-stepping enables the simultaneous retrieval of the differential phase, dark-field and conventional absorption signal [6–8]. The differential phase signal is obtained by measuring the angular deviations of the transmitted wavefront, which are directly linked to the local gradient of the tissue's phase-shift. Recent differential phase-contrast mammography studies conducted with freshly dissected complete breasts showed promising results with respect to clinical relevance and feasibility [9].

However, previous efforts also indicated that a direct translation of radiographic DPC towards conventional mammography is accompanied by two major drawbacks: first, the retrieved local phase gradient is of differential nature, which results in strongly edge-enhanced images with a reduced visual perception of extended structures, such as tumor masses and architectural distortions. One-dimensional integration of the differential data is possible, however requires the implementation of regularization algorithms in order to reduce streak artefacts in direction of the integration (accumulation of statistical errors) affecting the integrated phase [10, 11]. Second, since the gratings are only structured along one dimension, DPC imaging sensitivity is highly anisotropic, being non-zero only perpendicular to the grating lines. More precisely, only the component of electron density changes perpendicular to the grating lines can be accessed and contributes to the differential phase-contrast signal. Similarly, tissue-induced small-angle scatter, which determines the dark-field signal, remains undetected if emitted parallel to the grating bars [12]. Consequentially, the risk to overlook oriented, non-uniform structures within the breast such as ducts and tumor branches is high.

In this chapter, we apply a bi-directional imaging approach, composed of two orthogonal scans, to ensure orientation sensitivity while remaining in a radiographic acquisition mode [13–15]. We investigate the clinical relevance of this method by measuring an invasive ductal carcinoma (IDC) enclosed within the freshly dissected sample. By means of this medically significant tumor which comprises 72.8 % of all invasive breast cancer we subsequently prove the necessity of an isotropic detection sensitivity [16]. We evaluate the diagnostic advantages of two-dimensional integrated phase compared to absorption imaging and mono-directional phase retrieval. Furthermore, insights into the tumor morphology are obtained by analysing angular deviations in the scattering signal (directional dark-field imaging) [12, 17]. The conclusion of our study is ascertained by a histological verification of our findings.

4.2 Results 47

4.2 Results

4.2.1 Two-Dimensional Phase Retrieval

The imaging of the freshly dissected mastectomy specimen was performed in cranio-caudal orientation. For reasons of comparability and benchmarking, a digital mammogram (29 kVp, 120 mA, average glandular dose 1.22 mGy) of the specimen within the sample holder was conducted using a Selenia Dimensions scanner from Hologic as shown in Fig. 4.1a.

Firstly, to identify the tumorous region, one image of the complete breast was taken with the interferometer. A total field-of-view of $12.8 \times 12.8 \,\mathrm{cm}^2$ was realized by stitching 4×4 projections following the procedure explained in Chap. 3. Scans with 9 phase steps and an exposure time of 9 s per step (low-statistic) were performed with phase-stepping in x-direction. Hence, underlying imaging sensitivity was strongly anisotropic and only components of the signals in x-direction were detected. Only one flat-field, i.e. projection without the sample in the beam, was taken beforehand. A smooth stitching of the 16 projections was achieved by correcting drift-related offsets within the differential phase. This was done by levelling the overall DPC signal of adjacent projections within the region of joint overlap as described in Chap. 3. The processed and stitched images (Fig. 4.1) related to absorption (B), differential phase (C) and dark-field (D) were obtained by Fourier analysis [6].

On the basis of the complete DPC breast images (Fig. 4.1b–d), the position of the tumorous area was determined, by which two-directional differential phase-contrast mammography is showcased in the following: an isotropic DPC imaging sensitivity is realized by combining the two one-dimensional and mutually orthogonal measurements of the IDC with phase-stepping in x and y-direction, respectively. Two high statistic scans were performed with 13 phase steps and an integration time of 13 s per step each, in order to be able to exclude statistical error as the cause of the

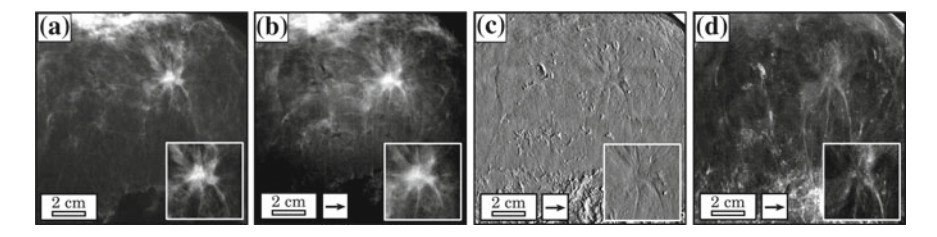


Fig. 4.1 Conventional and mono-directional phase-contrast mammograms of a breast specimen with invasive ductal carcinoma. Conventional, ex-vivo mammogram (**a**), grating-based absorption (**b**), differential phase (**c**) and dark-field mammogram (**d**) of the breast specimen. The field-of-view has a size of $12.8 \times 12.8 \, \mathrm{cm}^2$. Images **b-d** were obtained by stitching together 4×4 low-statistic projections. The high-statistic images of the invasive ductal carcinoma are shown as *inlays*. Arrows indicate one-directional measurements

presented results. The inlays in Fig. 4.1b–d show the corresponding images of the IDC acquired with phase-stepping in *x*-direction.

The thereto orthogonal scan in y-direction was performed by rotating the sample holder by 90° and then relocating the sample stage to image the same sample volume. For the purpose of demonstrating bi-directional phase-contrast mammography, latter was preferred over the rotation of all three gratings by 90° . Alignment and compression of the breast tissue remain unaltered within the sample holder during the measurement. In the following, images retrieved along one dimension are marked by a subscript "x" or "y", respectively.

Thereafter, the high-statistic set of absorption (A_x, A_y) , differential phase $(\partial \phi_x, \partial \phi_y)$ and dark-field images (D_x, D_y) of the IDC were fused. Firstly, it had to be ensured that the two images of each modality cover precisely the sample section. A possible displacement within the three image sets was reduced by using a least square optimization algorithm, which shifts the two absorption images against each other until the overall discrepancy in intensity between both images is minimized. This is feasible, since the detection of wave attenuation (absorption image) in comparison to wave deviations (differential phase, dark-field image), is independent from the scanning direction. The numerically determined shift (sub-pixel accuracy) was then used to correct for the displacement within the set of absorption, differential phase and dark-field images.

The fusion of the one-dimensional phase gradients $\partial \phi_x$ and $\partial \phi_y$ was realized via a two-dimensional Fourier transform approach [15]. The two-directional integrated absolute phase Φ^{2d} is then given by

$$\Phi^{2d}(x,y) = \mathcal{F}^{-1} \left[\frac{\mathcal{F}[\partial \phi_x(x,y) + i \partial \phi_y(x,y)](k,l)}{2\pi i (k+il)} \right] (x,y), \tag{4.1}$$

where \mathcal{F} is the two-dimensional Fourier transform, x,y the Cartesian and k,l the reciprocal space coordinates. The combined image $\partial \phi_x + i \partial \phi_y$ was mirrored horizontally and vertically to avoid edge discontinuities at the image boundaries, thus providing periodic data in Fourier space [18]. Since the phase integration corresponds to a f^{-1} -filter ($f = \sqrt{k^2 + l^2}$) in Fourier space, low frequencies are enhanced compared to high frequencies. The amplification of low frequencies generates a background, that is superimposed on the integrated phase image Φ^{2d} . The corrected phase image Φ^{2d} is obtained by

$$\Phi_c^{2d} = \Phi^{2d} - G(\Phi^{2d}, \sigma_1), \tag{4.2}$$

where $G(\Phi^{2d}, \sigma_1)$ is the integrated phase image Φ^{2d} , blurred with a Gaussian filter of width σ_1 . By intensively blurring (standard deviation of Gaussian kernel of $\sigma_1 = 80$, image size of 384 x 384 pixels) relevant image contents remain unaffected by the subtraction of the low frequency background.

The noise power spectrum of the input images $A_{x,y}$, $\partial \phi_{x,y}$ and $D_{x,y}$ is approximately inversely proportional to f [19]. Due to integration, the retrieved phase image exhibits a noise power spectrum proportional to f^{-2} . The low amplitude of

4.2 Results 49

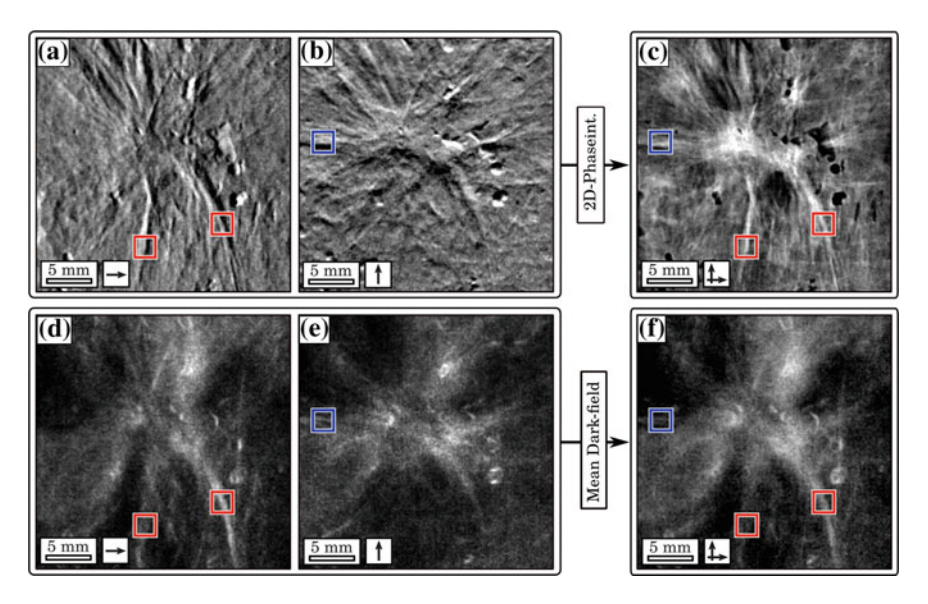


Fig. 4.2 *Imaging sensitivity of bi-directional phase-contrast mammography.* Two-directional differential phase $\partial \phi_x$ (**a**), $\partial \phi_y$ (**b**) and sharpened, two-dimensional integrated phase image Φ_s^{2d} (**c**). Two-directional dark-field D_x (**d**), D_y (**e**) and mean dark-field D_x image (**f**). *Arrows* indicate the direction of scanning. *Red* and *blue boxes* indicate tumor branches exclusively perceivable in the images obtained with scanning performed in x- or y-direction, respectively. Note that full detection sensitivity of malignant breast features is only provided in **c** and **f**

high-frequency noise in the image allows a high-frequency boost of Φ_c , in order to pronounce small tumor features and increase image acutance. The sharpened phase image Φ_s^{2d} (Fig. 4.2c) is obtained with an unsharp mask operation, given by

$$\Phi_s^{2d} = \Phi_c^{2d} + \alpha(\Phi_c^{2d} - G(\Phi_c^{2d}, \sigma_2)). \tag{4.3}$$

To pronounce very fine structures, a slight blur (standard deviation of Gaussian kernel of $\sigma_2 = 5$, image size of 384 x 384 pixels) was used. The filter strength was set to $\alpha = 3.2$. The dose-equivalent absorption image is calculated by

$$A(x, y) = e^{\frac{1}{2}(\ln A_x(x, y) + \ln A_y(x, y))}.$$
 (4.4)

To provide comparability to the sharpened phase image Φ_s^{2d} , the absorption image A was also processed with the unsharp mask filter ($\sigma_2 = 5$). However, in case of the absorption image A, the noise power spectrum is proportional to f^{-1} . This allows sharpening only to a minor extent ($\alpha = 0.5$), until the intrinsic amplification of high-frequency noise leads to a degradation of image quality [20]. The sharpened absorption image A_s is shown in Fig. 4.3b.

The mean dark-field image D (Fig. 4.2f), related to the overall small-angle scattering power of the sample, is given by

$$D(x, y) = e^{\frac{1}{2}(\ln D_x(x, y) + \ln D_y(x, y))}.$$
 (4.5)

Moreover, the dark-field images D_x and D_y were utilized to obtain information on the preferred scattering direction of the tissue under investigation. Scattering in x-direction (D_x) is coloured red, while scattering in y-direction (D_y) is coloured blue. The RGB-composition (Fig. 4.3d) of the two images classifies scattering power (brightness) and the preferred scattering direction, ranging from x-directed (red) over isotropic (purple) to y-directed (blue). Note that the latter has to be considered a pseudo "directional" dark-field image. In order to unambiguously distinguish isotropically scattering structures from ones who exhibit an anisotropic contrast, which is titled by 45° with respect to the imaging sensitivity, a tri-directional scan has to be conducted (for a detailed discussion cf. Jensen T. et al. (2010) [17]).

4.2.2 Imaging Sensitivity of Mono- Versus Bi-Directional Phase-Contrast Mammography

An overview of the high-statistic differential phase and dark-field images of the IDC, as obtained with the two-directional scanning approach, is given in Fig. 4.2. We investigate the dependency between the detection of strongly oriented tumor features and scanning direction, by comparing $\partial \phi_x$ against $\partial \phi_y$ and D_x against D_y , respectively: the tumor branches that are primarily vertically aligned (red framed) are strongly visible in $\partial \phi_x$ (Fig. 4.2a) and D_x (Fig. 4.2d). However, the same features cannot be detected in the thereto orthogonal images $\partial \phi_y$ (Fig. 4.2b) and D_y (Fig. 4.2e). By contrast the horizontally oriented tumor branch (blue framed), is exclusively detected in $\partial \phi_y$ (Fig. 4.2b) and D_y (Fig. 4.2e).

These observations indicate that tumor branches exhibit a strongly anisotropic contrast for both differential phase and dark-field imaging: within the tumor branches, electron density variations of the tissue are only minor, resulting in a poor differential phase contrast along the branch. However, compared to the surrounding, healthy tissue, the electron density is differing considerably. Furthermore, scatter caused by the branches and its substructures must be directed mostly perpendicular to the branch orientation.

Hence, the selection of scan direction, and therewith one-dimensional imaging sensitivity, determines to what extent the anisotropic tissue structures like branches, embedded in healthy tissue, can be detected. If scanning is performed parallel to the branch orientation for instance, neither scatter, caused by the branches, is detected, nor sufficient phase-contrast obtained. To secure a full detection of the tumor branches, an isotropic imaging sensitivity is indispensable, as provided by the combination of two orthogonally conducted scans. Comprehensive images, that provide the full range of features (red and blue frames), are obtained by fusing the one-directional differential phase and dark-field images as sharpened, two-directional

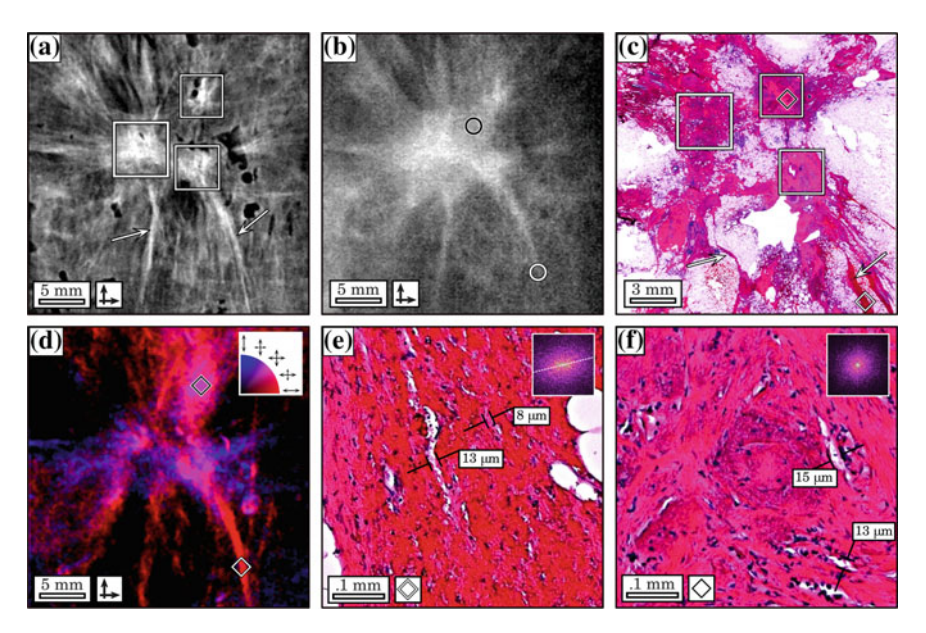


Fig. 4.3 Bi-directional phase-contrast and "directional" dark-field mammography of an invasive ductal carcinoma. a Sharpened, two-dimensional integrated phase image Φ_s^{2d} of the invasive ductal carcinoma. The frames in $\bf a$ and $\bf c$ indicate three locally separated tumor lesions (apparently trifocal). Arrows in $\bf a$ and $\bf c$ indicate fine tumor branches. b Sharpened, absorption image A_s of the invasive ductal carcinoma. Circles indicate position of relevant tumor details. c Histological slice (Hematoxylin and Eosin stain) of the invasive ductal carcinoma. d "Directional" dark-field image of the invasive ductal carcinoma. Preferred scattering direction is color-coded ranging from x-directed (red) over isotropic (purple) to y-directed (blue). c 200x magnified histological image of the tumor branch, as indicated by the white diamond in $\bf c$ and $\bf d$. The 2-dimensional FFT is shown as an inlay. d 200x magnified histological image of the tumor lesion, as indicated by the black diamond in $\bf c$ and $\bf d$. The 2-dimensional FFT is shown as an inlay

integrated phase Φ_s^{2d} (Fig. 4.2c) and mean dark-field D (Fig. 4.2f), respectively. Moreover, the sharpened, two-directional integrated phase image Φ_s^{2d} is free of streak and shadowing artefacts, even though the field-of-view is exceeded by the sample.

Besides overcoming the limited sensitivity of an one-directional scan, the two-directional approach exhibits further diagnostic advantages, illustrated in a benchmark (Φ_s^{2d} versus A_s) and "directional" dark-field case study (Fig. 4.3). The sharpened phase image Φ_s^{2d} (Fig. 4.3a) enables a diagnostic differentiation of the carcinoma into three locally separated tumor lesions (white frame). Two tumor branches are clearly perceivable, as directly emerging from the single lesions and spreading out to the image borders (arrows). The superior depiction of fine details within the phase image is caused by an enhanced soft-tissue contrast, but also improved local contrast and image acutance gained by image sharpening. By contrast, the same medical details can not be deduced from the dose-equivalent, sharpened absorption image A_s (Fig. 4.3b): the attenuation-based soft-tissue contrast is insufficient to enable a visual

distinction into lesions, but instead displays the tumor mass as pervasive structure (black circle). The tumor branches appear distinctively shortened, since fine branch parts (high-frequency features) are blurred within image noise (white circle). To validate the medical relevance of details exclusively perceivable within the phase image and exclude them as being image artefacts, histological evaluations were carried out. The tumorous area was extracted, dissected and stained with Hematoxylin and Eosin (Fig. 4.3c). We matched the three tumor lesions (white frame) and fine branches (arrows) with respect to size and orientation and confirmed their malignancy. Furthermore, the tumor was classified as apparently tri-focal, i.e. containing three locally separated lesions.

4.2.3 "Directional" Dark-Field Mammography

We extracted further diagnostic insights on the tumor constitution by examining two spots of the "directional" dark-field image (Fig. 4.3d) in more detail. The vertically oriented tumor branch (white diamond) scatters preferably perpendicular to its orientation, identifiable by the red color. This prominent anisotropic scatter can be ascribed to the tissue morphology on the scatter determining length scale, which is in the order of the analyser grating period of $p_2 = 4.8\,\mu\text{m}$ (cf. Fig. 2.6) [21]. The corresponding histological section of the branch was photographed with a magnification of 200 (Fig. 4.3e). The magnified image reveals multiple vascular walls (white) and elongated tumor cells (pink) preferably aligned alongside the fibre with diameters in the range of some microns. The elliptically-shaped two dimensional Fourier transform of the image (top right inlay) emphasizes the inherent alignment of the substructure. Since scatter occurs dominantly at edges/tissue-interfaces which are mutually oriented along the fibre, an unilaterally directed scatter is generated.

For a second correlation of the "directional" dark-field signal with tumor morphology, the top tumor lesion (black diamond) was chosen. Here, contributed scatter is uniformly distributed, discernible by the violet color. The corresponding histological section of the branch was also photographed with a magnification of 200 (Fig. 4.3f). The magnified image shows a cluster of tumor cells (violet) surrounded by bunches of elongated cells (pink) and vascular walls (white). By contrast, in this case the morphology seems random, without exhibiting any preferred orientation or distinct alignment of the inherent features. This impression is ascertained by the circular-shaped two-dimensional Fourier transform of the image (top right inlay). Accordingly, scatter in this area is isotropic.

4.2 Results 53

4.2.4 One- Versus Two-Directional Full-Field Phase-Contrast Retrieval

In a final step, bi-directional measurements were applied to a full-field DPC mammography of a fresh and cancer bearing mastectomy, with the goal of further investigating breast feature detection sensitivity and compare the here presented two-directional phase-retrieval technique to one-dimensional integration approaches. Figure 4.4A and B show the corresponding one-dimensional orthogonal differential phase gradients $\partial \phi_x$ and $\partial \phi_y$ obtained by following the acquisition protocol presented in Sect. 4.2.1. Note that for explanation purposes, the top row of $\partial \phi_x$ (Fig. 4.4a) was not corrected and therefore yields an offset as indicated by yellow arrows.

In accordance with the case study presented prior in this chapter (Fig. 4.2), also in this example multiple breast features with strongly anisotropic imaging contrast could be identified: the vertical aligned cyst border (red framed) is solely visible in $\partial \phi_x$ (Fig. 4.4a). In the thereto orthogonal scan $\partial \phi_y$ (Fig. 4.4b) the corresponding horizontal cyst encapsulation (blue frame - bottom) gets depicted while additional horizontally aligned tumor spiculations (blue frame - right), out-bonding the central tumor mass, are revealed. Following Eq. 4.1, full feature sensitivity showing the overall cyst encapsulation and tumor infiltration is given by deriving the two-directional, integrated phase image (Fig. 4.4c).

In order to visualize the above stated deficiencies of a mono-directional scanning and phase-retrieval approach, an ad-hoc integration of the local phase gradients was conducted, using

$$\Phi_x^{1d}(x,y) = \mathcal{F}^{-1} \left[\frac{\mathcal{F}[\partial \phi_x(x,y)](k,l)}{2\pi i k} \right] (x,y). \tag{4.6}$$

Figure 4.4d and e show the corresponding one-dimensional integrated absolute phase images Φ_x^{1d} and Φ_y^{1d} . Since phase retrieval accompanies an accumulation of statistical noise in direction of the integration path, severe streak artefacts are present in the image. As the differential data was stitched from multiple projections (with potentially varying offset), while parts of the breast were also exceeding the field-of-view, no well-defined background is available prior to integration; hence the integration constant remains unknown, which results in an additional row-specific offset value, as exemplarily indicated by yellow arrows in Fig. 4.4d. For reasons of comparison the one-dimensional integrated data sets Φ_x^{1d} and Φ_y^{1d} were fused to Φ^{1d} (Fig. 4.4f), adapting Eq. 4.4. Note that the obtained image fails at providing any diagnostic meaningful information, being corrupted by the superposition of orthogonal streak artefacts.

As a gold standard a refined, one-dimensional integration algorithm Φ^{1d*} using the Poisson solver and a smoothing operator was implemented (for a detailed derivation cf. Matias Di Martino, J. et al. (2013) [22]). Using $\frac{\partial^2}{\partial x^2}\Phi_x=\frac{\partial}{\partial x}\partial\phi_x$, whereas $\frac{\partial}{\partial x}\partial\phi_x$ corresponds to the first derivative of the phase gradient, Eq. 4.6 can be substituted to

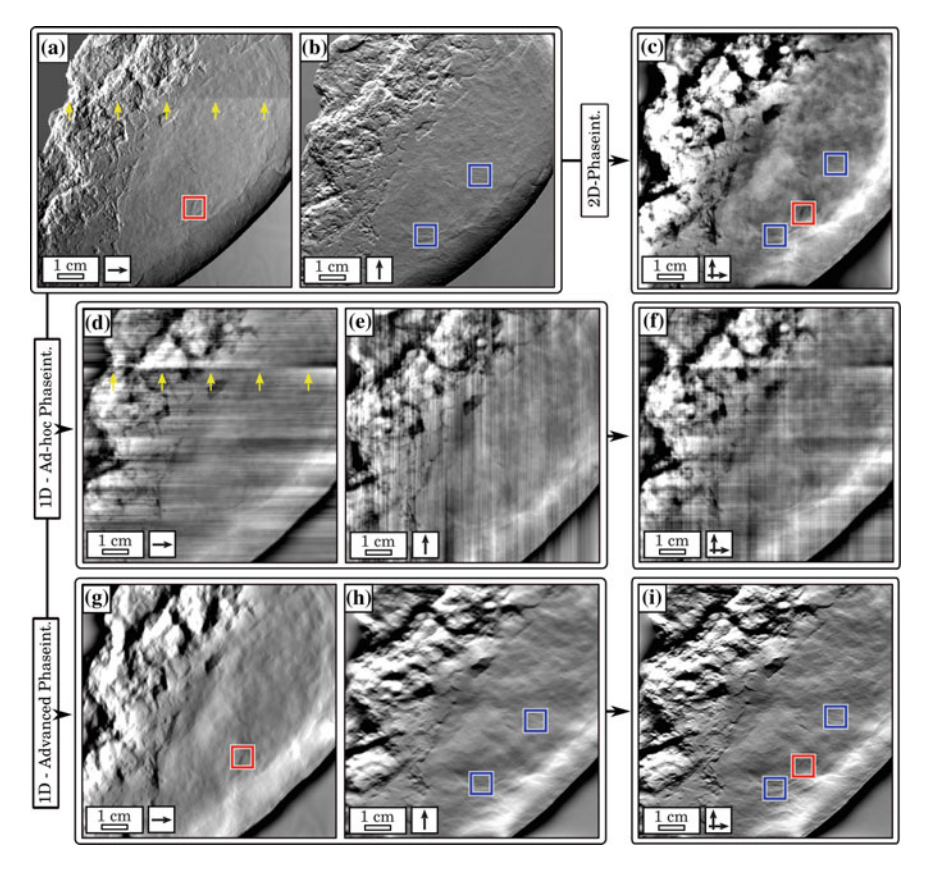


Fig. 4.4 Full-field mammography comparing one- versus two-directional phase retrieval. Two-directional differential phase $\partial \phi_x$ (a), $\partial \phi_y$ (b), and sharpened, two-dimensional integrated phase image Φ_x^{2d} (c). Ad-hoc one-dimensional integrated phase Φ_x^{1d} (d), Φ_y^{1d} (e) and corresponding fused phase image Φ^{1d} (f). Yellow arrows in a indicate uncorrected background within the differential data which accounts for severe integrations artefacts in d. Advanced one-dimensional integrated phase Φ_x^{1d*} (g), Φ_y^{1d*} (h) and corresponding fused, sharpened phase image Φ_s^{1d*} (i). Red and blue boxes indicate cyst borders and tumor infiltrations exclusively perceivable in scanning conducted in x- or y-direction, respectively. Note that Φ^{1d} is corrupted by severe streak artefacts while Φ_s^{1d*} appears blurred in comparison to Φ_s^{2d} . Arrows indicate one- and bi-directional measurements

$$\Phi_x^{1d}(x,y) = \mathcal{F}^{-1} \left[\frac{\mathcal{F}\left[\frac{\partial}{\partial x} \partial \phi_x(x,y)\right](k,l)}{-4\pi^2 k^2} \right] (x,y). \tag{4.7}$$

As stated in Sect. 4.2.1, the dominator of this equation can be considered a low-pass filter, which attenuates high-frequency contents of the integrated image. However, in the case of one-directional phase retrieval, this filter is restricted to one coordinate (k), hence high-frequency noise suppression is confined to the x-direction. Empirically, an artificial high-frequency noise-suppressor in y-direction can be incorporated, by

4.2 Results 55

modifying k^{-2} to $(k^2 + \lambda l^2)^{-1}$. Here λ determines the extent of smoothing applied in direction perpendicular to the phase gradient, namely the Fourier coordinate l. Finally, the phase, integrated in x- and smoothed in y-direction, is given by

$$\Phi_x^{1d*}(x,y) = \mathcal{F}^{-1} \left[\frac{\mathcal{F}\left[\frac{\partial}{\partial x} \partial \phi_x(x,y)\right](k,l)}{-4\pi^2 (k^2 + \lambda l^2)} \right] (x,y). \tag{4.8}$$

By setting $\lambda=0.7$, streak-artefact free phase images Φ_x^{1d*} (Fig. 4.4g) and Φ_y^{1d*} (Fig. 4.4h) of the breast specimen can be retrieved which are capable of depicting the feature content seen in the respective differential data. However, note that the smoothing operator does not only affect noise, but intrinsically also blurs high-frequency image details perpendicular to the integration direction. This is of special importance considering that the sharpened, fused phase image Φ_s^{1d*} (Fig. 4.4i) consequently comprises blurring of breast features in both directions. This drawback manifests itself in an overall blurred image and reduced spatial resolution, when compared to the corresponding sharpened, two-dimensional integrated phase image Φ_s^{2d} (Fig. 4.4c). Finally, note that various other phase-retrieval approaches exist, which aim at the reduction of image artefacts while maintaining image acutance, among others total-variation regularized based algorithms [23].

4.3 Discussion | Diagnostic Sensitivity Requires Bi-Directional Phase-Contrast Mammography

In this chapter, we demonstrated that grating-based mammography faces the problem of a diagnostically limited imaging sensitivity, if operated with a mono-directional scan alone. We identified both benign (cyst) and malignant breast structures (IDC), that exhibit a strongly anisotropic imaging contrast for both differential phase and dark-field imaging. To provide diagnostic reliability and ensure detection of oriented, tumorous structures, regardless their orientation within the breast, an isotropic imaging sensitivity is indispensable and could be provided by applying a two-directional scanning approach. An isotropic imaging sensitivity is a crucial requirement for the successful detection of early stage tumors such as in-situ carcinoma. Here, tumor growth is naturally limited to the inner compartments of ducts, resulting in a elongated tumor shape similar to the observed IDC branches [24, 25].

We have proven the feasibility of the two-directional scanning and phase-integration approach by first localizing the tumor and then subsequently measuring the corresponding enclosed section within the mastectomy specimen. We suggest that this technique is also clinical compatible, since we could successfully apply it to full-field mammography in a second step.

To exclude statistical errors as cause of the observed anisotropic imaging contrast given by IDC branches, this proof-of-principle study had to be conducted with high-statistic measurements and thus should neither be considered dose nor time

relevantly designed. Stampanoni, M. et al. and Sztrókay, A. et al. already discussed that an acquisition of images within the dose limits required for clinical applications would be possible by optimizing several setup relevant aspects such as design energy, X-ray target material, beam filtration, grating quality, duty-cycle, grating substrate thickness, sample holder and detector efficiency [9, 26]. For dose-compatible phase-contrast mammography see Chap. 7.

Keypoints

- Both benign and malignant breast features can exhibit strongly anisotropic imaging contrast in phase-contrast mammography.
- Diagnostically meaningful sensitivity requires an atleast bi-directional scanning approach.
- Two-dimensional phase retrieval provides superior image quality in comparison to one-dimensional techniques.

We elaborated additional diagnostic advantages accompanied by the two-directional scanning approach which could further motivate the need to acquire two images: the two-dimensional integration mechanism provides absolute, streak-artefact free phase images which proved to facilitate the visual differentiation of medically significant tumor details, yet unseen in the dose equivalent absorption image. The excellent depiction of high-frequency features yields the potential to strongly promote the detection of early stage tumors, fine tumor branches and small metastases. Finally, we showed that advanced one-dimensional phase integration approaches can also generate streak-artefact free, absolute phase images. These however comprise a reduced effective image resolution, hence limited detection quality of fine breast features, in comparison to the two-directional phase integration approach.

Furthermore, we examined a possible diagnostic application of "directional" dark-field imaging by characterizing the soft-tissue morphology on the micrometer length scale, far below the actual detector resolution. The morphology of two tumor associated areas could be characterized by their scattering behaviour as randomly proliferated and inherently oriented, respectively. This technique may promote the characterization and therewith diagnostic classification of suspicious structures and microcalcifications as linear branching or coarse granular [27, 28]. Besides, it might give a hint concerning the neoplastic grading of tumorous tissue by distinguishing between well-differentiated/oriented and fully anaplastic cell domains. Finally, the 90° rotation of the three gratings could be circumvented by the implementation of two-dimensionally structured gratings [13].

4.4 Materials and Methods

4.4.1 Imaging Dose

The applied radiation dose was measured using the incident air kerma with a Dosimax plus/RQX-detector system. The incident air kerma rate was found to be 2.1 mGy at the beam center. For the initial low-statistic projections, 9 phase steps with an integration-time of 9 s each were taken. In case of the high-statistic projections used for the two-directional proof-of-principle study the number of steps and integration-time was increased to 13. To calculate the mean glandular dose a Monte-Carlo based conversion factor of 0.389 was chosen, determined by the half-value layer (Al) of 0.8 mm and a sample thickness of 5 cm [29]. A mean glandular dose of 66 mGy (total exposure time of 81 s, low-statistic) and 138 mGy (total exposure time of 169 s, high-statistic) per projection was found.

References

- 1. Siegel, R., Naishadham, D., & Jemal, A. (2012). Cancer statistics, 2012. *CA: A Cancer Journal for Clinicians*, 62, 10–29.
- 2. Poplack, S., Tosteson, A., Grove, M., Wells, W., & Carney, P. (2000). Mammography in 53,803 women from the new Hampshire mammography network. *Radiology*, 217, 832–840.
- 3. Keyriläinen, J., et al. (2010). Phase-contrast X-ray imaging of breast. *Acta Oncologica*, 51, 866–884.
- 4. Takeda, T., Momose, A., Ueno, E., & Itai, Y. (1998). Phase-contrast X-ray CT image of breast tumor. *Journal of Synchrotron Radiation*, 5, 1133–1135.
- 5. Arfelli, F., et al. (2000). Mammography with synchrotron radiation: Phase-detection techniques. *Radiology*, 215, 286–293.
- 6. Pfeiffer, F., Weitkamp, T., Bunk, O., & David, C. (2006). Phase retrieval and differential phase-contrast imaging with low-brilliance X-ray sources. *Nature Physics*, 2, 258–261.
- Momose, A., et al. (2003). Demonstration of X-ray talbot interferometry. *Japanese Journal of Applied Physics*, 42, 866–868.
- 8. Pfeiffer, F., et al. (2008). Hard-X-ray dark-field imaging using a grating interferometer. *Nature Materials*, 7, 134–137.
- 9. Stampanoni, M., et al. (2011). The first analysis and clinical evaluation of native breast tissue using differential phase-contrast mammography. *Investigative Radiology*, 46, 801–806.
- Roessl, E., et al. (2012). Image fusion algorithm for differential phase contrast imaging. Proceedings of SPIE, 8313, 54.
- 11. Thuering, T., Modregger, P., Pinzer, B., Wang, Z., & Stampanoni, M. (2011). Non-linear regularized phase retrieval for unidirectional X-ray differential phase contrast radiography. *Optics Express*, 19, 25545–25558.
- Jensen, T., et al. (2010). Directional X-ray dark-field imaging. *Physics in Medicine and Biology*, 55, 3317.
- 13. Zanette, I., Weitkamp, T., Donath, T., Rutishauser, S., & David, C. (2010). Two-dimensional X-ray grating interferometer. *Physical Review Letters*, *105*, 248102.
- 14. Wen, H., Bennett, E., Hegedus, M., & Rapacchi, S. (2009). Fourier X-ray scattering radiography yields bone structural information. *Radiology*, 251, 910–918.
- Kottler, C., David, C., Pfeiffer, F., & Bunk, O. (2007). A two-directional approach for gratingbased differential phase contrast-imaging using hard X-rays. Optics Express, 15, 1175–1181.

- Li, C., Anderson, B., Daling, J., & Moe, R. (2003). Trends in incidence rates of invasive lobular and ductal breast carcinoma. *JAMA*, 289, 1421–1424.
- 17. Jensen, T., et al. (2010). Directional X-ray dark-field imaging of strongly ordered systems. *Physical Review B*, 82, 214103.
- 18. Arnison, M., Larkin, K., Sheppard, C., Smith, N., & Cogswell, C. (2004). Linear phase imaging using differential interference contrast microscopy. *Journal of Microscopy*, 214, 7–12.
- 19. Cha, B., et al. (2012). Design and image-quality performance of high resolution CMOS-based X-ray imaging detectors for digital mammography. *Journal of Instrumentation*, 7, C04020.
- Polesel, A., Ramponi, G., & Mathews, V. (2000). Image enhancement via adaptive unsharp masking. IEEE Transactions on Image Processing, 9, 505–510.
- 21. Malecki, A., Potdevin, G., & Pfeiffer, F. (2012). Quantitative wave-optical numerical analysis of the dark-field signal in grating-based X-ray interferometry. *Europhysics Letters*, 99, 48001.
- 22. Matias Di Martino, J., et al. (2013). Phase retrieval from one partial derivative. *Optics Letters*, 38, 4813–4816.
- 23. Sperl, J., et al. (2014). A Fourier-domain algorithm for total-variation regularized phase retrieval in differential X-ray phase contrast imaging. *Optics Express*, 22, 450–462.
- 24. Barreau, B. (2005). Mammography of ductal carcinoma in situ of the breast: Review of 909 cases with radiographic-pathologic correlations. *European Journal of Radiology*, 54, 55–61.
- Menell, J., et al. (2005). Determination of the presence and extent of pure ductal carcinoma in situ by mammography and magnetic resonance imaging. *The Breast Journal*, 11, 380–390.
- Sztrókay-Gaul, A., et al. (2012). High-resolution breast tomography at high energy: a feasibility study of phase contrast imaging on a whole breast. *Physics in Medicine and Biology*, 57, 2931– 2942.
- Dinkel, H., Gassel, A., & Tschammler, A. (2000). Is the appearance of microcalcifications on mammography useful in predicting histological grade of malignancy in ductal cancer in situ? *The British Journal of Radiology*, 73, 938–944.
- Stomper, P., & Connolly, J. (1992). Ductal carcinoma in situ of the breast: correlation between mammographic calcification and tumor subtype. *American Journal of Roentgenology*, 159, 483–485.
- 29. Dance, D., Skinner, C., Young, K., Beckett, J., & Kotre, C. (2000). Additional factors for the estimation of mean glandular breast dose using the UK mammography dosimetry protocol. *Physics in Medicine and Biology*, 45, 3225.

Chapter 5 Screening Value of Phase-Contrast Mammography

Um klar zu sehen, genügt oft ein Wechsel der Blickrichtung.

Antoine de Saint-Exupery

Abstract In this chapter, the diagnostic potential of phase-contrast and dark-field mammography as a future screening modality is exemplarily illustrated by means of a selective case study. First, limitations of clinical imaging techniques, such as an inherently low soft-tissue absorption contrast in the female breast, are pointed out on an incentive manner. Afterwards four diagnostically interesting cases, containing bi- and multifocal breast cancer, are presented to the reader and extensively discussed. The aim of this chapter is to motivate and justify the further progression of phase-contrast mammography towards first clinical trails and multi-reader studies. Note that some of the results presented in this chapter are based on the publication "Grandl, S., Scherer, K. et al. Improved visualization of breast cancer features in multifocal carcinoma using phase-contrast and dark-field mammography – an ex-vivo study. *Eur. Radiol.* **25**, 3659–68 (2015)".

5.1 Introduction | Current Shortcomings of Clinical Screening

With the implementation of nation-wide screening programs in many countries breast cancer mortality has steadily declined over the past decades [1]. Technical developments in conventional breast imaging such as tomosynthesis have led to a significantly improved detection of early breast cancer and pre-invasive breast lesions. However, breast cancer remains one of the leading causes of cancer death in women world-wide and underlying imaging techniques continue to have major limitations in daily clinical routine [2].

While being the standard screening technique, the diagnostic sensitivity and specificity of conventional mammography remains fairly low, contingent on the fact that attenuation-based contrast is inherently low within breast soft-tissue. This is of particular disadvantage in the case of women with dense breast tissue [3] (cf. Fig. 2.9b)

and women at high familial risk for breast cancer [4, 5]. While mammography performs with a sensitivity of 76 % in breasts with entirely fatty pattern, it is only 60 % in the case of breasts with fibroglandular or dense pattern [6, 7]. For young women at high familial risk for breast cancer up to two-thirds of breast cancers are diagnosed as interval cancers in between subsequent screening rounds, where cancer has already been growing large and positive axillary lymph node metastases are exhibited. Besides, concerns arise with respect to an intolerable lifetime radiation exposure for young patients.

Especially in this high-risk group and for the detection of multifocal or multicentric breast cancer, specialist recommend MRI as an initial screening modality. In addition to offering the highest diagnostic sensitivity in both fatty (80%) and fibroglandular tissue (81%) MRI avoids ionizing radiation [7]. On the other hand it suffers from a low spatial resolution, being very cost- (1025\$ for bilateral contrast-enhanced breast MRI versus 85\$ for bilateral mammography per examination) and time-intensive (30–60 min overall examination time for MRI versus 10–20 min overall examination time for screening mammography). Further the use of intravenous contrast agents is required [7]. Here, adverse reactions have been reported of up to 0.1% of all patients who have been given intravenous gadolinium contrast agents [8]. Besides, MRI is non-sensitive towards tiny calcium deposits, which can be indicative for malignancy. Finally, MRI is less specific than screening mammography comprising the risk of increasing overdiagnosis, invasive follow-up procedures and potential overtreatment in clinical routine, which is currently under debate [9].

Ultrasound is helpful for the diagnostic evaluation of palpable or mammographically identified tumor masses, but is considered as an supplemental screening modality only. This becomes particularly obvious in a study by Berg, W. et al., who demonstrated that ultrasound alone is rather unspecific and would substantially increase the false positive rate by 8.1 % [10]. Being both operator-dependent and time-consuming, ultrasound as well as MRI are unsuitable for a broad implementation into standard population screening [11].

In the case of X-ray energies used in clinical mammography, phase-contrast (PC) and dark-field radiography (DF) are suitable candidates for complementing conventional screening. These image modalities yield the potential to overcome the relatively low absorption-contrast of low Z materials in dense breast tissue, since PC relies on the intrinsically enhanced electron-density contrast and DF is based on the smallangle scattering capability. The advantage of phase-sensitive imaging gets obvious, when comparing the β and δ values of fatty and glandular tissue, at an energy of 27 keV. While the difference in β , exhibited between glandular and adipose tissue, accounts to only 0.25×10^{-10} , it is approximately three orders of magnitude higher in the case of δ , namely 0.20×10^{-7} [12]. Initial phase-sensitive breast imaging which could verify an increased detection sensitivity at reduced radiation dose, was conducted with free space propagation and analyzer-based imaging techniques at synchrotron facilities [13–15]. Besides providing a scatter-sensitive imaging channel, dark-field mammography benefits from sub-resolution sensitivity [16], which enables the detection of microstructures within the breast that are smaller than the pixel pitch of the detector [17, 18].

Patient	Histological diagnosis	ACR	BIRADS	Max Tumor diameter (mm)
I	Multifocal invasive carcinoma not specific type (NST, formerly invasive ductal), G1	2	IV	40
II	Trifocal invasive carcinoma not specific type (NST, formerly invasive ductal) and invasive lobular carcinoma, G 1–2	2	IV	15
III	Bifocal carcinoma not specific type (NST, formerly invasive ductal) G2	2	V	25
IV	Invasive carcinoma not specific type (NST, formerly invasive ductal), G 2	3	V	40

Table 5.1 Tumor characteristics of patient I–IV

Histological diagnosis and tumor type; Classification of mammographic breast density according to the American College of Radiology (ACR); preoperative imaging according to the breast imaging reporting and data system (BIRADS); maximum tumor size according to histopathology. Please note that the smallest sample diameter is measured in anteroposterior direction and does not correspond to the maximum craniocaudal diameter used for the experimental mammography

With the recent introduction of a grating-based imaging approach utilizing a Talbot-Lau interferometer, retrieval of phase-contrast and dark-field signal is no longer restricted to highly brilliant X-ray sources, but is now compatible with clinical X-ray sources [19, 20]. First studies investigating mastectomy samples with laboratory-based phase-contrast mammography showed promising results with respect to diagnostic potential by means of improved tumor visualization [21], image quality [22] and enhanced detection of ultra-small microcalcifications [17, 18].

The results shown in this chapter demonstrate that dark-field imaging alone results in improved visualization of tumor-infiltrated soft-tissue strands, multifocality, tumor boundaries and small calcified tumor clusters yet undifferentiated with conventional imaging techniques. By means of four selective case studies (for more details cf. Table 5.1), diagnostic merit of phase-contrast mammography is verified and suggested as a potential future screening modality.

5.2 Results

5.2.1 Case I | Dark-Field Mammography Reveals Radiographically Undetectable Tumor Nodules

Patient I presented with a histologically proven recurrent breast carcinoma of the contralateral left breast after breast conserving therapy (data not shown). Additionally, two nodular indurations of the right breast in the upper lateral quadrant were clinically suspicious. Conventional in-vivo mammography (IV-Mx) of the right breast

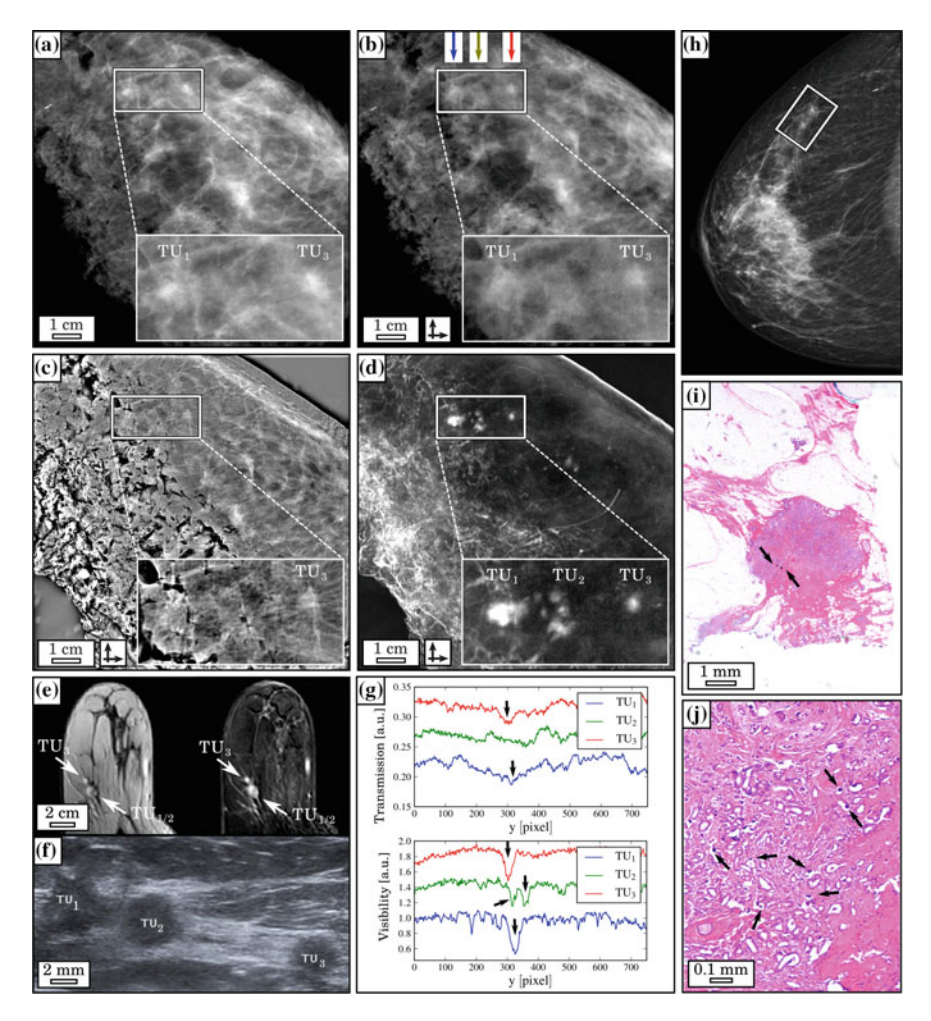


Fig. 5.1 Dark-field mammography reveals radiographically undetectable tumor nodules. Clinical ex-vivo mammography (EV-Mx, **a**), experimental absorption-contrast mammography (A-Mx, **b**), phase-contrast mammography (**c**) and dark-field mammography (DF-Mx, **d**) of patient I; representative section from the in-vivo MRI (**e**) including contrast-enhanced T1 weighted sequence (**e**—*left*) and the corresponding subtraction image (**e**—*right*) and ultrasonography (**f**); *vertical line* plots quantifying superior depiction of tumor (TU) 1, 2 and 3 in DF-Mx (G—*bottom*) in comparison with A-Mx (**g**—*top*); in-vivo mammography (IV-Mx) of patient I in craniocaudal projection (**h**); exemplary histological image (hematoxylin-eosin staining) of one calcified tumor nodule (**i** and **j**), *arrows* indicating hyper-fine microcalcifications. The *rectangles* in **a**—**d** and **h** indicate TU₁₋₃. The *crossed arrows* in **b**—**d** indicate bi-directional measurements

revealed two corresponding adjacent lesions (Fig. 5.1h, white box) measuring 5 and 2 mm in the right upper lateral quadrant. Ultrasound revealed altogether seven suspicious lesions of 3–8 mm diameter in the upper lateral right quadrant three of which

5.2 Results 63

are shown in Fig. 5.1f. Dynamic MRI showed two suspicious enhancing lesions in the upper lateral quadrant of the right breast corresponding to the in-vivo mammography (Fig. 5.1e). Histopathology of the whole breast revealed a multifocal carcinoma not specific type (NST, formerly invasive ductal carcinoma) grade 1 with the single tumor nodules measuring up to 6 mm and a maximum total diameter of 4 cm within an extensively growing ductal carcinoma in situ (6 cm).

Figure 5.1a-d show ex-vivo clinical mammography (EV-Mx), experimental absorption-contrast mammography (A-Mx), phase-contrast mammography (PC-Mx) and dark-field mammography (DF-Mx) of the breast specimen I in craniocaudal orientation, which support the mammographic finding of two separated tumor nodules (TU₁ and TU₃), although being partially superimposed by surrounding breast parenchyma and resection margins. Surprisingly, in the DF-Mx five additional smaller spots of high scattering contrast, composing a third nodule (TU₂), were detected between the mammographically verified nodules TU₁ and TU₃. The spatial arrangement of the additional strongly scattering nodules within the DF image is consistent with the corresponding ultrasound section, showing a hypoechogenic bridge connecting the very lateral TU₁ and TU₂ as well as the third nodule TU₃. The detection of an additional, intermediate nodule may explain why the first nodule TU₁ is presented distinctively enlarged within the MRI in comparison to TU₃: the low spatial resolution of MRI in combination with a continuous perfusion of contrast agent within TU₁ and TU₂ seems to depict the latter falsely as one persuasive tumor mass. Histopathological work-up (Fig. 5.1i, j) proved the nodules with high DF-contrast as small calcified tumor nodules of 6 mm maximum diameter.

Since the overall volume of microcalcified tissue is small, linear absorption coefficient (EV-Mx, A-Mx) and electron density (PC-Mx) of the tumorous tissue are hardly altered by the presence of calcium, which leads to a visual blurring of the tumor within the surrounding breast parenchyma. However, imaging sensitivity in DF-Mx is enhanced towards ultra-small calcifications in the size of some microns accounting for the strong scattering signal provided by microcalcified structures within the tumor nodules. The surrounding breast parenchyma does not contribute to the scattering signal, which enables a clear differentiation of the small calcified tumor nodules from the surrounding breast tissue. Vertical Line plots in A-Mx (Fig. 5.1g—top) and DF-Mx (Fig. 5.1g—bottom) visualize the superior depiction of all tumor nodules by means of DF-Mx. To quantify this observation the contrast-to-noise ratio (CNR) was calculated for each tumor by

$$CNR = \frac{|S_t - S_s|}{\sigma_s},\tag{5.1}$$

where $|S_t - S_s|$ corresponds to the difference between the signal intensities of the tumor (t) and respective surrounding tissue (t), divided by the standard deviation of the pure image noise σ_s , preferably calculated from a flat section within the surrounding tissue. Values of 14.28 (TU₁), 4.82 (TU₂) and 7.76 (TU₃) in the DF-Mx by far exceed those in the A-Mx of 3.58 (TU₁), 1.71 (TU₂) and 4.14 (TU₃). In the presented case, DF-Mx was the only radiographic imaging modality depicting and

detecting additional tumor nodules correctly, yet undetectable or spatially unresolved within conventional mammography and MRI.

5.2.2 Case II | Dark-Field Mammography Reveals Pervasion of the Breast with Partially Tumorous Soft-Tissue Strands

Patient II presented with a palpable mass in the upper lateral quadrant of the left breast. The IV-Mx (Fig. 5.2e) showed a mass lesion of 7 mm diameter in the upper lateral quadrant of the left breast associated with a suspicious architectural distortion. Ultrasonography showed a corresponding suspicious architectural distortion measuring $14 \times 12 \times 8$ mm³ with typical posterior acoustic shadowing. Histopathology of the whole abladate revealed a trifocal carcinoma with the single tumors lying directly adjacent to each other including an intermediate grade (G 2) invasive ductal carcinoma and an intermediate to low grade (G 2-3) invasive lobular carcinoma.

Figure 5.2a–d show EV-Mx, A-Mx, PC-Mx and DF-Mx of breast abladate II. Histological images in hematoxylin-eosin staining show parts of the tumor-infiltrated tissue strands originating from the main tumor (Fig. 5.2f, g). Spiculated soft-tissue strands originating from the tumor and perfusing the surrounding tissue within a distance of approximately 2 cm were detected in all image modalities. However, in the DF-Mx (and to some extend in PC-Mx), the extension of the strands was distinctively vaster than suggested by the other image modalities reaching even up to the posterior resection margin (inlays in Fig. 5.2d). Histology revealed that the tissue strands consist of vessels and are partially infiltrated by tumor cells.

The poor differentiability of the spiculated strands in IV-Mx, EV-Mx, A-Mx and PC-Mx within the surrounding tissue can mainly be attributed to the small diameter (1–1.5 mm) of the strands in comparison to the underlying breast tissue (5 cm) in beam direction as well as the fact that the differences in electron density between the tissue strands and the surrounding fatty breast tissue are relatively low. Hence the effective change in linear absorption coefficient (EV-Mx, A-Mx) and electron density (PC-Mx) induced by the tissue strands with respect to the embedding tissue is minor, resulting in a poor contrast which is insufficient for proper delineation of the tissue strands from the surrounding tissue (CNR = 0.86). However, the scattering properties within the strands strongly differ from the surrounding tissue. By means of DF-Mx, a clear differentiation (CNR = 3.98) from the surrounding tissue was achieved, since scatter caused by the vessels and highly cellular structures within strands is not limited by their thickness. Although the micromorphology of the strands remains spatially unresolved, sub-resolution sensitivity towards the inherent structures is provided by the dark-field signal. Thus, the small-angle scattering signal caused by vascular walls and structures with high cellularity is detected by DF-Mx. Since inherent structures are mostly aligned alongside the strands, scatter is highly isotropic resulting in an add-up of signal. Additionally, DF-Mx provides a flat

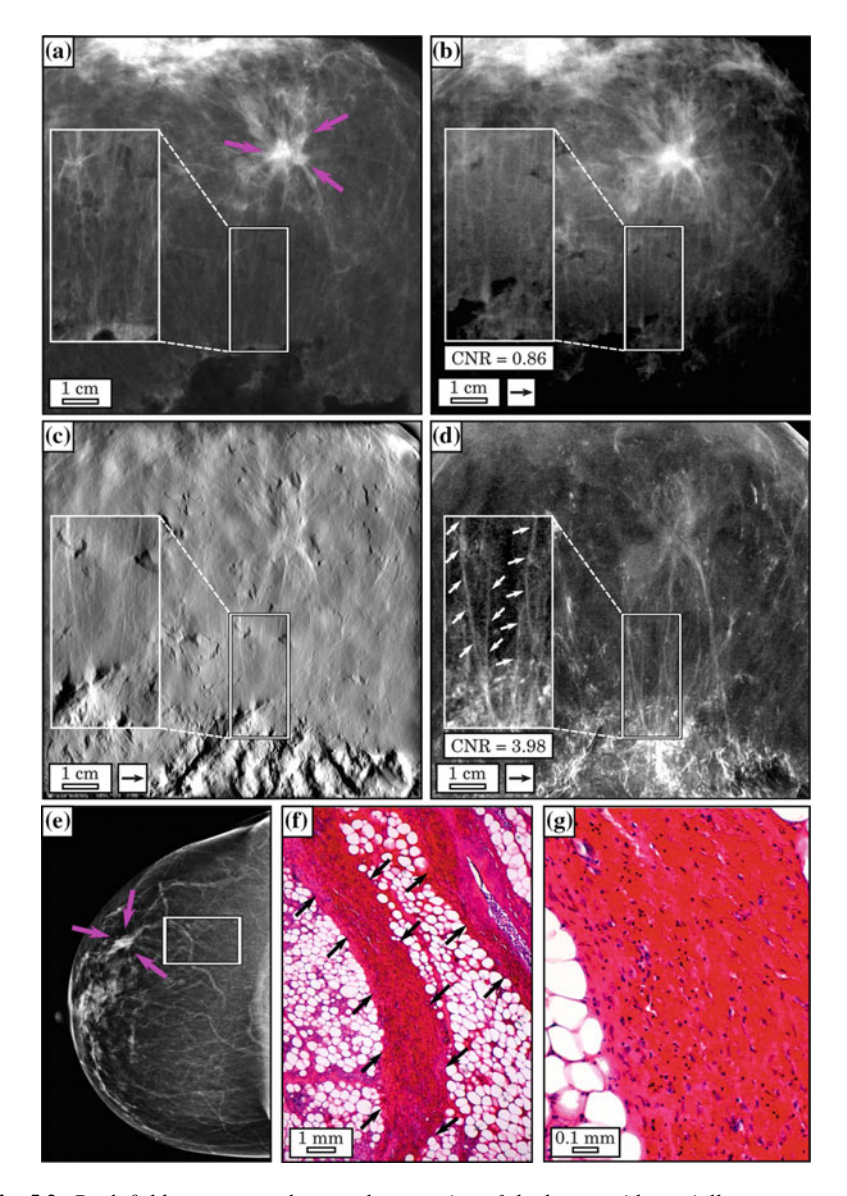


Fig. 5.2 Dark-field mammography reveals pervasion of the breast with partially tumorous softtissue strands. Clinical ex-vivo mammography (a), experimental absorption-contrast mammography (b), phase-contrast mammography (c) and dark-field mammography (d); in-vivo mammography (e) of patient II in craniocaudal projection; pink arrows in a and e indicate the trifocal carcinoma; white rectangles in a-e indicate partially infiltrated tissue strands emerging from the tumor; exemplary histological image (hematoxylin-eosin staining) of partially tumor-infiltrated tissue strands (f) and (g) as indicated by black arrows. The arrow in b-d indicate one-directional measurements

background as fatty tissue is hardly scattering. This facilitates the depiction of the fine tumor strands from the surrounding tissue, yet undetectable in conventional imaging. With the information obtained by DF-Mx available in the preoperative mammogram of this patient, an additional preoperative MRI would likely have been recommended for clarifying the tumor extent with respect to pectoral muscle infiltration.

5.2.3 Case III | Phase-Contrast Mammography Reveals Tumor Margins with Special Cellular Characteristics

Patient III presented with a palpable mass in the upper lateral quadrant of the left breast. Palpation revealed two suspicious indurations: in the left upper lateral and in the left lower medial quadrant. IV-Mx (Fig. 5.3e) revealed a suspicious mass (tumor 1), measuring $14 \times 9 \, \text{mm}^2$ in the left lower medial quadrant which was mainly superimposed by breast parenchyma. A second mass of $12 \times 8 \, \text{mm}^2$ was found in the left upper lateral quadrant (tumor 2). Sonographically (Fig. 5.3f shows tumor 1), both tumors had typical malignant features such as poor echogenicity, blurred margins and a hyperechogenic rim. Histopathology revealed tumor 1 (Fig. 5.3g) as a $2.5 \times 1.2 \times 1 \, \text{cm}^3$ moderately differentiated (G 2) invasive carcinoma of not specific type (NST), tumor 2 as a partially hemorrhagic, $2.5 \times 2.3 \times 2 \, \text{cm}^3$ moderately differentiated (G 2) invasive carcinoma NST containing a postbioptic hemorrhagic cavity.

Figure 5.3a–d show EV-Mx, A-Mx, PC- and DF-Mx of sample III. Note, that the air inclusions represent a tissue defect at the biopsy site in tumor 2. Both tumor manifestations are detectable within the dissected breast in all modalities. In the PC- and DF-Mx, an additional strong, linear contrast was observed exclusively at the dorsal margin of tumor 1 (black arrows in Fig. 5.3c, d), enabling a clear differentiation from the adjacent breast tissue. Histopathological work-up revealed a desmoplastic stromal reaction and fibrous changes alongside the edge of the tumor resulting in a sharp demarcation from the surrounding tissue (black arrows in Fig. 5.3g).

The distinct separation of tissue is accompanied by a strong local variation in refractive index across tumor and adherent parenchyma, which generates a high contrast within the phase signal. Further X-rays are scattered at the tissue border alongside the tumor margin as visible within the dark-field image signal. Finally, the dark-field signal may additionally be sensitive to changes in tissue cellularity induced by the desmoplastic stromal reaction. In contrast, absorption-based imaging (IV-Mx, EV-Mx and A-Mx) is hardly sensitive towards this specific tumor entity and displays posterior and anterior tumor margins in a very similar manner.

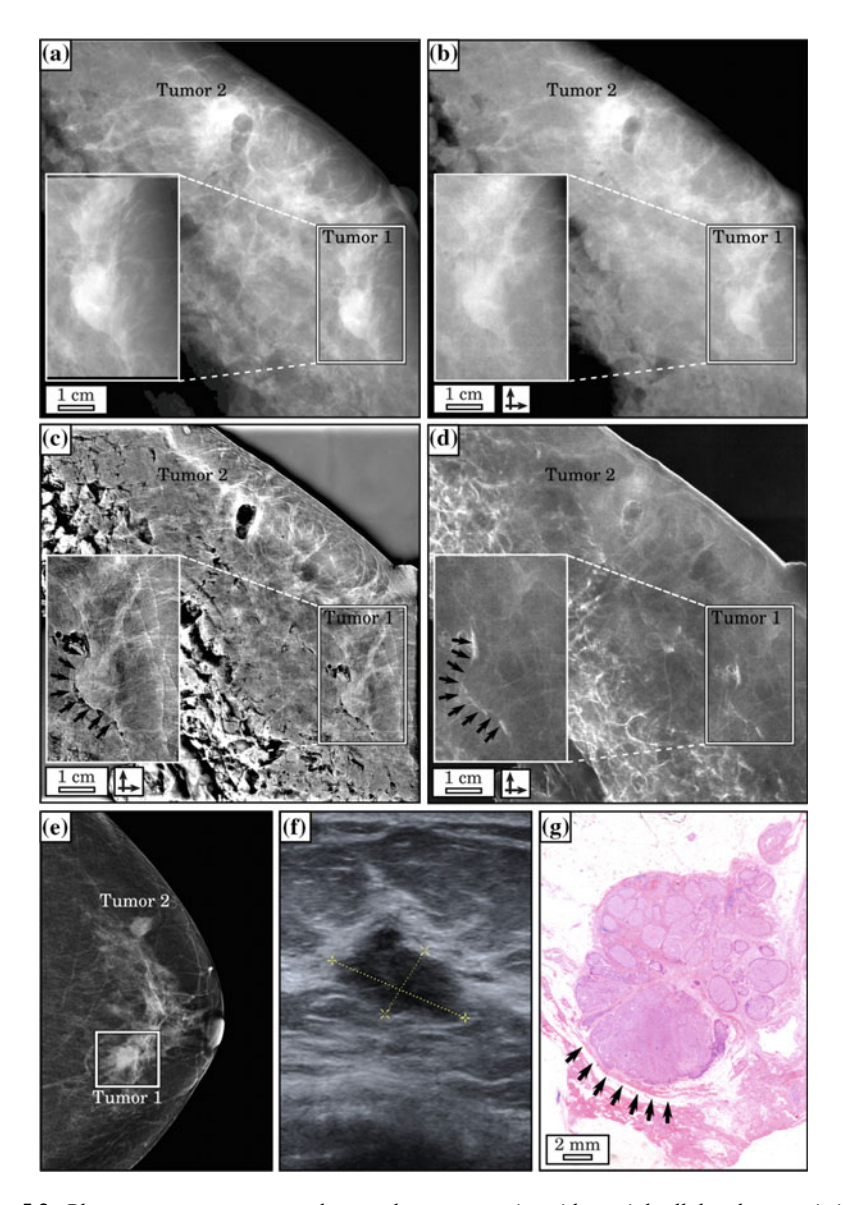


Fig. 5.3 Phase-contrast mammography reveals tumor margins with special cellular characteristics. Clinical ex-vivo mammography (**a**), experimental absorption-contrast mammography (**b**), phase-contrast mammography (**c**) and dark-field mammography (**d**); in-vivo mammography (**e**) of patient III in craniocaudal projection; white rectangle indicating tumor 1; ultrasonography of tumor 1 (**f**); histological image (hematoxylin-eosin staining) of tumor 1 (**g**); posterior margin of tumor 1 exhibiting a desmoplastic stromal reaction as indicated by black arrows in **c**, **d** and **g**. The crossed arrows in **b-d** indicate bi-directional measurements

5.2.4 Case IV | Phase-Contrast Mammography Reveals Actual Tumor Spread

Patient IV presented with an irregularly delineated tumor in the left breast. IV-Mx (Fig. 5.4e) revealed a suspicious lesion superimposed by breast parenchyma, measuring $2.5 \times 2.2 \, \mathrm{cm^2}$ which was prior to excision diagnosed as a cyst. Close to the cyst in mediocaudal direction a second mass of $2 \times 2 \, \mathrm{cm^2}$ with architectural disorders was found (pink arrows). Sonographically, the second mass yielded typical malignant features such as poor echogenicity and blurred margins, albeit was measured to $3.5 \times 1.6 \times 2.5 \, \mathrm{cm^3}$. Histopathology revealed the tumor as a $4 \times 2 \times 2 \, \mathrm{cm^3}$ moderately differentiated (G 2) invasive carcinoma of not specific type (NST) with infiltration into the surrounding tissue. Dynamic MRI including contrast-enhanced subtraction (Fig. 5.4f) and native T2-sequence imaging (Fig. 5.4g) were conducted to verify tumor and cyst, respectively.

Figure 5.4a—e show EV-Mx, A-Mx, PC-Mx, DF-Mx and differential phase-contrast mammography (DPC-Mx) of the breast specimen IV in craniocaudal orientation. Within IV-Mx, EV-Mx, A-Mx, PC-Mx the cyst and central tumor mass are equally well depicted and the latter measured to a maximum diameter of 2.2 cm. However, in PC-Mx and DPC-Mx multiple, horizontally aligned tissue strands outbonding the tumor (length of about 2 cm) in direction of the mammilla, are visible (framed inlays), remaining completely undetected by the other imaging modalities. Histological work-up verified a tumorous infiltration of the surrounding breast tissue with fine spiculations (arrows in Fig. 5.4j) and determined the maximum tumor size to 4 cm, supporting the findings of PC-Mx and DPC-Mx.

Similarly to patient II, the fine tissue strands provide an insufficient absorption contrast, further being superimposed by the underlying dense breast parenchyma. However, contrasting case II, no increased cellularity nor cell morphology was found within the spiculations, which presumably gives account to the absence of a prominent dark-field signal in patient IV. Surprisingly, even within the MRI contrastenhanced subtraction image (Fig. 5.4f) the spiculations were overlooked, possibly due to either a limited uptake of contrast agent within the fine spiculations or limited spatial resolution of MRI. As a consequence the tumor size was strongly underestimated with a maximum diameter of 3.2 cm only. Finally, PC-Mx and DPC-Mx provided the best depiction of the spiculations, utilizing an enhanced soft-tissue contrast but also increased image acutance gained by high-frequency boosted image details.

In addition, we found that DF-Mx (Fig. 5.4d) enables a strongly contrasting depiction of the microcalcified tumor core (pink arrows) and cyst encapsulation (blue arrows) from the surrounding, poorly scattering tissue. Also within the DPC-Mx (Fig. 5.4e) the sharp tissue demarcation between cyst encapsulation and embedding breast tissue is well resolved. Finally, note that the interior of the cyst, which is of fluid nature, does not exhibit any dark-field signal at all. Here, dark-field imaging yields the potential to improve diagnostics of highly suspicious cysts which currently need an aspiration of the comprised tissue to exclude malignant components [23].

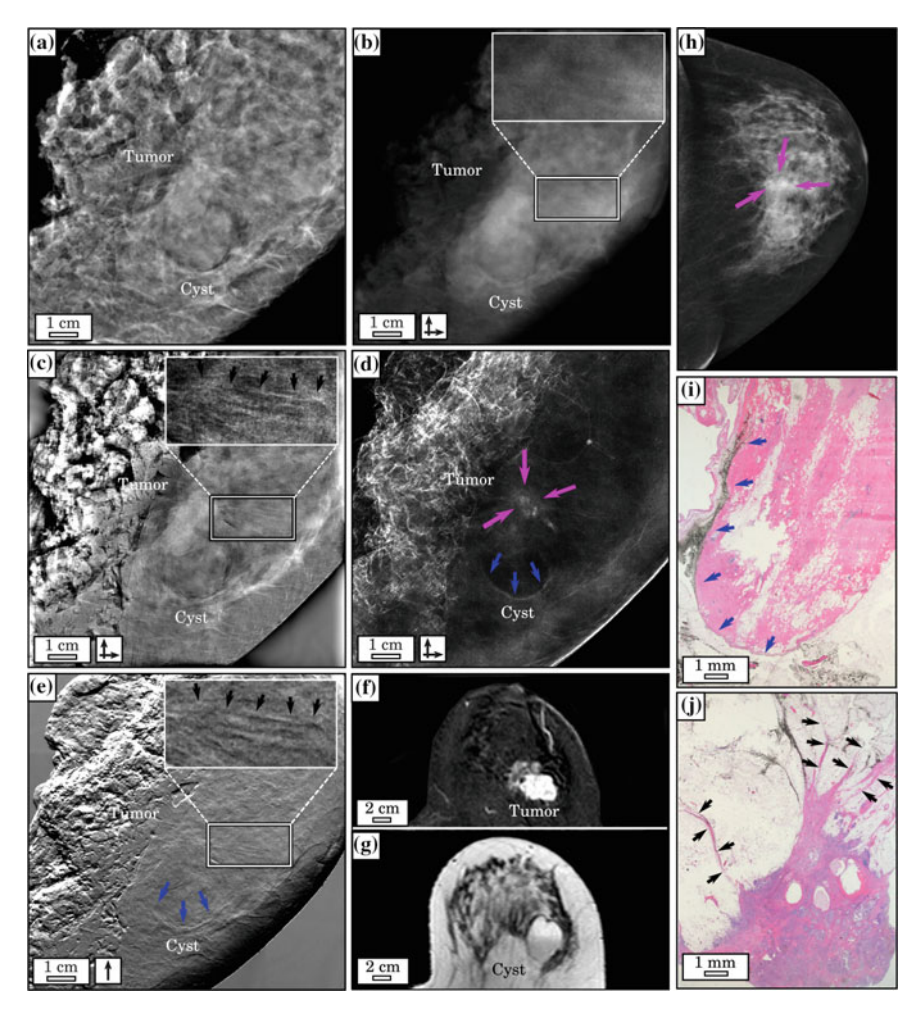


Fig. 5.4 *Phase-contrast mammography reveals actual tumor spread.* Clinical ex-vivo mammography (**a**), experimental absorption-contrast mammography (**b**), phase-contrast mammography (**c**), dark-field mammography (**d**) and differential phase-contrast mammography (**e**); in-vivo mammography (**h**) of patient IV in craniocaudal projection; *white rectangles* indicate area with tumor extensions; representative section from the in-vivo MRI including contrast-enhanced subtraction (**f**) and native T2-sequence image (**g**); histological image (hematoxylin-eosin staining) of the collapsed cyst (**i**); the cyst border is highlighted by *blue arrows* in **d**, **e** and **i**; histological image (hematoxylin-eosin staining) of the tumor (**j**); tumor core as indicated by *pink arrows* in **d** and **h**; tumor extensions as indicated by *black arrows* in **c**, **e** and **j**. The *single* and *crossed arrows* in **e** and **b**—**d** indicate one and bi-directional measurements, respectively

5.3 Discussion | Phase-Contrast Mammography as a Promising Candidate for Clinical Screening

In this ex-vivo study on four selected mastectomy samples containing bi- and multifocal carcinoma, we evaluated the diagnostic value of grating-based phase-contrast and dark-field mammography at a conventional, polychromatic X-ray source. We showed that dark-field mammography provides complementary information in comparison with conventional imaging, by revealing tissue strands emerging from the tumor, detecting microcalcified tumor nodules and depicting focality and tumor margins in correlation with histology.

Until now, only a few investigations lay their focus on the diagnostic value of darkfield imaging of dissected breast samples [17–22]. Stampanoni, M. et al. analyzed five mastectomy samples using phase-contrast mammography and found that the fused images created from the grating-based absorption, phase and dark-field signals enable a better visualization of small tumors, skin infiltration and differentiation between scars, healthy tissue and invasive cancer [21]. A blinded follow-up reader study came to the conclusion that the fused images outperform conventional digital mammograms in terms of overall image quality and sharpness [22]. Our results confirm these findings, indicating an improved visibility of high-frequency features (tissue strands, tumor margins, spiculations and cyst margins) within phase-contrast mammograms. Moreover, we could demonstrate that sub-resolution dark-field sensitivity helps to detect highly dispersed microcalcifications when examining complete breast samples that are not visible in other modalities due to size and volume, but that are nonetheless indicative of malignancy. This is accordance with studies by Michel, T. et al. who analyzed slices of cancer-bearing breast samples [18]: they showed, that the presence of microcalcifications within the tumor results in a high dark-field signal albeit the microcalcifications were not detectable in the conventional mammogram.

Exceeding previously published studies on phase-contrast mammography on whole mastectomy samples, our study is exemplarily indicating that dark-field mammography may outperform all conventional imaging modalities in the detection of small or low-density tumor nodules, fine structures and delineation of tumor tissue. The correct determination of tumor size and margins including tumor branches—especially within dense breast tissue—may prevent incomplete resection and the need for follow-up resections. Moreover, the capability of detecting minor or highly dispersed calcium grains strongly facilitates the sensitivity towards incipient calcification-processes and therewith detection of early stage tumors. However, it still remains debatable, to which extent a higher sensitivity in the detection of calcifications, unresolved in conventional mammography, will influence the percentage of overdiagnosis and lead to additional breast biopsies.

One challenge in breast cancer treatment is the prevention of recurrent disease that can be caused by incomplete resection or unnoticed multifocality and multicentricity at the time of diagnosis. A considerable percentage (13–75%) of primary breast cancers occur as multifocal disease with often small satellite nodules not detected in conventional breast imaging [24]. Breast MRI has been shown to be more sensitive

in the detection of multifocality, but is time- and cost-intensive. Our results indicate that dark-field mammography yields the potential to detect small tumors, especially if micro-calcified, at a better resolution than MRI, even though additional lesions—depending on their localization—might still need further histological assessment.

While the experimental measurements were conducted within a clinically feasible frame (compact setup, conventional X-ray tube and adequate sample compression) the applied radiation dose exceeds the corresponding clinical ex-vivo value (average glandular dose ranging from 0.56 to 1.22 mGy) by far. The estimated glandular dose applied at our experimental setup was 66–72 mGy (total exposure time of 81 s) per projection and scan direction, depending on the sample thickness. Since measurements were not conducted dose-optimized, several aspects can be addressed to reduce the dose applied: an increase of 13.2–49.4 % setup fringe visibility by improving the beam quality (design energy, beam filtration) and grating quality (duty-cycle, grating substrate thickness, grating height) would already imply an approximately 14-fold decrease in dose for phase-contrast imaging. An optimization of the detector with respect to the design energy of 27 keV and the replacement of the X-ray target molybdenum with tungsten could further double the setup efficiency. A decrease of 9-3 s exposure time per step would further decrease the dose by a factor of 3. Corresponding "low"-dose measurements were exemplarily conducted in case of patient I (one scan direction) providing equivalent quality of detection for the microcalcified tumor nodules (Fig. 5.5a) and suggest that a much lower exposure time is practicable. These considerations would imply a reduction of dose down to 0.8 mGy (1.6 mGy in case of bi-directional scanning) which lies within the dose-limits of 2.5 mGy set by the European guidelines for mammography [25]. Note that the measurements pre-

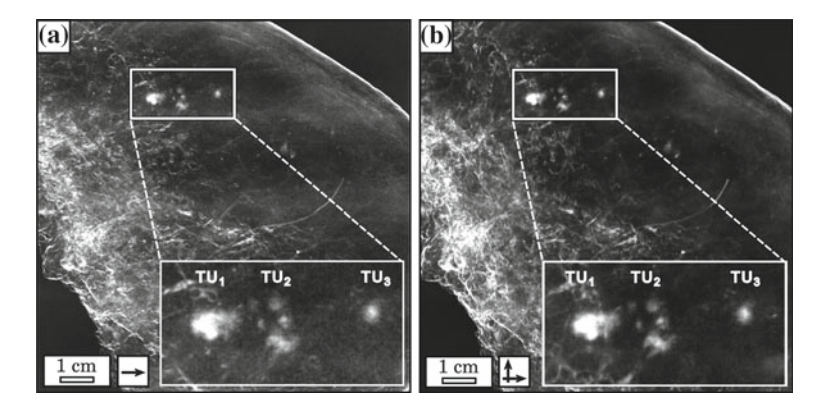


Fig. 5.5 Comparison of "low"- and high-dose dark-field mammography. **a** Low-dose (22 mGy mean glandular dose, 9 phase-steps, 3 seconds exposure time per phase-step) dark-field mammography of patient I conducted in one scan direction, as indicated by *arrow*. **b** Corresponding high-dose measurements (66 mGy mean glandular dose, 9 phase-steps, 9 seconds exposure time per phase-step) conducted in two scan directions, as indicated by *crossed arrows*. Both images offer equal quality in the detection of the tumor nodules

sented here were further conducted with the dose-unoptimized setup (for respective dose-compatible phase-contrast mammography cf. Chap. 7).

Keypoints

- Phase-contrast and dark-field mammography can outperform conventional imaging techniques for certain indications.
- Dark-field mammography is sensitive to both calcified and non-calcified tumorous structures.
- Phase-contrast mammography provides significantly enhanced visualization of fine tumor features.

Currently phase-contrast imaging suffers from limited clinical experience and needs further technical improvements. Previous studies demonstrate few selected cancer cases and up to now, no independent multi-reader studies with larger patient cohorts and lower prevalence of malignancy were performed. Thus, future studies will have to focus on the specific value of grating-based phase-contrast imaging for different tumor entities and on larger patient cohorts to identify those patients that will benefit the most from this promising additional imaging modality with the final goal of introducing phase-contrast mammography into clinical screening.

5.4 Materials and Methods

5.4.1 Study Design and Sample Acquisition

The study was conducted in accordance with the Declaration of Helsinki and was approved by the local ethics committee. The four selected patients suffering from multifocal breast cancer were chosen from a collective of a prospective study on ex-vivo phase-contrast mammography. From September 2012 to August 2013, all patients undergoing mastectomy were asked to take part in the study. All participants gave written informed consent before inclusion after adequate explanation of the study protocol. Indication to breast surgery followed recommendation of the interdisciplinary tumor conference. Inclusion criteria were a histologically proven breast cancer in preoperative core biopsy with a recommendation to mastectomy according to gynaecological guidelines or the patients wish for mastectomy as well as completed preoperative conventional breast diagnostics (mammography, ultrasound, +/- MRI).

The study was conducted in accordance with the Declaration of Helsinki and was approved by the local ethics committee. All participants gave written informed consent before inclusion after adequate explanation of the study protocol.

5.4.2 Imaging Dose

The average glandular radiation dose of the in-vivo mammography automatically registered by the mammography unit was 0.40 and 0.41 mGy for sample I, 1.21 and 1.27 mGy for sample II and 1.35 and 1.26 mGy for sample III and 1.42 and 1.44 mGy for sample IV (mediolateral oblique projection and craniocaudal projection, respectively). The average glandular radiation dose of the ex-vivo clinical mammography was 0.56 mGy for sample I, 1.22 mGy for sample II and 1.18 mGy for sample III and 1.31 mGy for specimen IV. The radiation dose of the experimental mammography was approximated by determining the incident air kerma (2.1 mGy/s) with a Dosimax plus/RQX detector system. The mean glandular dose was calculated by weighting this value with a Monte-Carlo based conversion factor of 0.389–0.422, determined by the half-value layer (Al) of 0.8 mm and breast thicknesses ranging from 4.5 to 5.0 cm [26, 27].

5.4.3 Preoperative Diagnostics

Preoperative diagnostics included clinical breast examination, clinical standard two-view digital mammography in craniocaudal (CC) and mediolateral oblique (MLO) projections (Hologic Selenia Dimensions, Bedford, USA) using a standard breast compression paddle and high resolution B-mode ultrasonography (standard linear transducer 13.5 MHz, Siemens Acuson Antares, Siemens Healthcare, Germany). For one patient additional MRI was performed by using a dedicated sensitivity-encoding-enabled bilateral breast coil with a 3.0 Tesla system (Magnetom Verio, Siemens Healthcare, Germany).

5.4.4 Histological Work-Up

Image data acquisition was followed by standard histological work-up according to histopathological diagnostic guidelines. The abladates were fixated in a 4% neutral-buffered formaldehyde solution immediately after image acquisition. The formaldehyde-fixated samples were cut into 5 mm slices. Representative tissue sections were dehydrated in an ascending alcohol series before embedding in hot paraffin wax. The paraffin blocks were cut into 5 μ m sections using a standard microtome and sections were stained with hematoxylin and eosin using standard protocols.

5.4.5 Ex-Vivo Clinical Mammography

The breast abladates were intraoperatively marked with surgical sutures for 3-D orientation. The samples were fixed in craniocaudal position within a metal-framed sample-holder realizing adequate breast compression. In order to ensure comparability, both a digital ex-vivo mammography at a clinical mammomat (Hologic Selenia Dimensions, Bedford, USA) with a pixel size of $70 \times 70 \, \mu m^2$ and an experimental grating-based phase-contrast mammography with an effective pixel size of $85 \times 85 \, \mu m^2$ were conducted without changing the sample position within the sample-holder.

5.4.6 Correlation Phase-Contrast Mammography, Ex-Vivo Mammography, In-Vivo Imaging and Histology

Phase-contrast and dark-field mammography of each sample were compared with preoperative in-vivo standard imaging in consensus by three radiologists experienced in breast diagnostics who were blinded for the histopathological diagnosis. Afterwards, the findings were correlated with corresponding histological sections by a pathologist specialized in breast diagnostics.

References

- 1. Marmot, M., et al. (2013). The benefits and harms of breast cancer screening: An independent review. *British Journal of Cancer*, 108, 2205–2240.
- 2. Ferlay, J., et al. (2010). Estimates of worldwide burden of cancer in 2008. *International Journal of Cancer*, 127, 2893–2917.
- 3. Pinsky, R., & Helvie, M. (2010). Mammographic breast density: Effect on imaging and breast cancer risk. *Journal of the National Comprehensive Cancer*, 8, 1157–1164.
- 4. Schrading, S., & Kuhl, C. (2008). Mammographic, US, and MR imaging phenotypes of familial breast cancer. *Radiology*, 246, 58–70.
- Tilanus-Linthorst, M., et al. (2002). A BRCA1/2 mutation, high breast density and prominent pushing margins of a tumor independently contribute to a frequent false-negative mammography. *International Journal of Cancer*, 102, 91–95.
- 6. Lee, C., & Weinreb, J. (2004). The use of magnetic resonance imaging in breast cancer screening. *Journal of the American College of Radiology*, 1, 176–182.
- 7. Sardanelli, F., et al. (2004). Sensitivity of MRI versus mammography for detecting foci of multifocal, multicentric breast cancer in fatty and dense breasts using the whole-breast pathologic examination as a gold standard. *American Journal of Roentgenology*, 183, 1149–1157.
- 8. Murphy, K., Brunberg, J., & Cohan, R. (1996). Adverse reactions to gadolinium contrast media: A review of 36 cases. *American Journal of Roentgenology*, 167, 847–849.
- 9. Bermejo-Perez, M., Marquez-Calderon, S., & Llanos-Mendez, A. (2008). Cancer surveillance based on imaging techniques in carriers of BRCA1/2 gene mutations: A systematic review. *British Journal of Radiology*, 81, 172–179.
- Berg, W., et al. (2008). Combined screening with ultrasound and mammography versus mammography alone in women at elevated risk of breast cancer. *JAMA*, 299, 2151–2163.

References 75

 Moon, H., et al. (2014). Comparison of cancer yields and diagnostic performance of screening mammography vs. supplemental screening ultrasound in 4394 women with average risk for breast cancer. *Ultraschall in der Medizin*. doi:10.1055/s-0034-1366288.

- 12. Sanchez del Rio, M., & Dejus, R. (2011). XOP v2.4: Recent developments of the X-ray optics software toolkit. *Proceedings of SPIE*, 8141, 814115.
- Keyriläinen, J., et al. (2010). Phase-contrast X-ray imaging of breast. Acta Radiologica, 51, 866–884.
- 14. Arfelli, F., et al. (2000). Mammography with synchrotron radiation: Phase-detection techniques. *Radiology*, 215, 286–293.
- 15. Takeda, T., et al. (1998). Phase-contrast X-ray CT image of breast tumor. *Journal of Synchrotron Radiation*, 5, 1133–1135.
- 16. Yashiro, W., et al. (2010). On the origin of visibility contrast in X-ray Talbot interferometry. *Optics Express*, 18, 16890–16901.
- 17. Anton, G., et al. (2013). Grating-based darkfield imaging of human breast tissue. *Zeitschrift fur Medizinische Physik*, 23, 228–235.
- 18. Michel, T., et al. (2013). On a dark-field signal generated by micrometer-sized calcifications in phase-contrast mammography. *Physics in Medicine and Biology*, 58, 2713–2732.
- 19. Pfeiffer, F., et al. (2006). Phase retrieval and differential phase-contrast imaging with low-brilliance X-ray sources. *Nature Physics*, 2, 258–261.
- Pfeiffer, F., et al. (2008). Hard-X-ray dark-field imaging using a grating interferometer. *Nature Materials*, 7, 134–137.
- 21. Stampanoni, M., et al. (2011). The first analysis and clinical evaluation of native breast tissue using differential phase-contrast mammography. *Investigative Radiology*, 46, 801–806.
- Hauser, N., et al. (2014). A study on mastectomy samples to evaluate breast imaging quality and potential clinical relevance of differential phase contrast mammography. *Investigative Radiology*, 49, 131–137.
- Mannello, F., & Tonti, G. (2006). Benign breast diseases: Classification, diagnosis, and management. Oncologist, 11, 1132–1134.
- 24. Bendifallah, S., et al. (2010). Multiple synchronous (multifocal and multicentric) breast cancer: Clinical implications. *Surgical Oncology*, *19*, 115–123.
- 25. Perry, N., et al. (2008). European guidelines for quality assurance in breast cancer screening and diagnosis. Fourth edition-summary document. *Annals of Oncology*, *19*, 614–622.
- 26. Dance, D. (1990). Monte carlo calculation of conversion factors for the estimation of mean glandular breast dose. *Physics in Medicine and Biology*, *35*, 1211–1219.
- 27. Dance, D., Skinner, C., Young, K., Beckett, J., & Kotre, C. (2000). Additional factors for the estimation of mean glandular breast dose using the UK mammography dosimetry protocol. *Physics in Medicine and Biology*, 45, 3225.

Chapter 6 Microcalcification Assessment with Dark-Field Mammography

Look deep into nature, and then you will understand everything better.

Albert Einstein

Abstract In this chapter, a dose-compatible diagnostic tool for the assessment and risk stratification of breast microcalcifications exploiting the sub-pixel resolution sensitivity of X-ray dark-field is presented. First, the diagnostic importance of breast microcalcification grading and its clinical limitations are illustrated, by which the necessity and potential of additional, refining classification procedures is given credit. Our results indicate that dark-field imaging of microcalcifications may enhance the diagnostic validity of current microcalcification analysis and reduce the number of invasive procedures. Finally, we take a critical look at a recent publication, which suggest a chemically-based assessment of calcifications by means of dark-field mammography. Note that this chapter has been submitted for publication to Scientific Reports as "Scherer, K. et al. Improved mammography diagnostics by assessing the micromorphology of breast calcifications via X-Ray dark-field radiography".

6.1 Motivation | Limitations of Conventional Microcalcification Analyses

In diagnostic mammography breast microcalcifications (clusters) are the primary evidence in the detection and assessment of early stage breast cancer (carcinoma insitu) and impalpable tumor lesions [1, 2]. Geometrical features such as position, size, shape and appearance of microcalcifications within the breast indicate their possible origin as either benign or cancerous cell processes [3–5]. Morphology and distribution descriptors (BIRADS) help to categorize microcalcifications and classify the malignancy risk of the corresponding breast tissue, hence determining the need for invasive assessment and follow-up procedures [6–8]. However, a clear assignment

as benign or malignant is only possible for a few characteristic microcalcification configurations such as egg, popcorn, skin (benign), fine linear and branching shapes (malignant) [9]. The predominant number of microcalcification types exhibit an unspecific, amorphous, coarse heterogeneous or pleomorphic pattern in the mammogram, which is graded as uncertain and of intermediate concern resulting in a high rate of benign biopsies [10–12].

Diagnostic potential and validity of current microcalcification analyses is limited by the fact that morphological descriptors are restricted to the global appearance of microcalcification clusters, since their microstructure remains spatially unresolved with clinical mammography systems (resolution of 70–100 μm) [13]. Furthermore, evaluation is susceptible to projection-based superposition effects within the microcalcification cluster [14]. Recent literature however gives strong evidence that spatial information on the interior morphology of microcalcifications could complement and refine the conventional assessment and grading of microcalcifications in clinical examination: Gufler, H. et al. reported in ex-vivo microCT studies investigating biopsy samples (resolution of 8.4 µm) that benign microcalcifications exhibit a lamellar-trabecular micromorphology while malignant microcalcifications are composed of granulous substructures [15]. Imamura, K. et al. used synchrotron radiation imaging (resolution of 6 µm) to demonstrate that pleomorphic microcalcifications consist of a significantly higher ratio of fine, clustered specks than amorphous microcalcifications [16]. Finally, Langen, H. et al. revealed calcifications which appeared linear on conventional radiography (12 Lp/mm), thus assigned as high risk calcification, as a superposition of harmless, round microcalcifications by using highresolution microradiography (2000 Lp/mm) [17]. A corresponding example showing a fibrocystic mastopathy with sclerosing adenosis (benign) is depicted in Fig. 6.1.

Although previous ex-vivo case studies showed an improved diagnostic discriminability between malignant and benign microcalcifications by assessment of their 3D-micro-morphology for certain indications, the underlying imaging techniques are unsuitable for clinical, in-vivo mammography: sufficient resolution of the micromorphology requires detector pixel sizes of an order of magnitude smaller than commonly used in clinical mammography. The implementation of adequate detectors would involve an immensely increased imaging dose, incompatible with the dose limits for clinical mammography and patient health.

Here we present an alternative, indirect imaging approach based on a laboratory Talbot-Lau Interferometer (incoherent X-ray source, flat panel detector with pixel size of 127 μ m, radiographic imaging mode) meeting the requirements of a clinical implementation in the near future [18–20]. The key factor of the presented method is the simultaneous measurement of absorption (relative decrease in transmission T) and dark-field signal (relative decrease in fringe-visibility V) with a grating-based phase stepping approach. These two contrasts allow the determination and comparison of material specific absorption power $\bar{\mu}$ and scattering power $\bar{\epsilon}$ of the investigated specimen [21]. Malecki, A. et al. simulated various microstructure textures composed of randomly distributed spheres and showed that spatial variations of structural parameters far below the detector pixel resolution limit strongly impact the ratio of absorption $\bar{\mu}$ to scatter power $\bar{\epsilon}$ [22]. Schleede, S. et al. utilized this

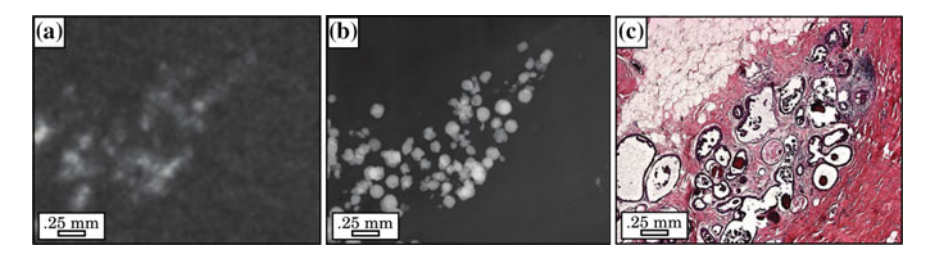


Fig. 6.1 High-resolution microradiography reveals suspicious microcalcifications as being benign. a Conventional specimen radiography showing microcalcifications with a typical malignant amorphous, linear shape. b High-resolution microradiography reveals the microcalcification cluster as a superposition of round and harmless calcifications. c Histological slice showing round calcifications associated with a fibrocystic mastopathy with sclerosing adenosis (benign). Figure adapted from Langen, H. et al. (2012) [17]

correlation to reveal changes within the microstructure of emphysematous mouse lungs, namely the decay of lung alveoli with disease progression accompanied by a strong decrease in provided scattering power $\bar{\epsilon}$, and could successfully discriminate these from healthy lungs [23].

We adapt this formalism to obtain spatial information on the inherent, subresolution structure of microcalcification clusters, by associating $\bar{\mu}$ with the overall calcium volume and $\bar{\epsilon}$ with the calcified interface along the beam in one detector pixel, respectively. The pixel-wise comparison of $\bar{\mu}$ and $\bar{\epsilon}$ (named "normalized scatter") then provides a measure of the microscopic surface-to-volume ratio exhibited by the calcium particles enclosed within a particular microcalcification cluster and can be considered as decoupled from the total microcalcification cluster thickness. Consequently, we utilize the mean $\bar{\mu}/\bar{\epsilon}$ -ratio determined over the total calcified area, as a micro-morphological classifier, by which differentiation of fine calcium grain configurations $(\bar{\epsilon} \gg \bar{\mu})$ from coarse, compact ones $(\bar{\epsilon} \approx \bar{\mu})$ is possible. We verify this hypothesis by correlating the $\bar{\mu}$ and $\bar{\epsilon}$ measurements of 15 biopsied microcalcification clusters, evaluated with grating-based dark-field mammography (at an effective resolution of 85 µm), with separately obtained, highly resolved micro-CT images (at an effective resolution of 6 µm). We further test dark-field mammography as a potential indicator of early tumor malignancy by evaluating 31 biopsied microcalcification clusters with respect to their histopathological findings.

Finally, our study raises a major issue in the conceptual design of a recent publication by Wang, Z. et al., in which the $\bar{\mu}/\bar{\epsilon}$ -ratio is utilized for the differentiation of calcium oxalate dehydrate and calcium hydroxyapatite breast calcifications [24]. Here the authors relate variations in the $\bar{\mu}/\bar{\epsilon}$ -ratio of microcalcifications to their chemical composition, while overlooking the impact of microstructural properties in scatter-based contrast generation.

6.2 Results

6.2.1 In-Situ Microcalcification Assessment with Dark-Field Mammography

At first, native breast tissue was investigated, to ascertain whether microcalcification assessment with dark-field mammography is clinically applicable. With a lab-based, three grating Talbot-Lau Interferometer (Fig. 6.2a), absorption (Fig. 6.2b) and dark-field images (Fig. 6.2c) of the un-fixated, freshly dissected mastectomy, comprising a distinct microcalcification cluster, were retrieved and stitched from 16 single projections. Subsequently the included cluster was excised, embedded in paraffin and comparative measurements performed, for the purpose of demonstrating that micromorphology classification is achievable independently from the surrounding material composition or thickness. The absorption (Fig. 6.2d) and dark-field images (Fig. 6.2e) of the biopsied tissue show the microcalcification cluster in different orientation compared to the mastectomy case.

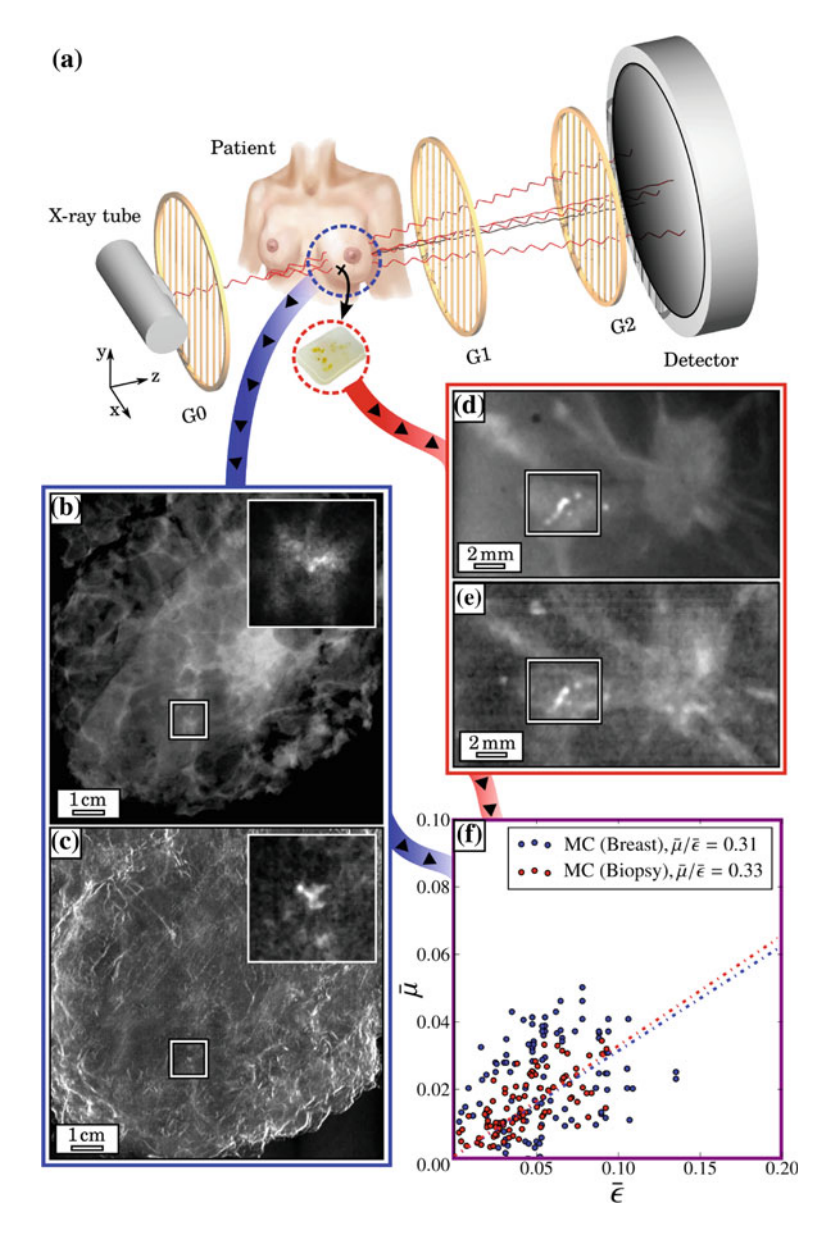
The measured signals were normalized with respect to the tissue surrounding the microcalcification in order to compensate for absorption and scattering contributions of the underlying tissue in the beam direction as explained in Sect. 6.4.2. This way, the decrease of beam intensity and fringe visibility caused by only the microcalcification cluster is retrieved. The measured absorption power $\bar{\mu}$ and scattering power $\bar{\epsilon}$ provided by the microcalcification cluster are deduced as the negative logarithm of the normalized transmission (T_c) and visibility signals (V_c) respectively by

$$\bar{\mu} = \int_0^{d_c} \mu_c(z) \, dz = -\ln T_c, \quad \bar{\epsilon} = i \int_0^{d_c} \epsilon_c(z) \, dz = -\ln V_c,$$
 (6.1)

hence equal the integral of linear attenuation coefficient $\mu_c(z)$ and linear diffusion coefficient $\epsilon_c(z)$ over the spatial mean thickness of the microcalcification cluster d_c respectively, where i is an interferometer-specific constant [25].

For each pixel within the calcified area in the cases of the native breast (blue) and subsequently biopsied microcalcification cluster (red), the values of $\bar{\mu}$ and $\bar{\epsilon}$ were paired and plotted within a scatter plot (Fig. 6.2f). Due to a change of cluster orientation with respect to the X-ray beam, accompanied by the excision and embedding process, corresponding projection-based data points differ slightly. However, the overall absorption and scattering power is preserved, since the microscopic surface-to-volume ratio of the microcalcification cluster remains unaltered. The mean $\bar{\mu}/\bar{\epsilon}$ -ratios were determined to 0.31 (\pm 0.02) in the case of native breast and 0.33 (\pm 0.01) in the case of the embedded biopsied microcalcification using a linear least squares fit and were found to be consistent within the error margins. This result demonstrates that the mean $\bar{\mu}/\bar{\epsilon}$ -ratio is a suitable micromorphological classifier, being unaffected by cluster orientation and embedding material/tissue and justifies the medical relevance of investigating biopsied microcalcification clusters in this study.

6.2 Results 81



◄ Fig. 6.2 *In-situ microcalcification assessment with dark-field mammography.* **a** Sketch of the dark-field mammography setup, consisting of a conventional X-ray tube, a source grating G_0 , a phase grating G_1 , an analyser grating G_2 and a flat panel detector. Absorption (**b**) and dark-field images **c** of a cancerous mastectomy specimen with native microcalcification cluster. The *insets* show magnified images of the microcalcification cluster. Absorption (**d**) and dark-field images **e** of the biopsied and paraffin embedded microcalcification cluster. **f** Scatter plot comparing absorption $\bar{\mu}$ to scattering power $\bar{\epsilon}$ of the native (*blue*) and subsequently biopsied microcalcification cluster (*red*). Mean $\bar{\mu}/\bar{\epsilon}$ -ratios of 0.31 ± 0.02 (Breast) and 0.33 ± 0.01 (Biopsy) are consistent within the error margins, suggesting that microcalcification assessment via dark-field mammography is suitable as an in-situ application

6.2.2 Dependence of Absorption $\bar{\mu}$ and Scattering Power $\bar{\epsilon}$ of Microcalcification Clusters on Their Inherent Micromorphology

In order to understand how $\bar{\mu}$ and $\bar{\epsilon}$ depend on the interior structure of microcalcification clusters, 15 biopsies were additionally investigated with micro-CT measurements (6 μ m resolution). In Fig. 6.3, the data points of four microcalcification clusters with significantly differing microstructures are compared, which are representative of the ultra-fine, fine, pleomorphic and coarse classes. It is apparent that both the slope and pattern of the measured scatter plots vary strongly between the microstructure classes.

The microcalcification with ultra-fine microtexture (blue framed) yields a distinctively uniform micromorphology consisting of very small calcium particles (grain radius of $r \approx 75 \,\mu$ m) only. According to expectations, this configuration is strongly scattering and hardly absorbing, resulting in the flattest slope ($\bar{\mu}/\bar{\epsilon}=0.14$) of all investigated data. Furthermore, the spread of data points is small ($Var(\bar{\mu}/\bar{\epsilon}) = 0.003$), indicating a high degree of regularity in particle size. The microcalcification cluster with fine microstructure (red framed) comprises some additional larger calcium particles ($r \approx 175 \,\mu\text{m}$), causing a slight increase in overall absorption power $\bar{\mu}$, in comparison to the ultra-fine microstructure. Besides, a larger particle correlates well with a few isolated data points ($Var(\bar{\mu}/\bar{\epsilon}) = 0.008$), which exceed the average $\bar{\mu}/\bar{\epsilon}$ ratio of 0.26 with respect to absorption power $\bar{\mu}$. A very pronounced diversification in inherent grain sizes was found in the case of the pleomorphic microcalcification cluster (purple framed). This microstructure comprises a strongly inhomogeneous $(Var(\bar{\mu}/\bar{\epsilon}) = 0.89)$, yet separated mix of very small $(r \approx 75 \,\mu\text{m})$ and distinctly larger calcium particles ($r \approx 275 \,\mu\text{m}$), causing an overall steeper slope of the data points $(\bar{\mu}/\bar{\epsilon} = 0.46)$, with separation into a strongly scattering/poorly absorbing (small particles for $\bar{\mu}/\bar{\epsilon} < 0.46$) as well as a poorly scattering/strongly absorbing branch (large particles for $\bar{\mu}/\bar{\epsilon} > 0.46$), respectively. The steepest slope was found for the microcalcification cluster with coarse texture (green framed). The distinctive feature for this class is a compact micromorphology, comprising very large calcium structures only $(r \approx 700 \,\mu\text{m})$ while lacking tiny grains $(\text{Var}(\bar{\mu}/\bar{\epsilon}) = 0.32)$. Here the microscopic surface-to-volume ratio exhibited by the microcalcification cluster

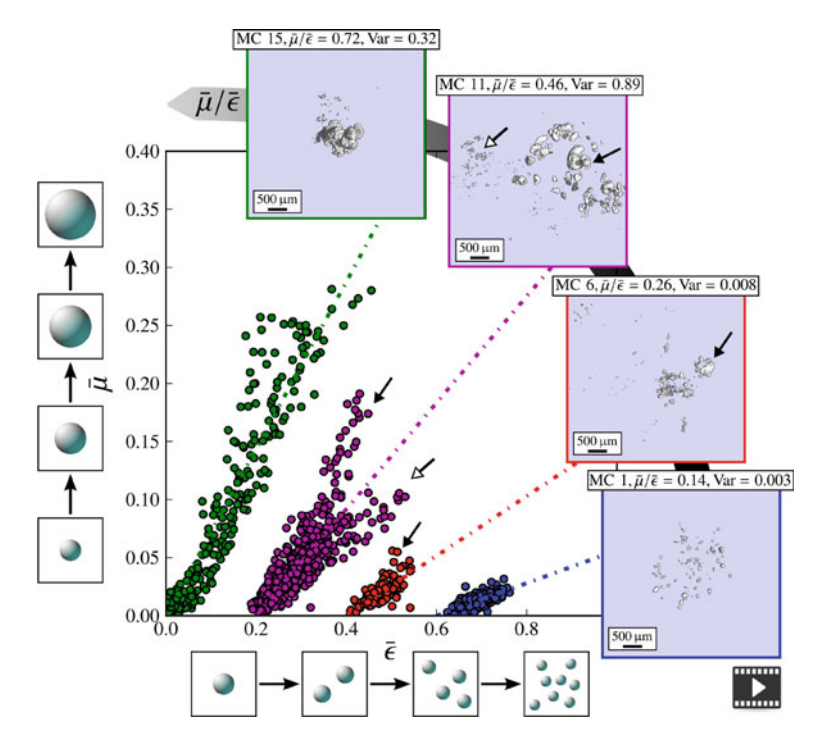


Fig. 6.3 Dependence of absorption and scattering characteristics of microcalcification clusters on their inherent micromorphology. Scatter plots comparing the absorption $\bar{\mu}$ to scattering power $\bar{\epsilon}$ of four microcalcification clusters, representative of the ultra-fine (blue), fine (red), pleomorphic (purple) and coarse (green) microtexture classes together with corresponding micro-CT images. For clarity, data points are shifted in $\bar{\epsilon}$ -direction by a value of 0.2 each. Discriminative mean $\bar{\mu}/\bar{\epsilon}$ -ratios of 0.14, 0.26, 0.46 and 0.72 were found to be strongly different for each of the four microtexture classes. A measure on the degree of regularity in calcium grain sizes is given by the variance of data points. Structural characteristic, i.e. a distinct diversification in grain size in the case of the pleomorphic microtexture, are consistent with the scatter data as indicated by arrows. For a respective rendering find Fig. A.1

is minimized, indicated by a strongly increased absorption $\bar{\mu}$ and decreased scattering power $\bar{\epsilon}$, respectively ($\bar{\mu}/\bar{\epsilon}=0.72$). Consequently, by determining the slope and spread (variance) of $\bar{\mu}$ and $\bar{\epsilon}$ of microcalcification clusters, a measure of the mean particle size and size distribution of calcium grains can be obtained.

To quantitatively investigate the dependence of the $\bar{\mu}/\bar{\epsilon}$ -ratio on the microstructure, particle-surface distributions were exemplary deduced: the corresponding micro-CT volumes were thresholded, each microparticle was fitted on a voxel-based segmentation algorithm, its volume and surface interpolated and the total microcalcification surface σ accumulated, as explained in Sect. 6.4.4. The particle-surface distribution then quantifies surface-to-volume characteristics of each cluster, by specifying the relative amount of surface occupied by calcium grains σ_r/σ , dependent on their grain size r (respectively volume).

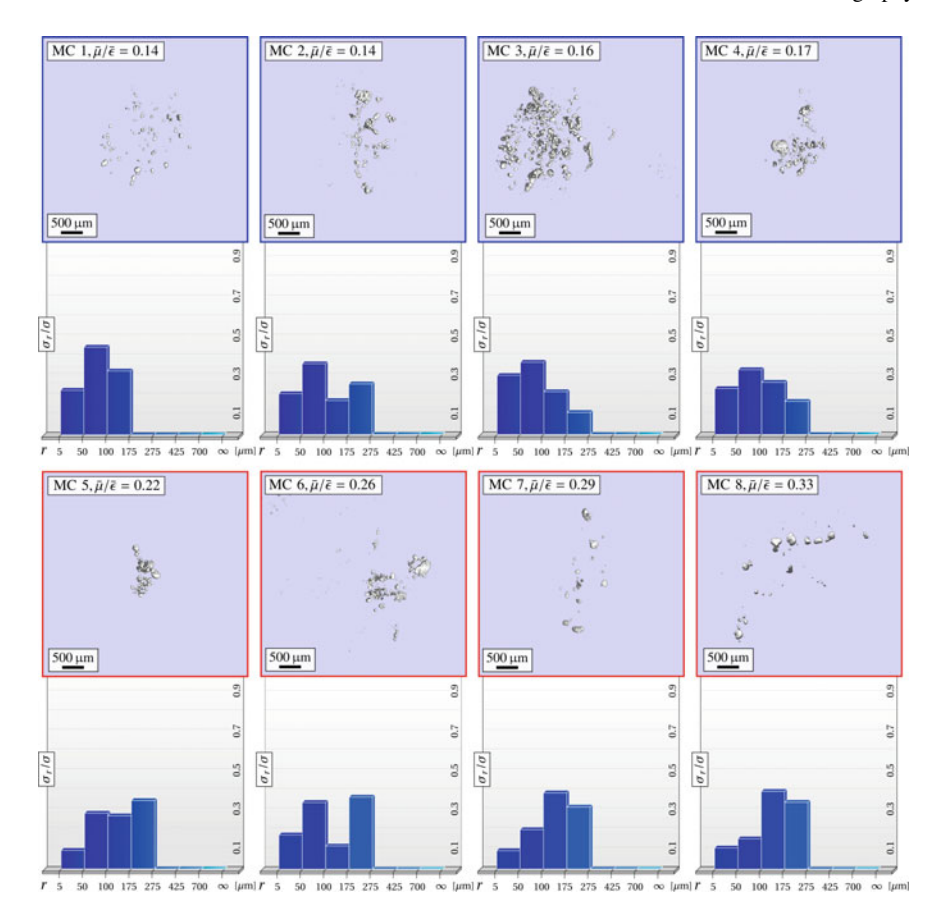


Fig. 6.4 Quantitative classification of microcalcification clusters utilizing the correlation between micromorphology and mean $\bar{\mu}/\bar{\epsilon}$ -ratio (I). Overview of 8 microcalcification clusters (micro-CT images) sorted with increasing mean $\bar{\mu}/\bar{\epsilon}$ -ratio and particle-surface distribution σ_r/σ , quantifying their inherent microstructure. A consistent relation between the mean $\bar{\mu}/\bar{\epsilon}$ -ratio and the micromorphological descriptor σ_r/σ was found, by which a categorical classification in ultra-fine (blue) and fine micromorphologies (red) is feasible

In Figs. 6.4 and 6.5 we compare the mean $\bar{\mu}/\bar{\epsilon}$ -ratios (sorted in increasing order), the interior morphology and particle-surface distributions σ_r/σ of 15 microcalcification clusters. We found a high correlation between $\bar{\mu}/\bar{\epsilon}$ and σ_r/σ with characteristic values for each of the four microtexture classes, as summarized in Table. 6.1.

Microcalcification clusters, exhibiting a mean $\bar{\mu}/\bar{\epsilon}$ -ratio below 0.33 (MC 1–8), were found to be exclusively composed of calcium grains smaller than 275 μ m in radius. Within this class, microcalcifications meeting the requirement of $\bar{\mu}/\bar{\epsilon} \leq 0.17$ could be further differentiated as ultra-fine (MC 1–4) where more then 70 % of the overall cluster surface is occupied by ultra small grains ($r \leq 175 \,\mu$ m). Microcalcifications with fine texture (MC 5–8) yielded a $\bar{\mu}/\bar{\epsilon}$ -ratio between 0.22 and 0.33 and

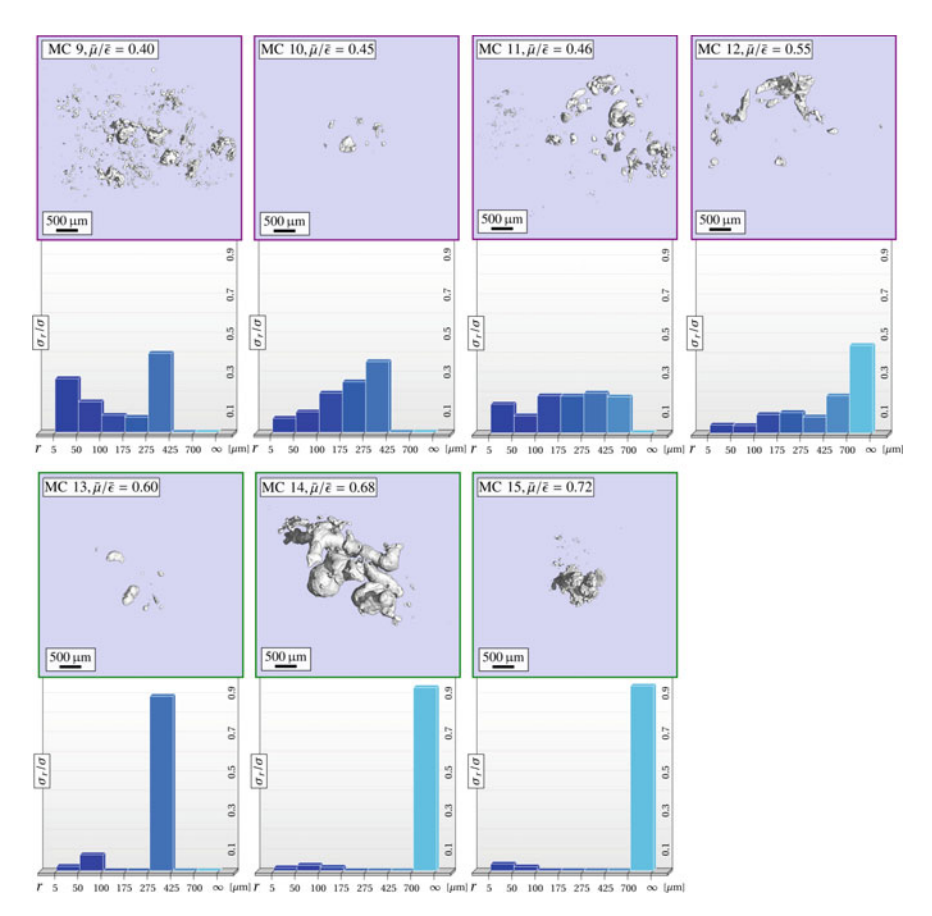


Fig. 6.5 Quantitative classification of microcalcification clusters utilizing the correlation between micromorphology and mean $\bar{\mu}/\bar{\epsilon}$ -ratio (II). Overview of 7 microcalcification clusters (micro-CT images) sorted with increasing mean $\bar{\mu}/\bar{\epsilon}$ -ratio and particle-surface distribution σ_r/σ , quantifying their inherent microstructure. A consistent relation between the mean $\bar{\mu}/\bar{\epsilon}$ -ratio and the micromorphological descriptor σ_r/σ was found, by which a categorical classification in pleomorphic (purple) and coarse micromorphologies (green) is feasible. Note that the mean $\bar{\mu}/\bar{\epsilon}$ -ratio between microcalcification clusters can differ by more then 500 %, as for instance when comparing MC 1 against MC 15

comprised more of slightly larger particles ($175 \le r \le 275 \,\mu\text{m}$) which contribute to more then 30 % of the overall surface. The smallest $\bar{\mu}/\bar{\epsilon}$ -ratio of 0.14 was obtained for an ultra-fine microcalcification cluster (MC 1), with no grains bigger than 175 $\,\mu\text{m}$ in radius.

Four $\bar{\mu}/\bar{\epsilon}$ -ratios between 0.4 and 0.55 were measured for microcalcification clusters with strongly pleomorphic microstructure (MC 9–12). Intermediate $\bar{\mu}/\bar{\epsilon}$ -ratios can be attributed to a broad spectrum of included grain sizes and therefore averaging of scattering and absorption contributions related to small and larger particles, respectively. The pleomorphic nature of this class is well indicated by the

Microcalcification	Microtexture Class	σ_r/σ	$ \bar{\mu}/\bar{\epsilon} $
MC 1-4	Ultra-fine	$\left[\sigma_{r\leq 175\mu\text{m}}/\sigma\right]\geq 0.7$	≤ 0.17
	$(r_{\text{max}} \leq 275 \mu\text{m})$		
MC 5-8	Fine $(r_{\text{max}} \le 275 \mu\text{m})$	$\left[\sigma_{r \le 175 \mu\text{m}}/\sigma\right] \le 0.7$	0.22 - 0.33
MC 9-12	Pleomorphic	0.25 ≤	0.40 - 0.55
		$\left[\sigma_{r\geq 275\mu\text{m}}/\sigma\right]\leq 0.75$	
MC 13-15	Coarse	$[\sigma_{r \ge 275\mu\text{m}}/\sigma] \ge 0.85$	≥ 0.6

 Table 6.1 Quantitative classification of microcalcification clusters

Ensuing from Figs. 6.4 and 6.5 microcalcification clusters can be quantitatively differentiated as ultra-fine, fine, pleomorphic and coarse textured, utilizing the correlation between mean $\bar{\mu}/\bar{\epsilon}$ -ratio and particle-surface distribution σ_r/σ (micromorphological descriptor)

circumstance that large calcium grains ($r \ge 275 \,\mu\text{m}$) occupy at least 0.25 % but not more then 0.75 % of the overall surface. Consistently, also within this group of microcalcifications a progression towards the inclusion of larger particles ($r \ge 425 \,\mu\text{m}$) with increasing $\bar{\mu}/\bar{\epsilon}$ -ratio (MC 11–12) was identifiable.

Coarse microtextures were observed for microcalcification clusters with $\bar{\mu}/\bar{\epsilon}$ -ratios exceeding a threshold of 0.6 (MC 13–15). A characteristic for this configuration is a small number of very large calcium structures dominating the overall microtexture appearance, i.e. accounting for more then 85 % of the overall surface, while small scatter-determining grains are negligible with respect to the occupied surface fraction. In accordance, the highest $\bar{\mu}/\bar{\epsilon}$ -ratio of 0.72 was observed for a structure (MC 15) consisting of a single, compact calcification only.

6.2.3 Microtexture of Microcalcifications as a Potential Indicator for Early Tissue Malignancy

In a very first approach, we tested the determined microtexture (ultra-fine, fine, pleomorphic or coarse) of microcalcifications as such as an indicator for tissue malignancy in early stages. This was done by comparing $\bar{\mu}$ versus $\bar{\epsilon}$ in a scatter plot for 11 microcalcifications associated histopathologically with a ductal carcinoma in-situ and 20 microcalcifications associated with a benign finding (Fig. 6.6a). The overall amount of investigated material corresponds to a microcalcified surface area of approximately 200 mm².

It is noticeable that benign microcalcifications dominate the region of $\bar{\mu}/\bar{\epsilon}$ -ratios determined for ultra-fine and fine micromorphologies, while the malignant microcalcifications prevail within ratios determined for pleomorphic and coarse microstructures. The frequency distributions of $\bar{\mu}/\bar{\epsilon}$ -ratios (range of 0.01 to 1.5) obtained for the corresponding benign and malignant microcalcifications (Fig. 6.6b), ascertain this impression. By relative comparison of the histograms, we found that only 12 % and 37 % of microcalcifications associated with ultra-fine and fine microstructure are of malignant nature while it is 68 and 69 % in case of polymorphic and coarse microtextures, respectively.

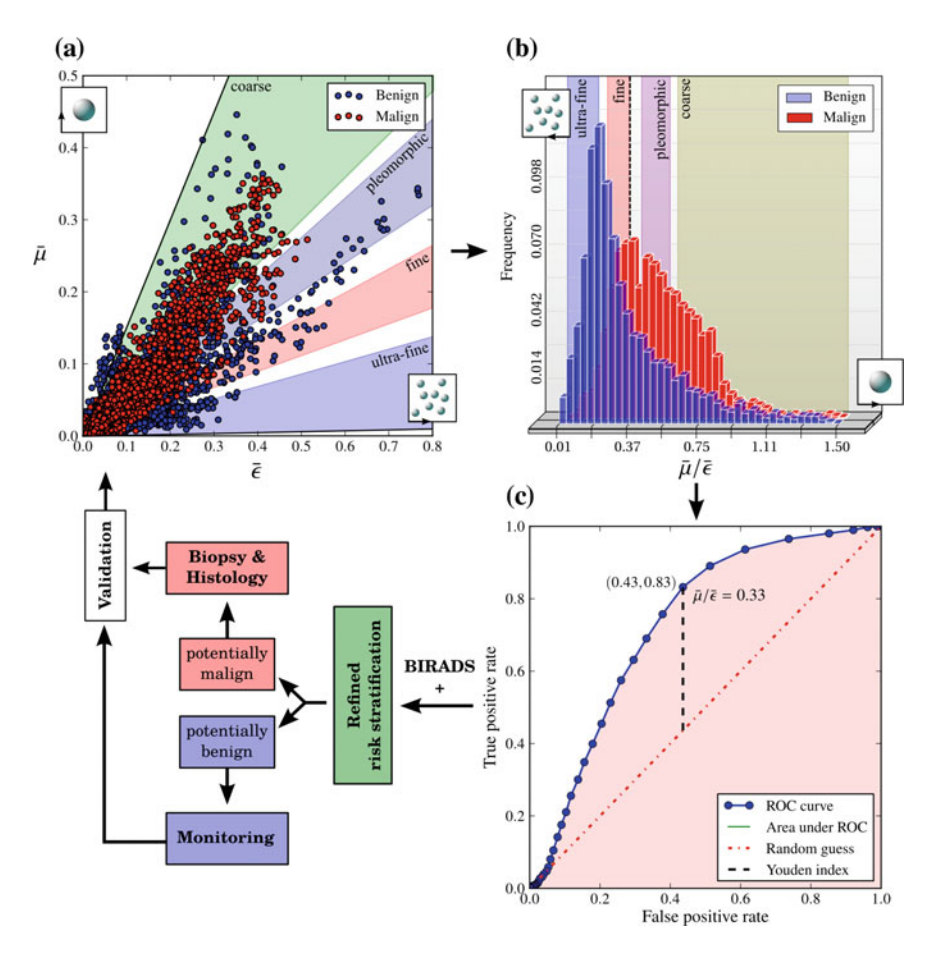


Fig. 6.6 Microtexture of microcalcifications as a potential indicator for early tissue malignancy. a Scatter plot comparing the absorption $\bar{\mu}$ to scattering power $\bar{\epsilon}$ of 11 microcalcifications associated histopathologically with a ductal carcinoma in-situ (red) and 20 microcalcifications associated with a benign finding (blue). b Histogram comparing the distribution of all $\bar{\mu}/\bar{\epsilon}$ -ratios found for benign and malignant microcalcifications obtained from a. Benign microcalcifications yield $\bar{\mu}/\bar{\epsilon}$ -ratios associated with ultra-fine and fine micromorphologies, while malignant microcalcifications prevail within ratios determined for pleomorphic and coarse microstructures. c Receiver operating characteristic curve estimating the performance of microtexture analysis as a potential indicator for early tissue malignancy, using a single $\bar{\mu}/\bar{\epsilon}$ -cut-off value. An optimal criterion (Youden index) for the discrimination of begin from malignant microcalcification was found for $\bar{\mu}/\bar{\epsilon} = 0.33$

In order to utilize this discriminability for diagnostics and estimate the performance of dark-field mammography as a predictor of malignancy, utilizing a single $\bar{\mu}/\bar{\epsilon}$ -cut-off value, a receiver operating characteristic was obtained [26]. The receiver operating characteristic curve (Fig. 6.6c) compares sensitivity (true positive rate) against 1-specificity (false positive rate) when classifying microcalcifications as

malignant if exceeding various $\bar{\mu}/\bar{\epsilon}$ -cut-off values. An optimal discrimination criterion (Youden index) was found for $\bar{\mu}/\bar{\epsilon}=0.33$ which surprisingly corresponds to the crossover of fine granular to pleomorphic microstructure. With a probability of 83 %, a malignant microcalcification will be correctly assigned as such, while 43 % of benign microcalcifications are falsely classified. We found that a malignant microcalcification may be graded with higher suspicion than a benign microcalcification utilizing its microtexture a probability of 73 % (area under the receiver operating characteristic curve), which is considered a fair test quality [27].

6.3 Conclusion | Microcalcification Assessment as a Diagnostically Promising Add-On Tool

In summary we have presented a novel, non-invasive and dose-equivalent method using X-ray dark-field mammography for breast microcalcification assessment that overcomes the major shortcomings of current microcalcification evaluation with conventional mammography: first, retrieval of microstructural properties proved to be fully-3D sensitive, hence not affected by projection-induced overlapping and superposition artefacts of microcalcification clusters in radiographic imaging mode. Second, microscopic resolution is provided through comparison of the global absorption to scattering power of microcalcification clusters, hence it is unrestricted by the resolution limit of the detector and therefore clinically compatible. Third, microcalcification analysis is quantitative and thus independent of the examining radiologist. A categorical differentiation of microcalcification clusters as ultra-fine, fine, pleomorphic and coarse microtextured was achieved by determining characteristic $\bar{\mu}/\bar{\epsilon}$ -ratios and revealing the particle-surface distribution σ_r/σ as a suitable micromorphological descriptor.

In a preliminary study investigating 31 biopsy samples the microtexture of microcalcifications was reviewed as a potential indicator for early tumor malignancy, considering that 85–95% cases of ductal carcinoma in-situ are detected due to their appearance in screening [1]. A fairly good correlation of ductal carcinoma in-situ with pleomorphic and coarse microstructures was reported in our study. Furthermore, we found that the crossover from fine to pleomorphic microstructure could be a potential indicator towards a higher probability of malignancy. Although literature currently does not provide a consistent framework for the validation and interpretation of our results (due to a very limited number of micro-CT studies available), we believe that with ongoing research microtexture analysis utilizing a single cut-off value could provide a differentiated reader-independent tool for risk stratification. Future applications in ductal carcinoma in-situ (DCIS) evaluation may include the determination of subtypes or evaluation of developing invasive breast cancer, currently impossible with conventional microcalcification evaluation, with the ultimate goal of addressing over-treatment of DCIS [28, 29].

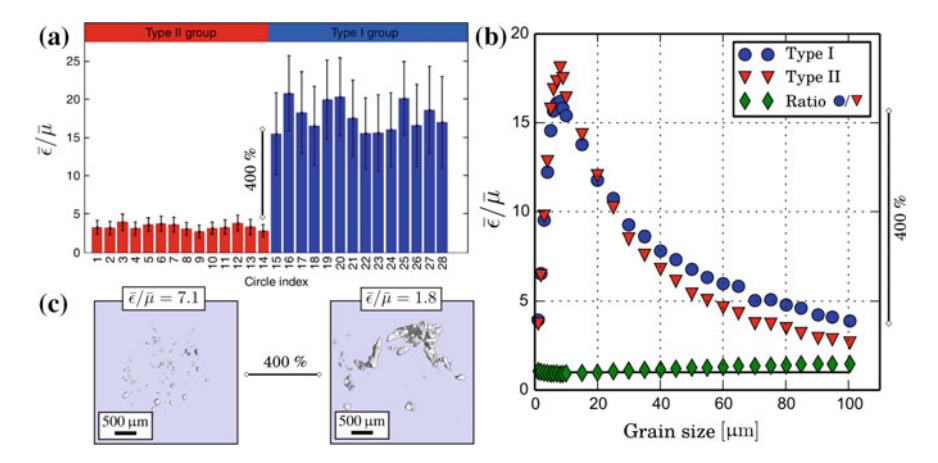


Fig. 6.7 Chemically-based differentiation of microcalcification via dark-field mammography? a Phantom study investigating potentially arbitrary powders, proposes a chemically-sensitive differentiation of Type I and II microcalcifications, contingent on variations in the exhibited $\bar{\epsilon}/\bar{\mu}$ -ratios of up to 400%. Supposition and figure adapted from Wang, Z. et al. (2014) [24]. **b** Simulations on the $\bar{\epsilon}/\bar{\mu}$ -ratio found for an assembly of type I and II grains with varying grain size and fixed overall volume. While the grain size is strongly impacting the $\bar{\epsilon}/\bar{\mu}$ -ratio, no significant chemical dependence was found, as illustrated by the *green diamonds* being nearly unity. **c** Experimental verification that the reported variations of 400%, can be solely explained by the microstructural properties of calcifications, which renders a chemically-based discrimination unjustified. Note that for reasons of consistency the $\bar{\epsilon}/\bar{\mu}$ - rather than the $\bar{\mu}/\bar{\epsilon}$ -ratio is displayed

In addition X-ray dark-field mammography could be of high interest for imaging of very small or low density calcifications. We found that ultra-fine micro-structures yielded an approximately 7 times higher signal in the dark-field in comparison to the absorption channel ($\bar{\mu}/\bar{\epsilon}=0.14$). This significant increase in dark-field and reduction of absorption contrast with decreasing calcium grain size, could enable the detection of incipiently growing microcalcifications in early tumor stages or dense breast tissue, which are currently overlooked in conventional mammography [30, 31].

Finally, our results strongly indicate that the micro-morphology of microcalcifications is the most prevailing factor in the determination of the $\bar{\mu}/\bar{\epsilon}$ -ratio of microcalcifications, which is in accordance with theoretical considerations on the generation of the dark-field imaging contrast [21, 22, 32]. First, we observed a change in the $\bar{\mu}/\bar{\epsilon}$ -ratio of more then 500 % from ultra-fine to coarse microtexture (cf. Figs. 6.4 and 6.5 MC 1 vs. MC 15). Second, minor structural deviations within one microtexture class, for example an increase in maximum grain size, were found to be consistent with a corresponding change in the mean $\bar{\mu}/\bar{\epsilon}$ -ratio (cf. Figs. 6.4 and 6.5 MC 1 vs. MC 3).

These insights dispute the main conclusion of a recent publication by Wang, Z. et al. (2014), namely the differentiation of calcium oxalate dehydrate (Type I) from calcium hydroxyapatite (Type II) breast calcification by measuring the $\bar{\mu}/\bar{\epsilon}$ -ratio [24].

In their study, the authors completely overlook the impact of microstructural properties on scatter-contrast generation and instead solely relate the $\bar{\mu}/\bar{\epsilon}$ -ratio of breast calcification to their chemical composition, on which the proposed diagnostic test is based on. Within their phantom study, they interpret discrepancies in the $\bar{\mu}/\bar{\epsilon}$ -ratio of about 400 %, which are very similar to the values presented here, to crystalline properties of type I and type II calcifications, while neglecting that the investigated powders comprise arbitrary grain sizes (Fig. 6.7a). Further, our simulation on dark-field imaging of type I and type II calcifications do not predict any significant differences in the exhibited $\bar{\mu}/\bar{\epsilon}$ -ratios (Fig. 6.7b), which is accordance with literature [33]. Hence, our results show on both a theoretical (Fig. 6.7b) and experimental basis (Fig. 6.7c), that the reported variations of 400 % can be solely explained by the microstructural constitution of the investigated microcalcification cluster. We are therefore convinced that a chemically-based discrimination of calcifications via dark-field radiography is purely hypothetical and unjustified. For a more detailed discussion see Appendix B.

Keypoints

- Sub-resolution dark-field mammography enables classification of microcalcifications as ultra-fine, fine, pleomorphic and coarse textured rather than giving a chemical grading.
- The microtexture of microcalcifications is a promising indicator for (early) tissue malignancy.
- The dark-field signal of ultra-fine calcifications strongly exceeds the corresponding absorption signal.

We suggest that the assessment of microcalcifications using dark-field mammography is suitable as a future in-situ application, since we could assign a cluster within native breast tissue as fine textured before undergoing excision and subsequently validating our prediction. In this proof-of-principle study, long exposure scans (9 phase-steps with 9 s exposure time each) were used, resulting in a mean glandular dose of 72 mGy per projection when measuring the cancerous mastectomy (for a detailed dose calculation cf. Sect. 5.4.2). Note that the measurements presented here were further conducted with the dose-unoptimized setup (for respective dose-compatible phase-contrast mammography cf. Chap. 7).

Nevertheless, together with other recently demonstrated advances of dark-field mammography in breast microcalcification imaging such as overall increased contrast-to-noise ratio and enhanced delineation, we believe that microtexture analysis will push grating-based mammography towards clinical application in the near future [34, 35]. Especially in the large group of uncertainly graded microcalcifications, microtexture analysis yields the potential to refine conventional, highly

subjective BIRADS classification and help to improve cancer risk stratification with the final goal of avoiding unnecessary and cost-intensive procedures.

6.4 Materials and Methods

6.4.1 Pool of Specimens

The freshly dissected, un-fixated breast specimen was obtained by mastectomy from a 63 year old patient. Histopathological work-up confirmed an invasive carcinoma. The specimen was measured in cradiocaudal orientation and was compressed to a medically reasonable thickness of 4.5 cm. The pool of 31 biopsies consisted of 11 microcalcifications hist-pathologically associated with in-situ carcinomas obtained from 10 patients and 20 microcalcifications hist-pathologically associated with benign finding from 13 patients. In order to avoid small-angle scatter from surface roughness, paraffin blocks were flattened before dark-field measurements.

6.4.2 Data Normalization

For the purpose of investigating microcalcifications independently from the underlying tissue in the beam direction, measured signals (T, V) were normalized with respect to the surrounding tissue (T_s, V_s) . Microcalcifications were discriminated from surrounding tissue, by thresholding and subsequent masking of the calcified areas within the dark-field image. On the supposition that the microcalcification cluster is distinctively thinner than the specimen $(d_c \ll d)$, the decrease of beam intensity (T_c) and fringe visibility (V_c) caused only by the microcalcification cluster can be retrieved by

$$T_c = \frac{T}{T_s}$$
 and $V_c = \frac{V}{V_s}$. (6.2)

6.4.3 Micro-CT Measurements

High resolution 3D-images were obtained with a micro-CT vtomex scanner (Phoenix X-ray, GE) tuned at $100\,\mu\text{A}$ and $60\,\text{kVp}$. Each paraffin block was measured at 1000 angles with 1 second exposure time per projection. An effective resolution of $6\,\mu\text{m}$ was achieved. 3D-volumes were reconstructed using the software VGStudio Max.

6.4.4 Voxel-Based Segmentation Algorithm

Micro-CT volume data was segmented by thresholding into two phases—microcalcification and enclosing paraffin—followed by a labelling process, which identifies clusters of interrelated voxels. This was achieved by calculating subvolumes of voxels, on the condition of at least sharing one mutual surface and considering sub-volumes greater than 5 voxels only. Afterwards, the volume and surface of each particle were interpolated and the particle radius calculated from a sphere of equivalent volume.

References

- 1. de Roos, M., van der Vegt, B., de Vries, J., Wesseling, J., & de Bock, G. (2007). Pathological and biological differences between screen-detected and interval ductal carcinoma in situ of the breast. *Annals of Surgical Oncology*, 14, 2097–2104.
- 2. Gajdos, C., et al. (2002). Mammographic appearance of nonpalpable breast cancer reflects pathologic characteristics. *Annals of Surgery*, 235, 246–251.
- 3. Farshid, G., Sullivan, T., Downey, P., Gill, P., & Pieterse, S. (2011). Independent predictors of breast malignancy in screen-detected microcalcifications: biopsy results in 2545 cases. *British Journal of Cancer*, 105, 1669–1675.
- 4. Palka, I., Ormandi, K., Gaal, S., Boda, K., & Kahan, Z. (2007). Casting-type calcifications on the mammogram suggest a higher probability of early relapse and death among high-risk breast cancer patients. *Acta Oncologica*, 46, 1178–1183.
- 5. Yunus, M., Ahmed, N., Masroor, I., & Yaqoob, J. (2004). Mammographic criteria for determining the diagnostic value of microcalcifications in the detection of early breast cancer. *Journal of Pakistan Medical Association*, 54, 24–29.
- Bent, C., Bassett, L., D'Orsi, C., & Sayre, J. (2010). The positive predictive value of BIRADS microcalcification descriptors and final assessment categories. *American Journal* of Roentgenology, 194, 1378–1383.
- 7. Liberman, L., & Menell, J. (2002). Breast imaging reporting and data system (BIRADS). *Radiologic Clinics of North America*, 40, 409–430.
- 8. Masmroor, I. (2008). Effectiveness of assigning BIRADS category-3 to breast lesion with respect to follow-up. *Journal of the College of Physicians and Surgeons Pakistan*, 18, 209–212.
- Nalawade, Y. (2009). Evaluation of breast calcifications. *Indian Journal of Radiology and Imaging*, 19, 282–286.
- Purdie, C., & McLean, D. (2009). Benign microcalcification and its differential diagnosis in breast screening. *Diagnostic Histopathology*, 15, 382–394.
- 11. Berg, W., Arnoldus, C., Teferra, E., & Bhargavan, M. (2007). Biopsy of amorphous breast calcifications: pathologic outcome and yield at stereotactic biopsy. *Radiology*, 221, 495–503.
- Uematsu, T., Kasami, M., & Yuen, S. (2008). Usefulness and limitations of the Japan mammography guidelines for the categorization of microcalcifications. *Breast Cancer*, 15, 291–297.
- 13. Smith, A. (2003). Fundamentals of digital mammography: physics, technology and practical considerations. *Radiology Management*, 25, 18–24.
- 14. Willekens, I., et al. (2014). High-resolution 3D micro-CT imaging of breast microcalcifications: a preliminary analysis. *BMC Cancer*, *14*, 9.
- 15. Gufler, H., Wagner, S., & Franke, F. (2011). The interior structure of breast microcalcifications assessed with micro computed tomography. *Acta Radiology*, *52*, 592–596.

References 93

16. Imamura, K., et al. (2008). Microcalcifications of breast tissue: appearance on synchrotron radiation imaging with 6-μm resolution Am. *Journal of Roentgenology*, 190, 234–236.

- 17. Langen, H., et al. (2012). Microradiography of microcalcifications in breast specimen: a new histological correlation procedure and the effect of improved resolution on diagnostic validity. *Radiology Research and Practice*, 2012, e526293.
- 18. Pfeiffer, F., et al. (2006). Phase retrieval and differential phase-contrast imaging with low-brilliance X-ray sources. *Nature Physics*, 2, 258–261.
- Momose, A., et al. (2003). Demonstration of X-ray talbot interferometry. *Japanese Journal of Applied Physics*, 42, 866–868.
- 20. Pfeiffer, F., et al. (2008). Hard-X-ray dark-field imaging using a grating interferometer. *Nature Materials*, 7, 134–137.
- 21. Yashiro, W., Terui, Y., Kawabata, K., & Momose, A. (2010). On the origin of visibility contrast in X-ray Talbot interferometry. *Optics Express*, *18*, 16890–16901.
- 22. Malecki, A., et al. (2012). Quantitative wave-optical numerical analysis of the dark-field signal in grating-based X-ray interferometry. *Europhysics Letters*, 99, 48001.
- Schleede, S., et al. (2012). Emphysema diagnosis using X-ray dark-field imaging at a laserdriven compact synchrotron light source. PNAS, 109, 17880–17885.
- 24. Wang, A., et al. (2014). Non-invasive classification of microcalcifications with phase-contrast X-ray mammography. *Natural Communication*, *5*, 3797.
- Bech, M., et al. (2010). Quantitative X-ray dark-field computed tomography. *Physics in Medicine and Biology*, 55, 5529–5539.
- 26. Metz, C. (2012). Basic principles of ROC analysis. Seminars in Nuclear Medicine, 8, 283–298.
- Zhou, X., Obuchowski, N., & McClish, D. (2011). Statistical methods in diagnostic medicine. Hoboken: Wiley.
- Stomper, P., & Connolly, J. (1992). Ductal carcinoma in situ of the breast: correlation between mammographic calcification and tumor subtype. *American Journal of Roentgenology*, 159, 483–485.
- 29. Burstein, H., et al. (1992). Ductal carcinoma in situ of the breast New. *The NewEngland Journal of Medicine*, 350, 1430–1441.
- Sickles, E. (1984). Mammographic features of "early" breast cancer Am. *Journal of Roentgenology*, 143, 461–464.
- 31. Martin, J., Moskowitz, M., & Milbrath, J. (1979). Breast cancer missed by mammography. *American Journal of Roentgenology*, 132, 737–739.
- 32. Lynch, S., et al. (2011). Interpretation of dark-field contrast and particle-size selectivity in grating interferometers. *Applied Optics*, 50, 4310–4319.
- 33. Michel, T., et al. (2013). On a dark-field signal generated by micrometer-sized calcifications in phase-contrast mammography. *Physics in Medicine and Biology*, 58, 2713.
- 34. Stampanoni, M., et al. (2011). The first analysis and clinical evaluation of native breast tissue using differential phase-contrast mammography Invest. *Radiology*, 46, 801–806.
- 35. Hauser, N., et al. (2014). A study on mastectomy samples to evaluate breast imaging quality and potential clinical relevance of differential phase contrast mammography. *Investigative Radiology*, 49, 131–137.

Chapter 7 Toward Clinically Compatible Phase-Contrast Mammography

I have wanted to fly into space for many years, but never imagined it would really be feasible.

Stephen Hawking

Abstract This chapter is dedicated to the clinical compatibility of laboratory-based phase-contrast mammography. First, we present which hardware changes and optimizations were conducted throughout the duration of this thesis, which enabled the first dose-compatible and rapid scan time phase-contrast mammograms of a freshly dissected mastectomy. In a next step, we quantitatively verify that the absorption mammograms obtained from the phase-contrast mammography unit meet the imaging criteria set by the American College of Radiology. Further, this chapter elaborates on the adaptation of tomosynthesis—which is nowadays common practice in clinical routine—towards phase-contrast and scatter-sensitive imaging. Note that some of the here presented results have been published as "Scherer, K. et al. Toward clinically compatible phase-contrast mammography. PLoS One 10, e0130776 (2015)". Finally, this chapter concludes with a possible solution on how to present trimodal data in a comprehensive manner. The utilized fusion algorithm is provided by E. Coello (GE Global Research, Munich), was developed in collaboration with the TUM, and is based on the publications "Coello, E. Image fusion in X-Ray phase contrast imaging (Technische Universität München, Munich, 2014)".

7.1 Motivation | Status Quo of Phase-Contrast Mammography

With the introduction of a three-grating Talbot–Lau interferometer using structured gratings, phase-contrast imaging is no longer restricted to highly brilliant X-ray sources, but instead is compatible with conventional laboratory sources, so that great potential for clinical applications is envisioned [1]. Especially in the case of mammography, recent studies verified diagnostic advantages for certain mammographic

indications, when utilizing phase- and scatter-sensitive imaging [2-5]. However, a major shortcoming of all previous studies on laboratory phase-contrast mammography was that the underlying image acquisition parameters did not meet clinical standards with respect to radiation dose, scan time and consistency between subsequent measurements. As shown in Chap. 5, we could obtain comprehensive phase-contrast mammograms of fresh, un-fixated and cancerous mastectomy samples at medically reasonable sample compression using a compact setup (total length of 1.5 m, rotating X-ray anode, flat panel X-ray detector with $127 \times 127 \,\mu\text{m}^2$ pixel size, effective pixel size of $85 \times 85 \,\mu \text{m}^2$ —similar in its design to a conventional mammography systems). However, the applied radiation doses (MGD) of 66–72 mGy per measurement by far exceeded the dose limits of 2.5 mGy, set by the European guidelines for Ouality assurance in mammography [6]. Respectively, also the exposure times used for this initial proof-of-principle studies amounted to more than one minute, incompatible with clinical routine and patient care. Similar limitations (MGD of 26 mGy, exposure time of 72s) have been reported by other groups working on the field of grating-based phase-contrast mammography [3, 4].

Therefore, difficulties arise which strongly restrict the further progression of phase-contrast mammography towards clinical implementation. First, high-dose measurements may not be reproducible within a dose-compatible scenario, which weakens the diagnostic significance and transferability of current study outcomes. Second, the analyzed sample collective is limited to a small number of ex-vivo mastectomy samples comprising medical indications which may not be representative for daily screening. Additionally, mastectomy samples are mostly obtained from elderly patients with fully adipose breasts, which are sufficiently well assessed with conventional mammography. Hence render the initial situation of phase-contrast mammography unfavourable with respect to a potential diagnostic surplus-value. Abladates further comprise resection borders and liquid inclusions, which are naturally absent within an in-vivo setting, however may falsify the evaluation of artefact-afflicted differential phase and dark-field data in comparison to respective absorption data. Finally, small study cohorts can not reliable model the amount of potential over-diagnosis accompanied by phase- and scatter-sensitive imaging.

While the complementarity of the three signals is the essence of phase-contrast mammography, it involves a set of issues with respect to clinical routine and human resources. First of all, radiologist are used to the "low-frequency nature" of the absorption image and are inexperienced with reading and correctly interpreting the novel image modalities, which mostly concerns the differential data. Second, the trimodal image sets require a tripling of examination time impracticable within screening routine. With the goal of extracting a single mammogram only, which preserves the "absorption character" of conventional mammograms while utilizing the multimodality of phase-contrast imaging, several fusion algorithms have been proposed recently [7, 8]. The latter mostly rely on a multi-resolution framework, which essentially decomposes the input images in specific frequency bands via discrete wavelet decomposition, followed by a subsequent de-noising, contrast-enhancing and recombining, respectively. Major drawback of this approach is the fact that the number of retrieved frequency domains is limited and that only one, constant weighting factor

is assigned to each domain. Further, on the assumption of maximizing the signal-to-noise ratio, by which each frequency band is optimized, the setting possibilities on the part of the radiologists are limited. This is yet unfavourable, since there is only little knowledge which breast features will benefit from which image modality and frequency domain. To overcome this limitation we propose a fusion approach in Fourier-space, which enables a more specific—on the fly—tuning, additionally granting access to the full range of frequencies.

7.2 Results

7.2.1 Setup Optimization

Several software and hardware specifications of the dedicated phase-contrast mammography system were optimized in order to enable clinically compatible measurements. The original entities underlying the previous high-dose measurements as presented in Chap. 5, are stated in parenthesis for comparison.

First, the arrangement of the breast-tissue holder and the phase grating downstream of the X-ray beam were exchanged (Fig. 3.1a). Thus, a saving of approximately 33 % mean glandular dose was achieved (value corresponds to a sample compression of 4 cm), by utilizing the wafer-substrate (silicon) as an effective absorber of low energy photons and increasing the source-to-sample distance. Note that this optimization step did only alter the effective pixel-size, not the overall photon statistics, while only slightly decreasing the sensitivity of the interferometer [9].

Second, a revised Varian 2520-DX detector (Gadox-screen) with improved read out electronics and a 16-bit AD-converter was implemented as an integrating flatpanel detector. Since the two absorber gratings reduce the total photon flux by at least 75%, the internal readout speed of the detector was strongly decreased to compensate for low photon statistics and reduce the accumulation of internal readout-noise during a single exposure. Correspondingly the factory setting of 10 fps (frames per second) was reduced to 1 fps and synchronized with the total exposure time of 1 (9) second(s) per phase-step. To further decrease radiation dose and scan time, the number of phase-steps was decreased to 5 (9)—at which sufficient sampling of the phase-stepping curve is still practicable—resulting in a total exposure time of only 5 (81) seconds per measurement.

By tuning the acceleration speed and step size of the high-load actuator, which translates the phase grating by means of a nano-converter, the scan time for the total 5 phase-steps was lowered to $12\,(101)\,\mathrm{s}$ in total. Furthermore, the substrate thickness of the analyser grating was thinned down to $200\,(500)\,\mu\mathrm{m}$, in order to minimize the attenuation of dose-relevant photons.

Finally, a stack of Polymethylmethacrylat-plates (PMMA) of variable thickness was introduced into the flat-field measurement as a breast-equivalent absorber (Fig. 3.1b). Here, the breast equivalent serves multiple purposes: first, a saturation of

the detector during flat-field measurements at low frame-rates is prevented. Second, the breast and respective reference scan exhibit comparable X-ray imaging spectra. As a consequence shadowing artefacts appearing at the edges of the absorption gratings are eliminated; hence flat image backgrounds within the absorption and dark-field channel are provided, which strongly facilitate the depiction of fine and low-contrast features. Further, variations in the overall fringe visibility due to beamhardening effects are avoided, preventing the generation of an artificial dark-field signal. Hence, by adapting the PMMA thickness so that the absorption power of the respective breast sample is mimicked for a certain effective energy, quantitativeness of each image signal is provided and therewith comparability between different breast samples established. Figure 7.1 demonstrates the necessity of implementing a respective breast-equivalent absorber. In Table 7.1 a conversion table from breast tissue (50% glandular and 50% adipose) to respective PMMA is given, for certain mean energies.

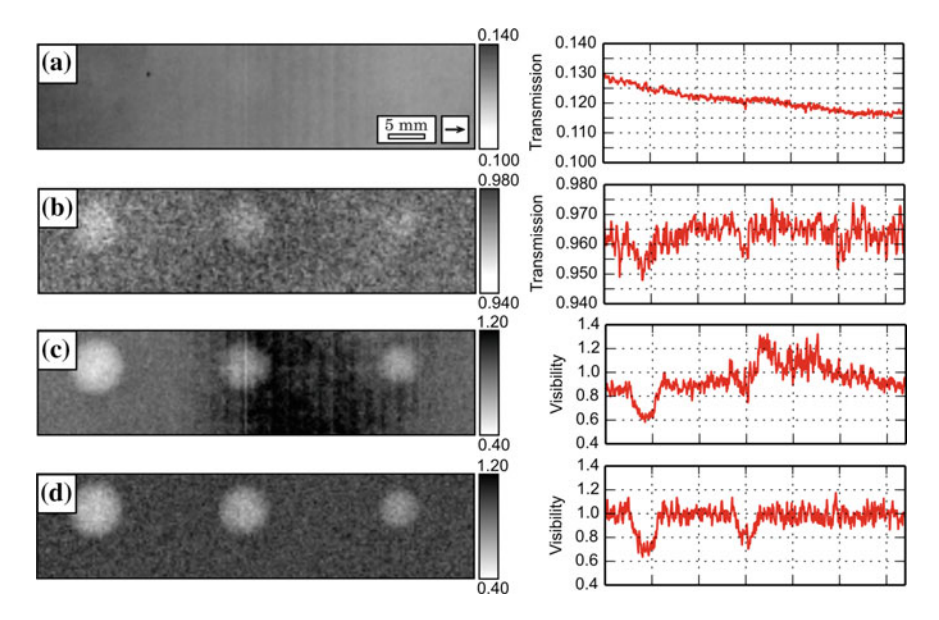


Fig. 7.1 Influence of a breast-equivalent absorber on image quality and quantitativeness in phase-contrast mammography. Grating-based absorption mammogram, obtained without (a) and with a breast-equivalent absorber (b). Due to an inclined position of the analyser grating with respect to the beam, the X-ray spectrum is hardened towards the left side. This results in a non-linear attenuation of photons through the phantom and generation of an artificial ramp as present in a. By using an absorber equivalent, the flat-field and sample scan yield similar X-ray spectra, which enables the retrieval of a flat mammogram as shown in b. Thereby, the depiction of the three tumor masses is strongly improved. Grating-based dark-field mammogram, obtained without (c) and with a breast-equivalent absorber (d). The non-linear absorption of photons and the circumstance that the fringe visibility is spectrum dependent, result in the generation of an artificial (physically unplausible) scatter signal ranging in between 0.8 and 1.2, as shown in c. By comparison in d, the flat-field and sample scan exhibit the same fringe visibility. As expected the breast phantom matrix is non-scattering, since yielding a visibility value of 1. Corresponding line-plots on the right

Table 7.1	Conversion tak	le hetween hred	ast tissue and no	lymethylmethacrylat

Energy (keV)	23	25	27	29	31	33
Conversion factor $\left[\frac{\mu_{\text{Breast}}}{\mu_{\text{PMMA}}}\right]$	0.924	0.902	0.895	0.890	0.885	0.881

By multiplying the breast specimen thickness with a conversion factor, the dimensions of an appropriate breast-equivalent absorber (PMMA) can be calculated. Note that the linear attenuation coefficients μ_{Breast} and μ_{PMMA} , which determine the conversion factors, are energy dependent

7.2.2 Experimental Verification

Figure 7.2 shows the experimental absorption (a), differential phase (b) and dark-field radiograms (c) of a freshly dissected, ex-vivo breast mastectomy sample, obtained at the laboratory X-ray phase-contrast mammograph alongside with the corresponding clinical, ex-vivo mammogram (d) taken with a Hologic, Selenia Dimensions mammograph (Bedford, USA—pixel size of $70 \times 70 \,\mu\text{m}^2$). The specimen was compressed to a thickness of 3.8 cm which corresponds to the clinical setting of a small breast. With a corresponding g-factor of 0.371 and a total exposure time of 5 s, the mean glandular dose was determined to 2.2 mGy, which is approximately twice the dose of the respective conventional mammogram of 0.94 mGy, but below the guideline limit of 2.5 mGy [6]. Two experienced radiologists rated the conventional and grating-based absorption images as equivalent with respect to image quality, acutance, sharpness and depiction of tissue strands/microcalcifications. We conducted exemplary contrast-to-noise ratio (CNR) investigations within the cancerous and microcalcification bearing tissue volume (white framed inlay). We found that the dark-field channel yields a superior CNR of 10.6 in the detection of the microcalcified tissue in comparison to 5.7 in the case of the absorption channel, proving that scatter-sensitive imaging provides beneficial information, even within a dedicated low-dose setting. Besides, soft-tissue tumor compartments, comprising highly dispersed grains are exclusively detected within the dark-field channel as indicated by a blue arrow. Finally, the grating-based images were manually fused by an expert using a Fourier Domain approach, as described in Sect. 7.4.4. Figure 7.2e shows the corresponding fused mammogram, which comprises all diagnostically important image contents at a glance: the distribution of fatty and glandular tissue, a superior depiction of high-frequency tissue strand (red arrows) as well as a superior detection quality of the micro-calcified, tumorous tissue (red and black arrows). Histological work-up of the mastectomy sample proved a residual (after neoadjuvant chemotherapy) breast cancer of non-specific type (NST) with a diameter of $11.5 \times 8.5 \times 2 \text{ cm}^3$ as well as residual ductal carcinoma in-situ containing intraluminal calcifications.

To ensure that low-dose, grating-based mammography meets the standards of clinical image quality, a mammographic accreditation phantom (Gammex 156, Gammex Inc., Middleton $-4.2\,\mathrm{cm}$ compressed human breast, $50\,\%$ adipose and $50\,\%$ glandular tissue) was measured with the clinically compatible acquisition protocol (5 s exposure, $12\,\mathrm{s}$ scan time, MGD of $2.07\,\mathrm{mGy}$). The respective absorption image (Fig. 7.3b) even exceeds the criteria set by the State Departments of Radiologic Health and the

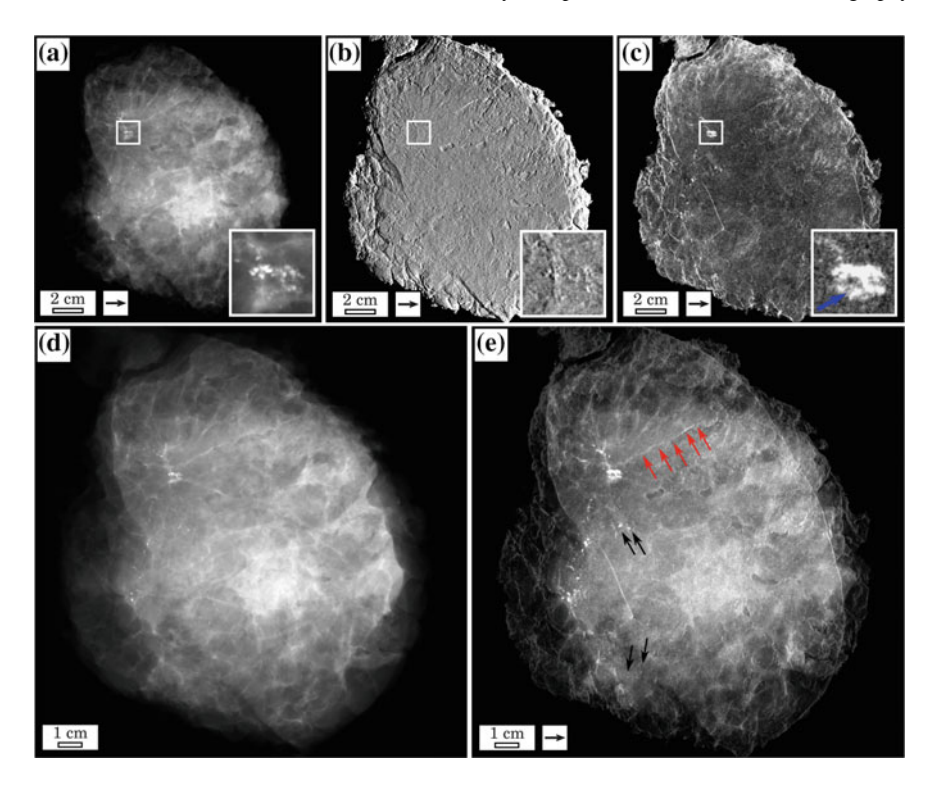


Fig. 7.2 Clinically compatible phase-contrast mammography of a freshly dissected, cancerous mastectomy sample. Grating-based absorption (a), differential phase (b), dark-field mammography (c) at 40 kVp, 70 mA and MGD of 2.2 mGy and clinical, ex-vivo mammogram (d) at 28 kVp, 86 mAs and 0.94 mGy mean glandular dose (Rhodium filter) of a freshly dissected mastectomy sample. Both absorption images are rated equivalent with respect to image and detection quality. *Inlays* show magnified view of the cancerous and micro-calcified tissue volume, with a superior contrast-to-noise ratio in the dark-field (10.6) in comparison to absorption channel (5.7). Micro-calcified, soft-tissue compartments of the tumor are exclusively detected with in the dark-field channel as indicated by *blue arrow*. **e** Expert-tuned fusion of the trimodal data shown in **a-c**. Note that the fused image depicts density variations in similar quality as the clinical, ex-vivo mammogram, additionally providing a superior depiction of high-frequency breast features (*red arrows*), the tumor core and widespread calcium grains (*black arrows*)

ACR, by revealing 4 of a minimum of 4 fibrils, 3 of a minimum of 3 groups of simulated microcalcifications and 4 of a minimum of 3 tumor masses [10]. Besides, the differential phase (c) and dark-field images (d) enable the detection of a 5th fibril and a 5th tumor mass, as indicated by arrows, unseen within the experimental absorption channel. Although the Gammex 156 can only reliably model the absorption behaviour of breast features, the depiction of additional structures, proves complementarity of the three image modalities and shows that the strongly decreased number of phase steps and exposure time are still sufficiently high for a meaningful retrieval of (differential) phase and scatter signal.

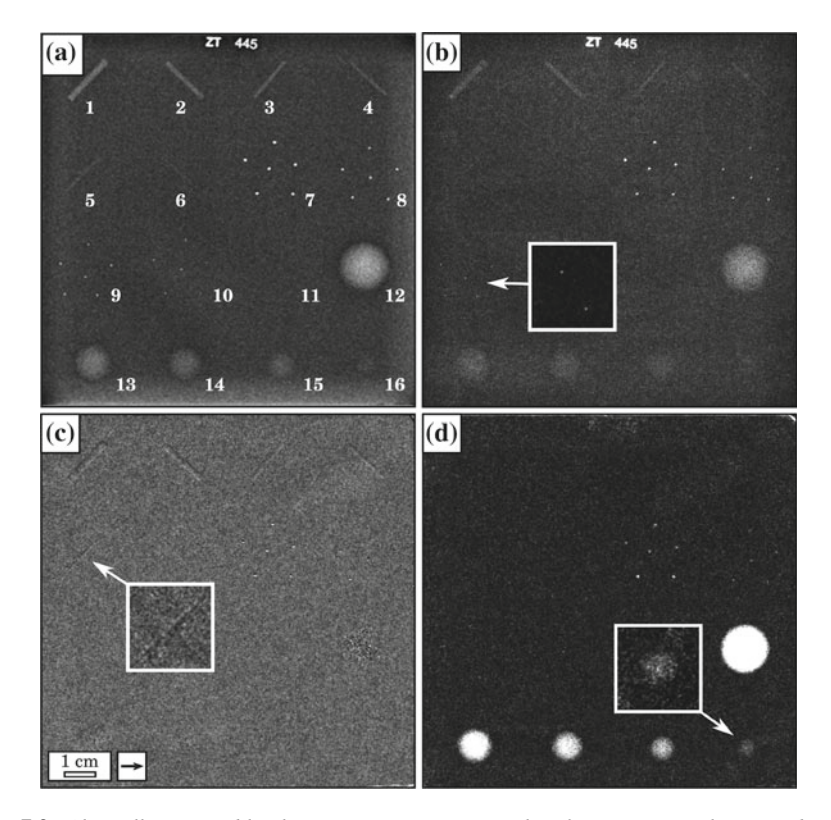


Fig. 7.3 Clinically compatible phase-contrast mammography of a mammographic accreditation phantom. Clinical mammography at 28 kVp, 159 mAs and 1.62 mGy mean glandular dose (Rhodium filter) (a), grating-based absorption (b), differential phase (d) and dark-field mammogram (d) at 40 kVp, 70 mA and 2.07 mGy mean glandular dose of the mammographic accreditation phantom Gammex 156 (Gammex Inc., Middleton). The grating-based absorption image meets the standard criteria of clinical image quality set by the ACR, by resolving 4 of a minimum of 4 fibrils (#1–4), 3 of a minimum of 3 groups of simulated microcalcifications (#7–9) and 4 of a minimum of 3 tumor masses (#12–15). The differential phase and dark-field channel provide meaningful, complementary information by revealing an additional 5th fibril (#5) and 5th tumor mass (#16) as indicated by arrows

7.2.3 Dark-Field Tomosynthesis

In the last years tomosynthesis enjoyed an unparalleled success story in the field of novel breast imaging techniques. Recent studies clearly showed that tomosynthesis is outperforming conventional full-field mammography. Skaane, P. et al. investigated more than 12,000 examinations and found, that tomosynthesis results in an 27% increase in the detection rate of invasive and in-situ carcinomas, while also decreasing the rate of false-positive diagnoses by 15% [11]. Especially in the group of woman being younger than 40, the combination of tomosynthesis and conventional digital mammography showed a superior reduction of recall rates by more than 50%, in

comparison to digital mammography alone [12]. In the case of entirely fatty breast tissue the advantage of tomosynthesis over conventional mammography is considered as rather insignificant.

The distinct gain in diagnostic performance in the assessment of dense breast tissue is attributed to the fact that tomosynthesis provides a depth resolution in beam direction, which tackles so-called "anatomical noise" present in radiography. First, full-field mammography suffers from summation effects of breast structures in dense tissue, which lead to the generation of artificial masses, coming with a high risk of being graded as malignant. In conventional mammography various techniques exist, which try to address superposition artefacts, however require additional unfavourable efforts, such as a twisting of the breast in combination with multiple exposures in cranialcaudal and mediolateral oblique projections [13]. Second tumor detection heavily relies on the revelation of tumor delineations, microcalcifications and architectural disorders, which can be superimposed and therefore hidden within scattered fibroglandular or heterogeneously dense breast tissue. Finally, tomosynthesis allows a precise localization of microcalcifications and masses in the breast, facilitating the planning and execution of invasive follow-up procedures.

Typically, tomosynthesis is operated in a angular range of 10–20° with 10–20 projections taken at small 1° steps, to provide a high spatial resolution in-plane [14]. The optimal trade-off between angular range and step size, which determines the quality of depth to in-plane resolution is still under investigation. Note that contingent on a limited angular sampling, tomosynthesis does not offer an isotropic volume or quantitative Hounsfield units as in comparison with computer tomography. While tomosynthesis is nowadays routinely operated within clinics, only little effort was conducted to adapt this technology for phase-contrast imaging. Previous studies investigated either phantoms or thin, formalin fixated slices of breast tissue and were mostly restricted to highly brilliant X-ray sources [15–17].

In order to illustrate the potential of phase-sensitive tomosynthesis at a compact setup a lizard was investigated in first place. Figure 7.4a–c show a set of reconstructed absorption, phase and dark-field in-plane slices which are ascending the animal body, respectively. The first column shows a plane close to the tissue surface. Here the phase image provides a superior depiction of the scales as indicated by the red box, contingent on the fact that the points of contact between the scales yield a distinct change in local refractive index. The second column shows the inner compartments of the corpus, including organs and rips. Here, the dark-field provides an extraordinary good depiction of liver and gastric, potentially due to a desiccation of the inner tissue through formalin, as indicated by the blue box. The third column shows the backbone, which is equally well resolved within all three image modalities.

In a next step, a fresh breast abladate at a medically reasonable sample compression of 4.7 cm was investigated with tomosynthesis. Figure 7.5a, b show the absorption and dark-field (cumulative) projections of a selected image section of the breast. Here, anatomical noise renders two tiny microcalcifications hardly visible (black circles), since being overlapped by dense breast tissue as well as scattering vessels. In Fig. 7.5c, d the reconstructed in-plane slices, which comprise the calcifications are displayed in absorption dark-field, respectively. Here, the microcalcifications are

103

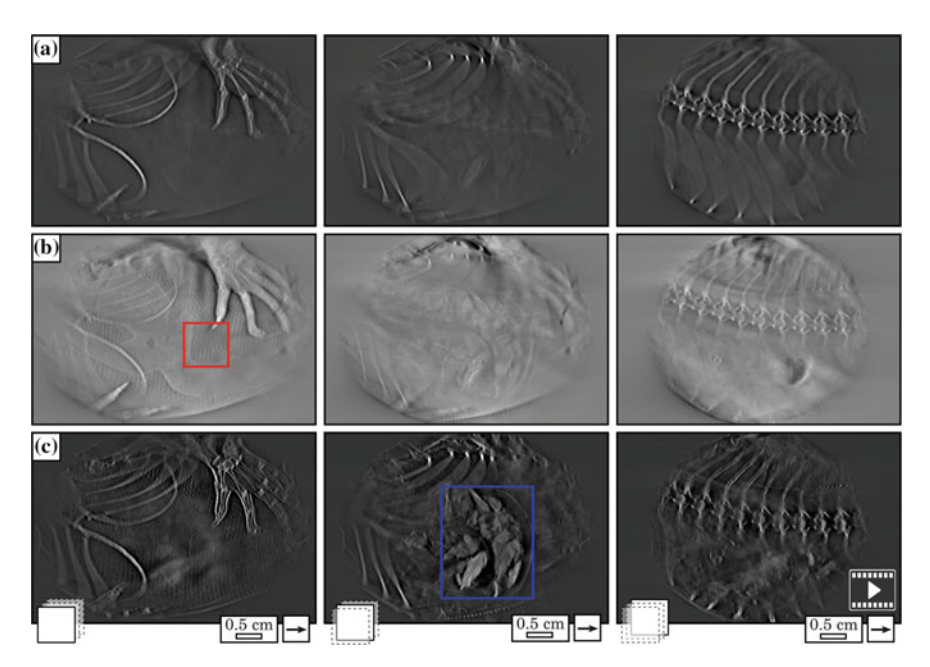


Fig. 7.4 Phase-contrast tomosynthesis of a lizard. Reconstructed absorption (a), phase (b) and dark-field (c) in-plane slices of a lizard, enabling depth resolution throughout the animal corpus (angular range: -20° to 20° , angular step size: 1°). The phase image provides a superior depiction of the skin scales (red box), contingent on prominent electron density variations in regions connecting adjacent scales. Liver and gastric are best resolved in the dark-field channel (blue box), reasoned by a potential hardening of tissue due to formalin uptake. The optical dense backbone is equally well resolved in all three modalities. Arrows indicate one-directional measurements. Stacks indicate depth of the in-plane slice. For a respective tomosynthesis rendering find Fig. A.2

clearly delineated from the background and revealed as being incorporated within a blood vessel. This information diagnoses the latter as vascular calcifications yielding a benign, non-cancerous origin, which would not require further procedures within a clinical examination. Note that this information is not accessible by means of the radiographies. Further, the dark-field channel is capable of resolving an additional small vessel perfusing the breast tissue yet hardly detectable within the absorption channel. When comparing the respective contrasts in ascending slices, we see that also in the case of tomosynthesis scatter-sensitive imaging provides complementary information: the absorption image excels at the depiction of larger vessel and tissue density variations, while the dark-field channel provides exceptionally good discrimination of fine vessels from surrounding, non-scattering tissue.

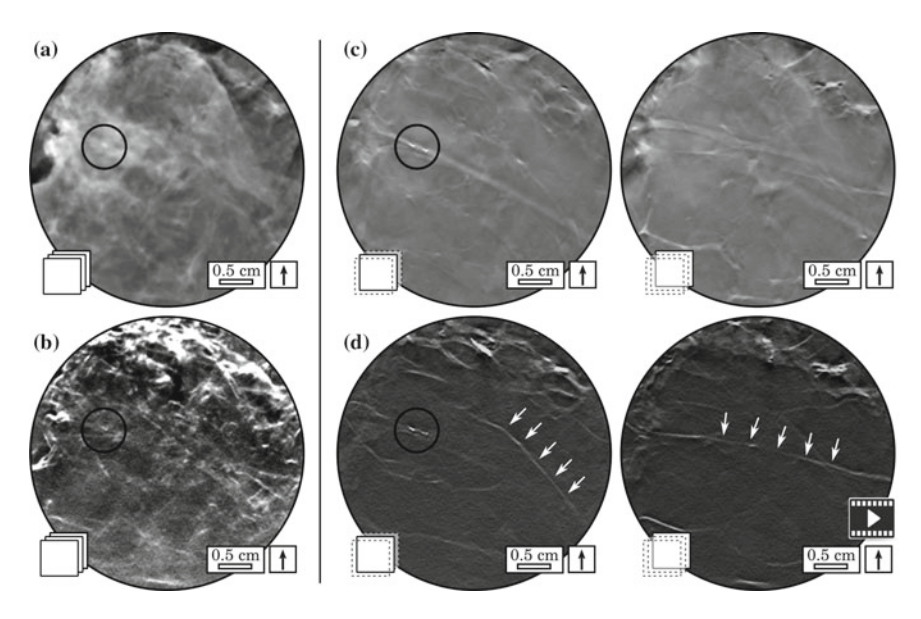


Fig. 7.5 Dark-field tomosynthesis of a freshly dissected abladate provides complementary depth information. **a** Absorption and **b** dark-field (cumulative) projection of a selected breast section, with microcalcifications (black circles) being superimposed by dense breast tissue and scattering vessels. **c** Two reconstructed, in-plane absorption and **d** dark-field slices, reveal the calcifications as benign being incorporated within a vessel (angular range: -20° to 20° , angular step size: 1°). Note that the dark-field channel provides an exceptional good discrimination between small vessels (white arrows) and non-scattering, surrounding tissue which are yet hardly detectable within the absorption channel. Arrows indicate one-directional measurements. Stacks indicate depth of the in-plane slice. A respective tomosynthesis rendering of a second case study can be found Fig. A.3

7.3 Conclusion | Phase-Contrast Mammography Adaptable to Clinical Requirements

In this technical developments chapter, we have shown for the very first time that phase-contrast mammography using a compact laboratory setup can be conducted in a clinically compatible manner. Our results demonstrate that the obtained absorption image is equivalent to standard mammography, while providing two additional complementary image modalities by means of phase and dark-field image contrast. The overall scan time could be decreased to 12 s which lies between the typical scan times of 7–20 s reported for current tomosynthesis systems. Considering that state-of-the-art systems utilize X-ray anodes with a power output of up to 7 kW (200 mA, 35 kV), while the X-ray anode underlying the presented work was capped at 2.8 kW (70 mA, 40 kV), suggests that an additional reduction of exposure time and detector noise is practicable. Within a clinical setting the mean glandular dose of 2.2 mGy could be even further decreased, using ultra-thin titan-wafers as substrate for the detector grating and increasing the interferometer fringe visibility, which is

currently only at 18%. Finally, we implemented an adaptable breast equivalent which allows the retrieval of artefact-free and quantitative images, hence providing comparability between subsequent breast measurements, indispensable for the diagnostic significance of future reader-studies.

To provide comparability between the clinical and experimental absorption images, the breast abladate was measured with an approximately doubled radiation dose in comparison to the conventional mammogram, contingent on the fact that 50% of all dose-relevant photons are attenuated by the analyser grating. Here the use of harder X-rays could facilitate a reduction of imaging dose, considering that phase-sensitive imaging offers strongly enhanced CNRs (in comparison to conventional absorption-based imaging) even at high energies [18, 19]. Further, an optimal combination of the complementary, multi-modal data may provide depiction of diagnostically crucial image content at much decreased imaging doses [20]. Finally, note that the clinical absorption image (Fig. 7.3a) is excelling the corresponding grating-based mammogram (Fig. 7.3b), with respect to the depiction of the ultra-fine phantom structures #5, #6 and #10. However, a slightly inferior spatial resolution of the experimental versus clinical scanner is understandable, when comparing underlying parameters: indirect X-ray conversion panel (Gadox) versus direct X-ray conversion panel (amorphous selenium), one-dimensional anti-scattergrid versus two-dimensional anti-scatter-grid, large focal spot (0.3 mm) versus small focal spot (0.05–0.2 mm) [21].

We further incorporated an intuitive fusion scheme for the comprehensive presentation of trimodal data at a glance, which is similar in appearance to the conventional absorption image and thus can be read by every radiologist. While a manually-tuned fusion is time-consuming and unsuitable for a clinical implementation, it is currently inevitable for the generation of a data pool of ground-truth examinations. These enable the benchmark of automatic fusion approaches, utilizing a "fusion factor/symmetry", which maximizes the amount of information being transferred from the input to the fused image.

Keypoints

- Phase-contrast mammography fulfils the criteria set by the ACR.
- Phase-contrast mammography meets requirements with respect to clinical acquisition parameters.
- Dark-field tomosynthesis provides complementary depth resolution.

Finally, the first phase-contrast tomosynthesis concept study investigating fresh breast abladates was conducted. Here we could show that the dark-field image provides complementary information, which enable a superior discrimination of vessels and inherent calcifications from surrounding tissue. Since this study was conducted as a proof-of-principle investigation, much space is given for improvements. First to reduce ring artefacts arising from noisy detector pixels a median-filter was applied to the projections prior to reconstruction, which however decreases the effective image

resolution. This step is avoidable when using a "type-writer"-scan procedure, i.e. the specimen is locally shifted by the size of a pixel each time before being rotated. Second, a conventional filtered-back projection was used, which however is unfavourable for the reconstruction of angular-incomplete datasets leading to under-sampling artefacts. Here iterative algorithms using the expectation maximization could strongly increase the image quality [22]. Besides, we utilized a stop-and-go image acquisition technique amounting to long scan times of several minutes, i.e. the sample is rotated each time after a full phase-stepping is obtained. However, recently Xi, Y. et al. proposed that interlaced phase-stepping techniques, may also be applicable to tomosynthesis using an inner-focusing reconstruction method [23].

Due to a limited field-of-view, restricted by the size of the currently implemented detector grating, the final images presented in this chapter were stitched from multiple projections and required a (undesired) scanning of the breast. However, recently the first gratings with a large field-of-view of $15 \times 15 \, \mathrm{cm^2}$ (round) and $30 \times 5 \, \mathrm{cm^2}$ have been produced. Besides, techniques for the fabrication of bended and tilted gratings, which are intended to adapt the cone-beam geometry of compact mammography systems in order to avoid beam shadowing, are rapidly developing. Along with the clinically compatible imaging results presented here, we are convinced that in-vivo measurements are in near reach and that the development of a clinical prototype is now of highest priority.

7.4 Materials and Methods

7.4.1 Image Processing

Ensuing from the general image processing presented in Chap. 3, the dose-compatible measurements require additional processing steps. Due to the increased integration time of 1 fps, the detector saturates within the regions which are uncovered by breast tissue. Here a simple intensity thresholding is used within the absorption image, to separate the sample from the saturated background. The corresponding mask is then applied to the co-registered differential phase and dark-field projections to enable proper stitching of the latter.

7.4.2 Imaging Dose

In a first step, the incident air kerma was measured using an ionization chamber, which was positioned at the respective breast sample position. To approximate the mean glandular dose (MGD) deposited within the radiation sensitive glandular breast tissue, the incident air kerma (1.19 mGy/s) was then multiplied with a breast-thickness dependent conversion factor g. The respective g-factors were calculated using Monte

7.4 Materials and Methods 107

Carlo simulations (software package CatSim, GE Global Research), taking into account the setup-specific X-ray spectrum and beam filtration [24]. A standard breast phantom was used for the dose model and was simulated as a radiation sensitive tissue core (50% glandular and 50% adipose tissue) of variable thickness surrounded by a 5 mm thick layer of radiation-insensitive skin (100% adipose tissue). For this configuration, we obtained a half-layer value of 0.881 mm aluminium and g-factors ranging from 0.450 to 0.274 for 3 to 6 cm of breast tissue, respectively.

7.4.3 Tomosynthesis Protocol

Within this proof-of-principle study, we used an angular range from -20° to 20° with 41 projections taken at 1° steps, with 7 phase steps and 9 s integration time each. As tomosynthesis was conducted prior to the setup optimization, the total image dose amounts to approximately 2 Gy. Data sets were pre-processed with Fourier analysis and the in-plane projections were reconstructed with a filtered back projection using a Hamming-Filter for the absorption and dark-field data and a Hilbert-Filter for the differential phase signal, respectively. Due to a limited field-of-view only sections of the breast could be investigated with tomosynthesis. After an initial full-field radiography of the mastectomy, a region of interest was selected and the sample holder manually moved into the center of rotation using a sledge-construction connecting sample-holder and stage.

7.4.4 Image Fusion Protocol

A Fourier domain approach was developed in first place to give the radiologist complete freedom in tuning the input images as well as fusing them—for a full documentation please find Coello, E. (2014) [25]. Generally, the fusion protocol follows these steps: the transmission T, differential phase-contrast $\frac{\partial \Phi}{\partial x}$ and visibility image V are normalized, Fourier transformed and each input selectively weightened with a 2D-Gaussian function termed G. The fused Image F is then given as the inverse Fourier Transform of the sum of the weightened input images, by

$$F = \mathcal{F}^{-1}[G_T \mathcal{F}(T) + G_{\frac{\partial \Phi}{\partial x}} \mathcal{F}\left(\left|\frac{\partial \Phi}{\partial x}\right|\right) + G_V \mathcal{F}(V)]. \tag{7.1}$$

The Gaussian function is denoted

$$G = s \cdot e^{-0.5(\sqrt{k^2 + l^2} - c)^2 \sigma^{-2}},\tag{7.2}$$

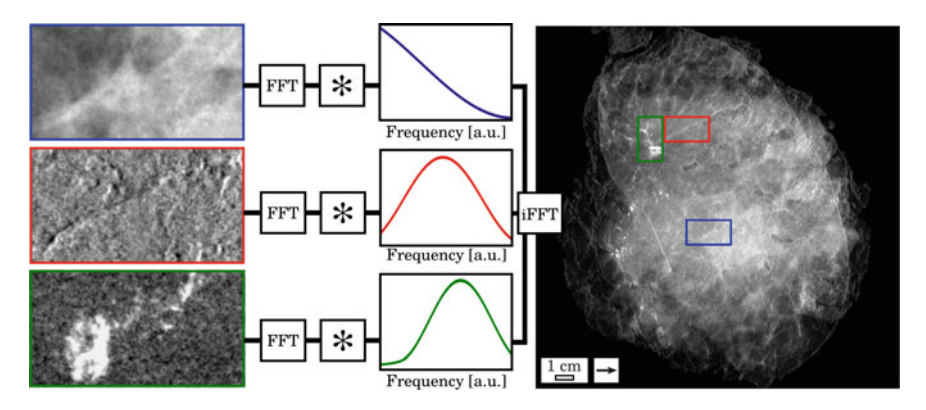


Fig. 7.6 Fusion of trimodal data using a Fourier domain approach. Exemplary sections taken from the absorption (blue), differential phase (red), and dark-field channel (green), showing breast features characteristic for each of the channels. Following Eq. 7.1 the input image are convoluted with a Gaussian to amplify the corresponding frequency bands. Density variation between glandular and adipose tissue are well resolved within the absorption image and extracted by a low-pass filter ($c_T = 0$, $\sigma_T = 0.73$, $s_T = 5$). Fine tissue strands and micro-grains are amplified by convoluting differential phase and dark-field data with a Gaussian, which is shifted towards higher frequencies ($c_{\frac{30}{3x}} = 0.07$, $\sigma_{\frac{30}{3x}} = 0.61$, $s_{\frac{30}{2x}} = 1.5$; $c_V = 0.2$, $\sigma_V = 0.51$, $s_V = 1.5$). The fused full-field mammogram provides the radiologists with diagnostic meaningful image content, from all three signals, at a single glance

where k, l are the Fourier space coordinates, c and σ determine the center and bandwidth of the frequency band and s is a scaling factor, respectively. In a first step c and σ are visually tuned to optimize the signal-to-noise ratio within the input images and an uniform fusion (s = 1) of the latter conducted. Afterwards, the scaling parameters are optimized in such a manner, that the diagnostically interesting features are optimally represented in the fused image. Figure 7.6 illustrates the fusion process by means of the dose-compatible measured breast abladate. Since the transmission channel excels at the depiction of extended density variations, e.g. between fatty and glandular tissue (blue frame), the latter is convoluted with a low-pass filter ($c_T = 0, \sigma_T = 0.73, s_T = 5$). Contrasting, as Chap. 4 showed, high-frequency features, such as fine fibres and tissue strands (red framed), are best depicted within the differential phase channel. These are extracted by convoluting the differential phase data with a Gaussian function which is shifted towards higher frequencies $(c_{\frac{\partial \Phi}{\partial x}} = 0.07, \sigma_{\frac{\partial \Phi}{\partial x}} = 0.61, s_{\frac{\partial \Phi}{\partial x}} = 1.5)$. Finally, the dark-field image depicts scattering structures which are often smaller or equal in size than a detector pixel, for instance micro-grains (green frame), which typically are best preserved using a highfrequency shifted Gaussian ($c_V = 0.2, \sigma_V = 0.51, s_V = 1.5$). Hereby, the Gaussian is chosen to be rather narrow in order to minimize an amplification of high-frequency noise, prominent in the dark-field image.

References 109

References

1. Pfeiffer, F., Weitkamp, T., Bunk, O., & David, C. (2006). Phase retrieval and differential phase-contrast imaging with low-brilliance X-ray sources. *Nature Physics*, 2, 258–261.

- Scherer, K., et al. (2014). Bi-directional X-ray phase-contrast mammography. PLoS One, 9, e93502.
- 3. Stampanoni, M., et al. (2011). The first analysis and clinical evaluation of native breast tissue using differential phase-contrast mammography. *Investigative Radiology*, 46, 801–806.
- 4. Hauser, N., et al. (2014). A study on mastectomy samples to evaluate breast imaging quality and potential clinical relevance of differential phase contrast mammography. *Investigative Radiology*, 49, 131–137.
- 5. Michel, T., et al. (2013). On a dark-field signal generated by micrometer-sized calcifications in phase-contrast mammography. *Physics in Medicine and Biology*, *58*, 2713–2732.
- 6. Perry, N., et al. (2008). European guidelines for quality assurance in breast cancer screening and diagnosis. Fourth edition-summary document. *Annals of Oncology*, 19, 614–622.
- 7. Wang, Z., et al. (2013). Image fusion scheme for differential phase contrast mammography. *Journal of Instrumentation*, 8, C07011.
- 8. Scholkmann, F., et al. (2014). A new method for fusion, de-noising and enhancement of X-ray images retrieved from Talbot-Lau grating interferometry. *Physics in Medicine and Biology*, *59*, 1425–1440.
- 9. Donath, T., et al. (2009). Inverse geometry for grating based X-ray phase-contrast imaging. *Journal of Applied Physics*, 106, 054703.
- 10. Hendrick, R., Bassett, L., & Botsco, M. (1999). *Mammography quality control manual*. Preston: American College of Radiology.
- 11. Skaane, P., et al. (2013). Comparison of digital mammography alone and digital mammography plus tomosynthesis in a population-based screening program. *Radiology*, 267, 47–56.
- 12. Haas, B., et al. (2013). Comparison of tomosynthesis plus digital mammography and digital mammography alone for breast cancer screening. *Radiology*, 269, 694–700.
- 13. Alimoglu, E., Ceken, K., Kabaalioglu, A., Cassano, E., & Sindel, T. (2010). An effective way to solve equivocal mammography findings: the rolled views. *Breast Care*, 5, 241–245.
- 14. Smith, A. (2008). Fundamentals of breast tomosynthesis. Bedford: Hologic Inc.
- 15. Hammonds, J., Price, R., Donnelly, E., & Pickens, D. (2011). Phase-contrast digital tomosynthesis. *Medical Physics*, 38, 2353–2358.
- 16. Schleede, S., et al. (2014). X-ray phase-contrast tomosynthesis for improved breast tissue discrimination. *European Journal of Radiology*, 83, 531–536.
- 17. Li, K., et al. (2014). Grating-based phase contrast tomosynthesis imaging: proof-of-concept experimental studies. *Medical Physics*, 41, 011903.
- 18. Wang, Y. (2007). Intuitive dimensional analyses of the energy and atomic number dependences of the cross sections for radiation interaction with matter. *Journal of X-Ray Science and Technology*, 15, 169–175.
- 19. Sarapata, A., et al. (2015). Quantitative imaging using high-energy X-ray phase-contrast CT with a 70 kVp polychromatic X-ray spectrum. *Optics Express*, 23, 523–535.
- 20. Wang, Z., et al. (2013). Image fusion scheme for differential phase contrast mammography. *Journal of Instrumentation*, 8, C07011.
- 21. Hologic Inc., Bedford. Selenia Dimensions data sheet. (2015). http://www.hologic.com/products/imaging/mammography.
- 22. Sidky, E., et al. (2008). Practical iterative image reconstruction in digital breast tomosynthesis by non-convex TpV optimization. Bellingham: SPIE Medical Imaging.
- 23. Xi, Y., & Zhao, J. (2013). Fast grating-based X-ray phase-contrast tomosynthesis. *EMBC*, 35, 2320–2323.
- 24. De Man, B., et al. (2007). CatSim: a new computer assisted tomography simulation environment. *Proceedings of SPIE*, 6510, 65102–65108.
- Coello, E. (2014). Image fusion in X-ray phase contrast imaging. Munich: Technische Universität München.

Chapter 8 Non-invasive Kidney Stone Differentiation Using Dark-Field Radiography

Vor die Therapie setzten die Götter die Diagnose.

Franz Volhard

Abstract In this chapter, we propose scatter-sensitive dark-field radiography as a diagnostic tool for the differentiation of renal stones and detection of radio-lucent calculi. First, we elucidate on the current shortcomings of clinical renal stone diagnostics, by which the presented study is motivated. Afterwards, we utilize knowledge on the micromorphology of kidney stones—which is indirectly assessed via dark-field radiography—for the refinement of conventional, absorption-based stone assessment. Finally, we conclude with an outlook on clinical transferability, by investigating renal stones embedded within a preliminary abdomen phantom. Note that the results presented in this chapter have been published as "Scherer, K. et al. Noninvasive differentiation of kidney stone types using X-ray dark-field radiography. *Sci. Rep.* **5**, 9527 (2015)".

8.1 Motivation | Limitations of Clinical Kidney Stone Diagnostics

The correct identification of the different renal calculi commonly found in the human body is of essential importance for the correct diagnosis, prognosis and therapy of many common diseases of the genitourinary system. For example, while urinary acid stones can occur in any healthy subject, struvite stones indicate an infection within the patient. In therapy, lithotripsy can be successfully administered for the uric acid type of kidney stones, while other types of calculi are more resistant to this type of therapy [1, 2].

Nevertheless, while standard imaging methods like computed tomography and sonography are helpful in localizing calculi in the body, they only yield modest results in the correct identification of the stone type [3, 4]. Further ultrasonography

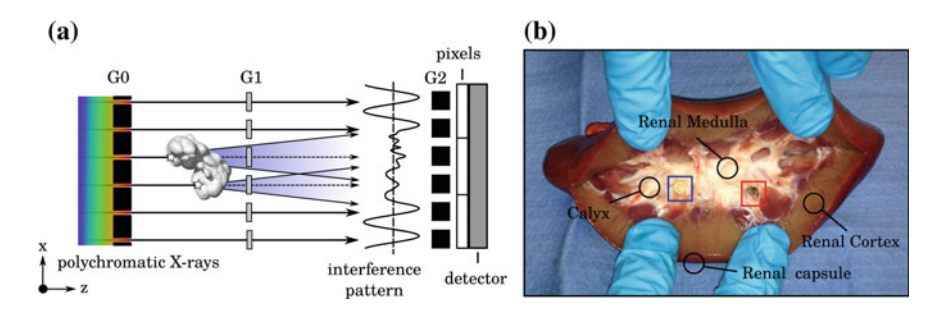


Fig. 8.1 Study design: non-invasive differentiation of kidney stone using dark-field radiography. **a** Diffuse X-ray scatter originating from sub-structures of the kidney stone manifest themselves in a local reduction of a phase-grating induced interference pattern. By analysing the dark-field signal, information on the kidney stone micromorphology, well below the detector resolution limit can be retrieved. **b** Photography of a fresh pig kidney with two renal stones embedded, used to show-cast X-ray dark-field radiography and potential in-vivo transferability. One exemplary uric acid (blue framed) and one calcium oxalate stone (red framed) were manually embedded in the fresh pig kidney before measurement

yields little detection sensitivity towards small stones. Respectively, an examination of the patients urine, or a removal of exemplary stones followed by a histological work-up is required in most cases. Currently, dual energy CT is evaluated with some success [5].

Recent developments in phase-sensitive X-ray imaging [6–8] have broadened the horizon of X-ray image contrast generation and are currently being evaluated for clinical application in a variety of diagnostic fields [9]. Among these, X-ray dark-field imaging [10] attracted particular interest, being sensitive towards structural changes in the micromorphology of tissue, as for instance associated with pathological processes of breast and lung tissue [11–13]. In contrast to absorption-based imaging, which solely relies on the reduction of beam intensity when introducing a specimen, dark-field contrast is generated by diffuse angular deflections of the X-ray wave-front when being scattered at inherent sub-structures. By resolving the scatter associated reduction of a phase grating induced interference pattern, the dark-field signal strength can be quantified, as illustrated in Fig. 8.1. The dark-field signal has been shown to be highly dependent not only on the chemical composition of the imaged sample, but decisively also on the sample's morphological structure on the micrometer scale [14, 15], well below the resolution limit of commonly used imaging detectors.

The idea underlying our present work is to try to discriminate uric acid, calcium oxalate and mixed types of stones from each other within a radiographic imaging mode, on the ground of the complementarity of their absorption and dark-field contrasts, which is based on differences between their morphological and chemical compositions. While the absorption and dark-field images will be obtained from a lab-based radiography setup, the micromorphological information (which are used to illustrate the generation of dark-field signal strength) will be assessed using highly resolving micro-CT.

8.2 Results 113

8.2 Results

8.2.1 Analytical Description

Formally, the measured projection value in absorption contrast $\bar{\mu}$ can be written as

$$\bar{\mu} = -\ln T = \int_0^L \mu(z) \, dz,$$
 (8.1)

where the transmission $T = I^s/I^r$ is obtained from the measured intensity I^s , relative to a reference intensity I^r measured without the kidney stone, μ being the absorption per unit length and L the stone thickness. As shown by Bech, M. et al., under the simplified assumption of ideally random scattering, the dark-field signal in projection mode can similarly be written as

$$\bar{\epsilon} = -\ln V = i \int_0^L \epsilon(z) \, dz,\tag{8.2}$$

where the visibility (dark-field) signal $V = V^s/V^r$ can be obtained from the interferometric visibilities V^s and V^r with and without stone, respectively, ϵ being the linear diffusion coefficient, quantifying the scattering per unit length, and i being a setup-specific constant (cf. Eq. 2.48) [16]. To account for the problem of overlaying structures in projection mode, we can formally describe the kidney stone as consisting of a perfectly homogeneous material along each projection path, and assign to this hypothetical material an "effective" absorption and scattering coefficient $\mu_{\rm eff}$ and $\epsilon_{\rm eff}$, respectively,

$$\bar{\mu} = \mu_{\text{eff}} \cdot L$$
 and $\bar{\epsilon} = i \cdot \epsilon_{\text{eff}} \cdot L$. (8.3)

The effective coefficients $\mu_{\rm eff}$ and $\epsilon_{\rm eff}$ are thus defined as a weighted average of the contribution of the absorption and scattering coefficients along each projection path

$$\mu_{\text{eff}} = \frac{1}{L} \int_0^L \mu(z) dz$$
 and $\epsilon_{\text{eff}} = \frac{1}{L} \int_0^L \epsilon(z) dz$. (8.4)

Interpreted in this way, the ratio of the projection values

$$\frac{\bar{\mu}}{\bar{\epsilon}} = \frac{\mu_{\text{eff}}}{i \cdot \epsilon_{\text{off}}} = c, \tag{8.5}$$

can be seen to be independent of the total kidney stone thickness L. Thus, in this approximation, we assume that there is a linear relationship between the measured $\bar{\epsilon}$ ($\epsilon_{\rm eff}$) and $\bar{\mu}$ ($\mu_{\rm eff}$) values, and that the slope c relating the two parameters is constant and characteristic for each kidney stone type. The simultaneous measurement of

absorption and scattering thus allows the cancellation of the thickness dependence in projection mode, as well as the identification and classification of different kidney stones by using the obtained slope c as a binary classifier.

8.2.2 Absorption Characteristics of Renal Calculi

The effective absorption coefficient $\mu_{\rm eff}$ is proportional to $Z_{\rm eff}^{3-4}$, whereas the effective atomic number $Z_{\rm eff}$ of the composite is mostly determined by the heaviest element in the kidney stone [17]. Thus, with respect to absorption, two classes of kidney stones can immediately be differentiated: the uric acid type of stones on the one hand, and the calcified stones (the oxalate, brushite and apatite/dahllite) on the other hand. While the heavy calcium ion in the calcified stones leads to a strong absorption signal ($Z_{\rm eff}\approx 14$ –16, large $\mu_{\rm eff}$), the uric acid stones contain only low Z elements like carbon, nitrogen and oxygen which implies a small absorption signal ($Z_{\rm eff}\approx 7$, small $\mu_{\rm eff}$), respectively. Struvite and cystine have intermediate atomic numbers ($Z_{\rm eff}\approx 10$ –12). Nevertheless, those chemicals mostly occur only in combination with other crystallite phases and thus usually fall into the mixed stone category, with effective absorption coefficients $\mu_{\rm eff}$ ranging between the uric acid and calcium oxalate class.

8.2.3 Scattering Characteristics of Renal Calculi

The classification of kidney stones by their scattering properties is more difficult, since the morphological structure and stone formation heavily depend on the mineralogical composition, the time varying chemical composition of the urine, the location and time of formation, the presence of growth inhibitors and catalyses, the inclusion of organic matrix, among others [18, 19]. Thus, for the sake of simplicity, micro-CT investigations are restricted to pure uric acid and calcium oxalate stones in the following, signifying two micromorphological extremes.

Uric acid type of kidney stones are known to grow in a layer-wise manner as concentric rings around a crystallite core [18]. This multi-shell structure is well reflected by the micro-CT measurement of an uricite stone as shown in Fig. 8.2a. The inner structure of the uricite stone displays a high textural irregularity comprising various grain sizes rutted with ring-like structures of higher optical density. Further, the exterior exhibits a distinct surface roughness containing large cavities and sharp edges. Since scatter predominately originates at boundaries with locally changing density and structure, uric acid stones are expected to have a large effective scatter coefficient $\epsilon_{\rm eff}$.

In contrast, in the case of calcium oxalate stones crystal forming is typically driven by a slow and regular crystalline growth (The exact stone formation is complex and dependent on many factors, among others the presence of crystallization cores and the ratio of mono-hydrate to di-hydrate) [19]. As a consequence, especially in

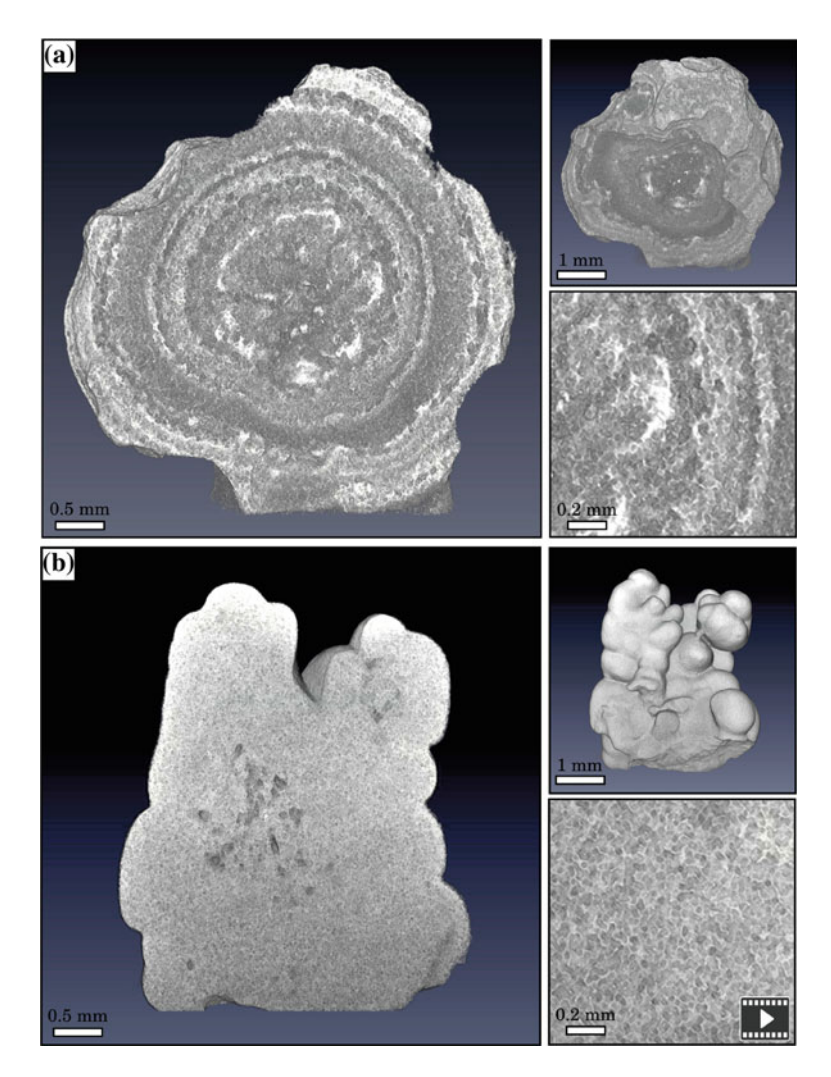


Fig. 8.2 Comparison of the uric acid and calcium oxalate stone morphology. a The volumetric micro-CT rendering of an uric acid-type kidney stone reveals a highly concentric growth structure, accompanied by a particular rough stone surface. The zoom-in of the tomographic slice shows high textural and optical irregularity induced by the multi-shell structure. b The volumetric micro-CT rendering of the calcium oxalate (90 % mono-hydrate and 10 % di-hydrate) stone, showing a strongly homogeneous microstructure with a smooth stone exterior. The zoom-in of the tomographic slice reveals fine, regularly distributed crystallite cores on the micrometer scale. The non-uniformity in optical density and structure in the case of the uricite stone compared with the calcium oxalate stone manifests itself in a significantly increased effective scatter coefficient $\epsilon_{\rm eff}$. For a respective volumetric micro-CT rendering find Fig. A.4

the case of calcium oxalate mono-hydrate, stones exhibit a relatively homogeneous microstructure with wedges rounding off and forming a smooth exterior [20]. This corresponds well with the micro-CT measurements of a 90% mono-hydrate and 10% dihydrate stone featuring a strongly uniform micromorphology with only minor structural disturbances in the form of some air cavities as shown in Fig. 8.2b. The high degree of regularity in grain size, a steady optical density throughout the stone and smooth stone surface manifest themselves in a very small effective scatter coefficient $\epsilon_{\rm eff}$.

Mixed types of stones comprise a more variable crystalline growth pattern, being more irregular in shape and structure than calcium oxalate stones, hence are expected to yield an intermediate effective scatter coefficient $\epsilon_{\rm eff}$.

8.2.4 X-Ray Dark-Field Radiography of Renal Calculi

Grating-based transmission and dark-field radiographies of an excised calcium oxalate and uric acid stone can be seen in Fig. 8.3a, b. While the calcium oxalate stone (top left inlay) exhibits a relatively high absorption (low transmission T, large $\mu_{\rm eff}$) and weak scattering signal (high visibility V, small $\epsilon_{\rm eff}$), directly inverse observations are made in case of the uric acid stone (top right inlay), which is in accordance

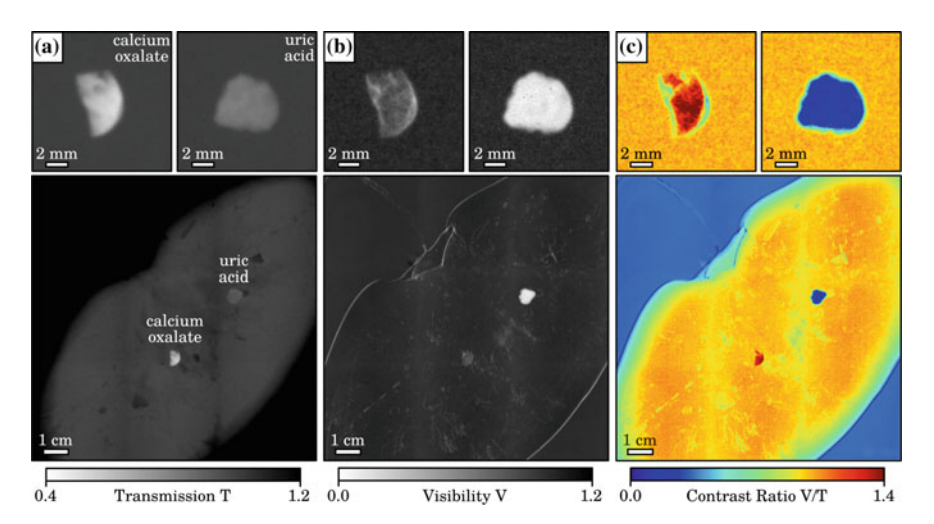


Fig. 8.3 Visual classification scheme for the discrimination of uric acid and calcium oxalate renal stones using X-ray dark-field radiography. **a** Transmission images T of an calcium oxalate (top left), uric acid stone (top right) and a pig kidney with both stones embedded (bottom), taken at 40 kVp tube voltage. **b** Corresponding visibility images V. **c** Since both stones show opposite absorption and scatter characteristics, the visibility-to-transmission ratio V/T allows a simple visual differentiation of stone class and discrimination from surrounding kidney tissue in false color. Note that the uric acid stone appears radio-lucent, while yielding high contrast in the dark-field image

8.2 Results 117

with previously discussed chemical and morphological stone properties. Based on the complementarity of both image signals, the two calculi can be clearly and easily differentiated in radiographic mode, as shown in Fig. 8.3c in false color, by deriving the thickness-independent visibility-to-transmission ratio V/T. Afterwards, we measured a fresh pig kidney with both stones embedded in the inside with an imaging dose of 5.2 mGy (bottom inlays), to demonstrate the potential of kidney stone assessment via X-ray dark-field radiography as a future in-vivo application: consequently, a superior visual differentiation and discrimination between the two calculi and surrounding kidney tissue could be achieved also within native tissue. Note that images were normalized with respect to surrounding tissue/material in order to compensate for signal not directly arising from the kidney stones themselves.

8.2.5 Statistical Analysis of Renal Calculi Classification

To evaluate this trend statistically, i.e. review the potential differentiate uric acid and calcium oxalate from each other and also discriminate the latter from mixed stone types, a cohort of 118 stones was analysed.

Each stone was segmented, normalized with respect to the background and separately analysed by generating a scatterplot of $\bar{\mu}$ versus $\bar{\epsilon}$ using every pixel of each stone as data-points, as exemplarily shown for three stones in Fig. 8.4a. Each point cloud belonging to a specific stone was then analysed separately using linear regression through the origin, evaluating the slope c (used as binary classifier) and the coefficient of determination R^2 of each stone. For each class, the obtained slopes were then arithmetically averaged to obtain a mean slope value \bar{c} which is characteristic for each class. For uric acid stones, we obtain $\bar{c}_U = 0.13 \pm 0.01$, for the calcium oxalate $\bar{c}_O = 0.97 \pm 0.44$, and for the mixed stones $\bar{c}_M = 0.31 \pm 0.13$. The error is obtained as the standard deviation of the slopes ensemble of each class. The coefficient of determination was used as an indicator of the goodness-of-fit and calculated to $R^2 = 0.80 \pm 0.16$ over the full sample collective, thus justifying the linear proportionality assumption expressed by Eq. 8.5.

We investigated the distributions of slope values c for each of the 118 stones in more detail by using a box-whisker diagram as shown in Fig. 8.4b. In addition to significantly differing median values (black dash), no overlap in interquartile data (50% of the data set as indicated by boxes) was observed for either of the three stone classes. Further, except two outliers (circles) all uric acid stones exhibited exclusively flatter slopes c then in comparison with the calcium oxalate stones.

8.2.6 Diagnostic Performance of Renal Calculi Classification

To verify whether the decisive change in effective absorption $\bar{\mu}$ to scatter power $\bar{\epsilon}$ with respect to stone class yields sufficient diagnostic value, receiver operating

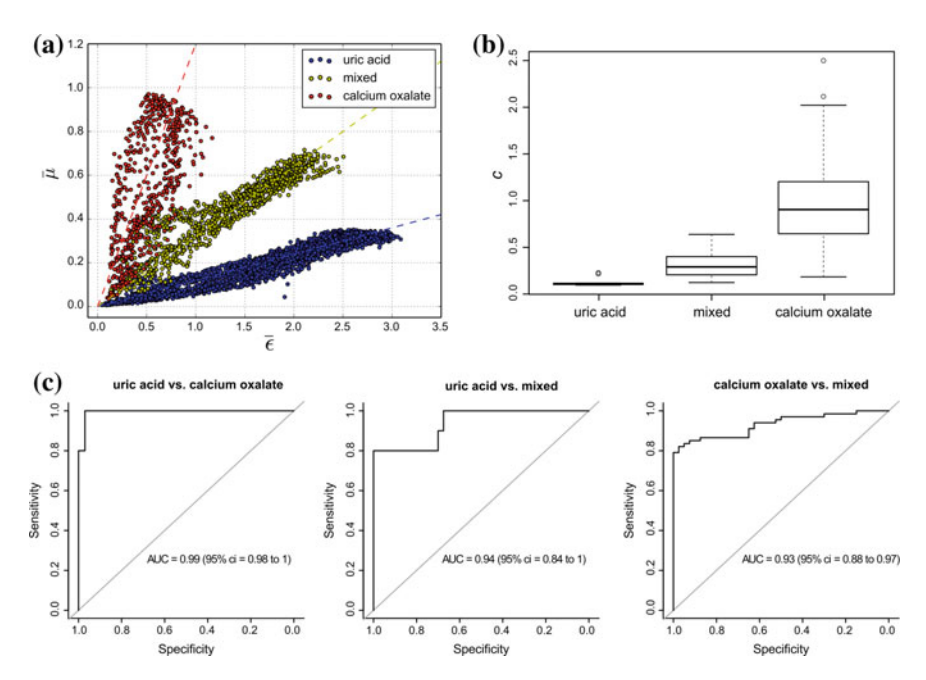


Fig. 8.4 Statistical analyses adjudge superior diagnostic performance of kidney stones assessment via X-ray dark-field radiography. a Scatter plot showing the ratios of $\bar{\mu}$ versus $\bar{\epsilon}$ for every image pixel of an exemplary uric acid (blue), calcium oxalate (red) and mixed types of kidney stones (yellow). Each data-cloud was fitted by a linear regression as indicated by dashed lines, and it slope c used as a binary stone type classifier. b Box-whisker plot showing the distributions of slope values c, determined for the uric acid, calcium oxalate and mixed stone collective. In addition to strongly differing mean values (black line) no overlap in interquartile data was found (box). c Receiver operator statistic analyses on the data presented in b, show a highly sensitive and specific differentiation of all three stone classes using X-ray dark-field radiography (Area under curve >0.9)

characteristic (ROC) analyses were carried out. The ROC curve provides combinations of specificity versus sensitivity when using the slope *c* as a binary classifier with varying threshold as shown in Fig. 8.4c. The diagnostic performance of renal calculi assessment via dark-field imaging was estimated by the area under the ROC curve (AUC). In the case of uric acid and calcium oxalate stones, a nearly unambiguous discernability between both classes was found using X-ray dark-field radiography, quantified by a AUC value of 0.99 (95 % bootstrap confidence interval of 0.98 to 1).

An optimal threshold value (Youden-Index), maximizing the sum of diagnostic sensitivity (100%) and specificity (97%), was found for c = 0.26. Besides, also mixed type of renal stones were found to be distinguishable with a high accuracy from both uric acid (AUC of 0.94, 95% bootstrap confidence interval of 0.84–1) and calcium oxalate stones (AUC of 0.93, 95% bootstrap confidence interval of 0.88–0.97).

8.3 Conclusion | Highly Sensitive Kidney Stone Assessment via Dark-Field Abdomen Radiography

Here, we have shown that the comparison of absorption and dark-field signal strength can determine the composition of different calculi classes of the genitourinary system. Our study was able to establish a clear trend in the absorption-to-scattering ratio, which we could directly assign to chemical and morphological differences of calcium oxalate and uric acid stones. We further deepened this correlation by means of statistical analyses and scatter plots. A simple visual inspection of the visibility-to-transmission signal strength was presented to allow a quick and convenient determination of the stone type, compatible with clinical routine. Finally, receiver operator characteristics including 118 stones from 18 patients revealed an outstanding diagnostic performance of dark-field radiography for the accurate differentiation of pure uric acid and calcium oxalate calculi as well as discrimination of mixed types of stones.

To secure our statistical findings and further clarify the origins of dark-field contrast with respect to stone micromorphology, especially aiming at complicated, rare and mixed stone types, more work including an increased sample collective and patient cohort is to be performed in the near future. Follow-up studies will focus on the deduction of composite-specific classifier values, enabling a more detailed differentiation of mixed types of stones into their chemical sub-groups.

Besides, we consider X-ray dark-field radiography to provide a superior detection sensitivity towards certain renal stones in comparison to conventional radiography, due to the demonstrated complementarity of absorption- and scatter-based imaging. While uric acid stones are usually entirely radio-lucent, which involves a high risk of being overlooked in conventional radiography and CT (see Fig. 8.3a), they are clearly revealed and delineated by the dark-field signal (see Fig. 8.3b) [21]. Also in the case of mixed types of stones, the dark-field signal strength exceeds the respective absorption entity by far ($c \ll 1$, Fig. 8.4b), which is of major clinical interest taking into account that only 60% of all renal stones are radiopaque [22].

As this initial study was aimed at determining the potential of dark-field imaging in the differentiation of kidney stones in the sense of a proof-of-principle study, mostly excised stones were measured within an ex-vivo framework. In a first step, we could successfully verify our classification scheme by fully scanning a fresh pig kidney with two manually embedded stones, while keeping the dose applied considerably low at 5.2 mGy. Although this value may not directly apply to a full abdomen scan, it is in the same order of magnitude as clinical dose values (0.7 and 8.0 mGy in case of an abdomen radiogram and CT, respectively) [23]. Thus we are convinced that dose-compatible abdomen dark-field radiography could be achieved, considering that an optimization of interferometer efficiency by tuning several setup entities (grating height and quality, duty cycle, beam energy and filtration) would imply a significant decrease in dose, while maintaining equivalent image quality [24, 25].

For the purpose of further pursuing clinical transferability of the proposed method in the near-term, we modelled a first medical meaningful scenario mimicking an

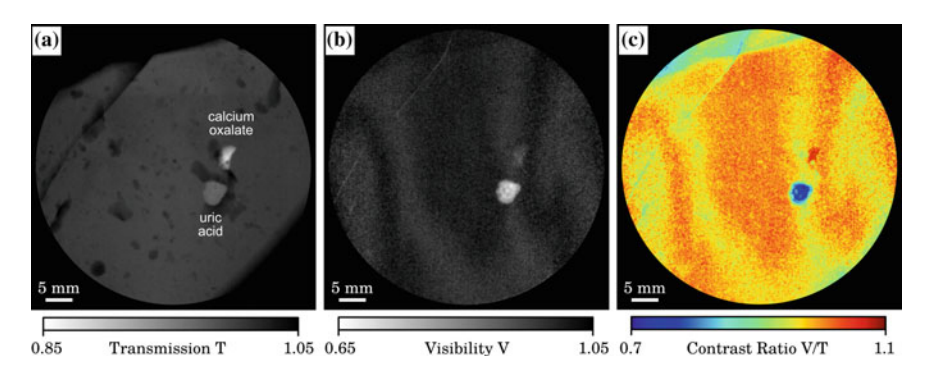


Fig. 8.5 In-vivo transferability study of a preliminary abdomen phantom at 100 kVp tube voltage. **a** High-energy transmission image T of a pig kidney, with manually embedded uric acid and calcium oxalate stones, placed within a 11 cm water-bath. **b** Corresponding visibility image V, revealing concentric growth rings of the uric acid stone. **c** The visibility-to-transmission V/T signal enables a clear differentiation of uric acid (blue) and calcium oxalate (red), consistent with the 40 kVp measurements shown in Fig. 8.3

abdomen phantom: a second pig kidney, with both stones embedded was placed within a 11 cm water-bath and measured at a high-energy laboratory setup running at $100\,\mathrm{kVp}$, which is the energy range of tube voltages used in commercial systems. The preliminary obtained measurements shown in Fig. 8.5 prove that an inversion of visibility-to-transmission signal when comparing uric acid and calcium oxalate stones is still existent, even in the case of very high X-ray energies (E) and significant beam-hardening. Future studies have to investigate, whether this does hold true for the differentiation from mixed types of stone, considering that $\mu_{\rm eff}$ and $\epsilon_{\rm eff}$ are proportional to E^{-3} and E^{-2} , respectively [14]. An increase in mean energy namely implies the drawback of converging and shrinking scatter plots offering a correspondingly reduced diagnostic performance.

Keypoints

- Dark-field radiography provides a highly sensitive and specific tool for the differentiation of uric acid, mixed and calcium oxalate renal stones.
- The dark-field signal can reliable detect radio-lucent uric acid stones, contingent on the complementary of absorption and small-angle scattering contrast.
- Kidney stone assessment via dark-field abdomen radiography is considered to be clinically applicable.

Further an animal model is envisioned to address concerns regarding the impact of structures overlying the kidney in radiographic imaging mode and discriminability of small and initially growing calculi in-vivo [26]. Especially in the case of inhomogeneous structure compositions or strongly absorbing tissue underlying the kidney

stone data normalization could be ambiguous, resulting in a limited accuracy in the determination of the stone type classifier c.

Finally, X-ray dark-field radiography is susceptible to superposing renal stones; hence an additional lateral radiogram of the abdomen or the implementation of advanced techniques such as tomosynthesis would be necessary to support diagnostic reliability. Besides, current technical limitations need to be challenged, such as the fabrication of bended, large field-of-view gratings with high aspect ratios, in order to significantly reduce scan-time and secure a successful implementation of non-invasive kidney stone assessment via X-ray dark-field radiography into clinical routine.

8.4 Materials and Methods

8.4.1 Study Design

A broad range of different kidney stones was acquired in order to have a representative sample collective. Nevertheless, the classification of kidney stones is in general complicated by the fact that most kidney stones in practice are rarely composed of a single pure chemical material, but are instead a mixture of various components with widely differing composition [27]. Thus in this proof-of-principle study we focus on the differentiation of three classes of kidney stones only: the pure uric acid stones, the pure calcium oxalate stones, and the mixed stone class including composites of brushite, carbon apatite and struvite. The different kidney stone types that occur in practice are summarized in Table 8.1 by compound name, chemical formula and mineralogical name.

The samples in our measurements were acquired by the Klinikum rechts der Isar, Department of Radiology. Each patient had their renal stone(s) removed following the common clinical practice with respect to their individual diagnosis and indication. Written and informed consent was obtained from all patients. Nine patients were found with a mixture of Whewellite and Weddelite, four patients with uric acid stones, and five patients with mixed stones types. From these patients, we obtained 68 oxalate stones, 10 uric acid stones, and 40 mixed stones, thus a total of 118 renal calculi was accessed and imaged. The composition of each kidney stone was determined by Fourier-transform infrared spectroscopy (FTIR) [28], using a Spectrum 100 system by Perkin Elmer, Beaconsfield, UK. The exact chemical composition of the calculus was determined by comparing the recorded spectrum with tabulated spectra. Components of stones were given in percentages, in which a concentration of more than 90 % of one component was regarded as pure. More details on the study design, patient selection routine, patient examination and exact composition of the kidney stone collective can be found in Eiber, M. et al. (2012) [5].

Compound name	Chemical formula	Mineralogical name	
Calciumoxalate-Monohydrate	$CaC_2O_4 \cdot H_2O$	Whewellite	
Calciumoxalate-Dihydrate	$CaC_2O_4 \cdot 2H_2O$	Weddelite	
Uric acid	$C_5H_4N_4O_3$	Uricite	
Uric acid dihydrate	$C_5H_4N_4O_3\cdot 2H_2O$	None	
Ammonium urate	$(NH_4)C_5H_3N_4O_3$	None	
Sodium urate monohydrate	$NaC_5H_3N_4O_3 \cdot H_2O$	None	
Calcium hydrogenate phosphate	$CaH(PO_4) \cdot 2H_2O$	Brushite	
Carbonate hydroxylapatite	$Ca_5(PO_4, CO_3)_3(OH)$	Apatite/Dahllite	
Magnesium ammonium phosphate	$Mg(NH_4)(PO_4) \cdot 6H_2O$	Struvite	
Cystine	$C_6H_{12}N_2O_4S_2$	none	

Table 8.1 Overview of the different types of kidney stones

Summary of renal stones relevant for this study, with chemical name, formula and mineralogical name. Stoichiometry adapted from Stoller, M. et al. (2007) [27]

8.4.2 Statistical Analysis

Statistical analysis was carried out using the statistical software *R* and its library *pROC* [29, 30]. Outliers were considered in the ROC analysis. Two thousand stratified bootstrap samples were drawn for each ROC analysis to estimate 95 % confidence intervals for the area under the ROC curve.

8.4.3 Micro-CT Measurements

We performed micro-CT measurements at a commercial GE VtomeX system, using a reflection tube with a voltage setting of 100 kVp at a current of 10 mA. For the tomographic scan we took 1200 projections over 360°, with an exposure time of 1 s each. Datasets were reconstructed using a standard filtered backprojection, rendered in Volume Graphics VGStudio MAX and analyzed visually. An example volume rendering can be seen in Fig. 8.2.

8.4.4 X-Ray Dark-Field Interferometer

For the statistical analysis, we normalized the projections with respect to the sample holder, in order to remove all contributions not originating from the kidney stone. All stones were then segmented from the background by intensity thresholding and their $\bar{\epsilon}$ and $\bar{\mu}$ -values were tabulated for each single pixel for further analysis. For

the purpose of validating in-vivo feasibility of renal calculi assessment via dark-field radiography, one calcium oxalate and one uric acid stone were additionally embedded and subsequently measured within a fresh pig kidney as illustrated in Fig. 8.1b. We derived comprehensive images of the pig kidney with a field-of-view of $12.8 \times 12.8 \, \mathrm{cm}^2$ by stitching 16 single projections taken with 5 phase-steps and 1 second exposure time each

123

8.4.5 Imaging Dose

The total air kerma of the pig kidney measurement was determined to be 10.5 mGy (incident air kerma rate 2.1 mGy/s) with a Dosimax plus/RQX-detector system. To give a rough estimate of the effective dose deposited in the kidney, we calculated the mean glandular dose of a 100% glandular breast tissue equivalent (underlying consideration are based on the fact that glandular breast and kidney tissue yield similar mass density coefficients) [31]. We obtained a mean dose of 5.2 mGy, by multiplying the total incident air kerma with a Monte-Carlo based conversion factor of 0.56 and a correction factor accounting for 100% glandular breast tissue of 0.9. Values arise from a half-value layer (Al) of 0.8 mm and a kidney thickness of 3 cm [32, 33].

8.4.6 Potential Clinical Implementation

In a first step, the radiologist marks the renal stone in the digital radiogram. Since stone edges yield excessive scatter corresponding regions are excluded from the data analysis. An algorithm is determining the surrounding tissue and calculating the respective mean signal values in both the absorption and dark-field channel, by which the renal stone is subsequently normalized. This is feasible since the kidney stone is distinctively thinner than the patient. In a next step, the scatter plot is generated from $\bar{\epsilon}$ and $\bar{\mu}$ and the binary stone classifier c extracted as the mean slope of the data points, by which the respective stone type can be determined from a look-up table. Finally, by reading the maximum ordinate of the scatter plot $(\bar{\mu})$ the thickness of kidney stone in beam direction can be approximated.

References

- Brown, J. (2006). Diagnostic and treatment patterns for renal colic in US emergency departments. *International Urology and Nephrology*, 38, 87–92.
- Coe, F. L., Evan, A., & Worcester, E. (2005). Kidney stone disease. *Journal of Clinical Investigation*, 115, 2598–2608.
- 3. Dalla Palma, L., Pozzi-Mucelli, R., & Stacul, F. (2001). Present-day imaging of patients with renal colic. *European Radiology*, 11, 4–17.
- 4. Bellin, M., et al. (2004). Helical CT evaluation of the chemical composition of urinary tract calculi with a discriminant analysis of CT-attenuation values and density. *European Radiology*, *14*, 2134–2140.
- 5. Eiber, M., et al. (2012). Targeted dual-energy single-source CT for characterisation of urinary calculi: experimental and clinical experience. *European Radiology*, 22, 251–258.
- Davis, T., Gao, D., Gureyev, T., Stevenson, A., & Wilkins, S. (1995). Phase-contrast imaging of weakly absorbing materials using hard X-rays. *Nature*, 373, 595–598.
- 7. Wilkins, S., Gureyev, T., Gao, D., Pogany, A., & Stevenson, A. (1996). Phase-contrast imaging using polychromatic hard X-rays. *Nature*, *384*, 335–338.
- 8. Pfeiffer, F., et al. (2006). Phase retrieval and differential phase-contrast imaging with low-brilliance X-ray sources. *Nature Physics*, 2, 258–261.
- Bravin, A., Coan, P., & Suortti, P. (2013). X-ray phase-contrast imaging: From pre-clinical applications towards clinics. *Physics in Medicine and Biology*, 58, 1–35.
- 10. Pfeiffer, F., et al. (2008). Hard-X-ray dark-field imaging using a grating interferometer. *Nature Materials*, 7, 134–137.
- 11. Hauser, N., et al. (2014). A study on mastectomy samples to evaluate breast imaging quality and potential clinical relevance of differential phase-contrast mammography. *Investigative Radiology*, 49, 131–137.
- Schleede, S., et al. (2012). Emphysema diagnosis using X-ray dark-field imaging at a laserdriven compact synchrotron light source. *Proceedings of the National Academy of Sciences*, 109, 17880–17885.
- 13. Michel, T., et al. (2013). On a dark-field signal generated by micrometer-sized calcifications in phase-contrast mammography. *Physics in Medicine and Biology*, 58, 2713–2732.
- 14. Yashiro, W., Terui, Y., Kawabata, K., & Momose, A. (2010). On the origin of visibility contrast in X-ray Talbot interferometry. *Optical Materials Express*, 18, 16890–16900.
- 15. Lynch, S., et al. (2011). Interpretation of dark-field contrast and particle-size selectivity in grating interferometers. *Applied Optics*, 50, 4310–4319.
- Bech, M., et al. (2010). Quantitative X-ray dark-field computed tomography. Physics in Medicine and Biology, 55(18), 5529–5539.
- 17. Tomasz, K., Podgorski, P., Guzinski, M., Czarnecka, A., & Tupikowski, K. (2012). Novel clinical applications of dual energy computed tomography. *Advances in Clinical and Experimental Medicine*, 21, 831–841.
- 18. Grases, F., Costa-Bauza, A., & Garcia-Ferragut, L. (1998). Biopathological crystallization: A general view about the mechanisms of renal stone formation. *Advances in Colloid and Interface Science*, 74, 169–194.
- 19. Grases, F., Costa-Bauza, A., Ramis, M., Montesinos, V., & Conte, A. (2002). Simple classification of renal calculi closely related to their micromorphology and etiology. *Clinica Chimica Acta*, 322, 29–36.
- 20. Stoller, M., & Meng, M. (2007). *Urinary stone disease: The practical guide to medical and surgical management*. Totowa: Springer.
- 21. Smith, R., Levine, J., & Rosenfeld, A. (1999). Helical CT of urinary tract stones. Epidemiology, origin, pathophysiology, diagnosis, and management. *Radiologic Clinics of North America*, *35*, 911–952.
- 22. Smith, R., & Varanelli, M. (2000). Diagnosis and management of acute Ureterolithiasis: CT Is truth. *Radiologic Clinics of North America*, 175, 3–6.

References 125

23. Mettler, A., Huda, W., Yoshizumi, T., & Mahesh, M. (2008). Effective doses in radiology and diagnostic nuclear medicine: A catalog. *Radiology*, 248, 254–263.

- 24. Scherer, K., et al. (2014). Bi-directional x-ray phase-contrast mammography. *PLos One*, 9, 93502.
- 25. Koehler, T., Engel, K., & Roessl, E. (2011). Noise properties of grating-based X-ray phase-contrast computed tomography. *Medical Physics*, 38, 106–116.
- Tapfer, A., et al. (2012). Experimental results from a preclinical X-ray phase-contrast CT scanner. Proceedings of the National Academy of Sciences, 109, 15691–15696.
- 27. Stoller, M., & Meng, M. (2007). *Urinary stone disease: The practical guide to medical and surgical management chapter 5: structure and compositional analysis of kidney stones*. Totowa: Humana Press.
- 28. Krafft, C., Steiner, G., Beleites, C., & Salzer, R. (2009). Disease recognition by infrared and Raman spectroscopy. *Biological and Medical Physics, Biomedical Engineering*, 2, 13–28.
- 29. R Core Team. R. (2014). A language and environment for statistical computing. Vienna: R Foundation for Statistical Computing.
- 30. Robin, X., Turck, N., Hainard, A., Tiberti, N., & Lisacek, F. (2011). pROC: an open-source package for R and S+ to analyze and compare ROC curves. *BMC Bioinformatics*, *12*, 77.
- 31. Woodard, H., & White, D. (1986). The composition of body tissues. *The British Journal of Radiology*, 59, 1209–1218.
- 32. Dance, D. (1990). Monte carlo calculation of conversion factors for the estimation of mean glandular breast dose. *Physics in Medicine and Biology*, *35*, 1211–1219.
- 33. Dance, D., et al. (2000). Additional factors for the estimation of mean glandular breast dose using the UK mammography dosimetry protocol. *Physics in Medicine and Biology*, 45, 3225.

Chapter 9 Summary and Outlook

There can be life after breast cancer. The prerequisite is early detection.

Ann Jillian

9.1 Summary of Results

9.1.1 Diagnostic Merit of Phase-Contrast Mammography

The work presented here was carried out in order to investigate the diagnostic merit which arises from phase- and scatter-sensitive mammography, and to answer the question whether phase-contrast mammography is a suitable candidate as a future screening modality.

At first, a compact setup—similar in design to a conventional mammography system—was specifically constructed for large field-of-view radiography and built from scratch within a laboratory environment. Subsequently, the mammolib package was developed which allows the retrieval of comprehensive full-field phase-contrast mammograms.

Ensuing from this, a case study investigating four freshly dissected abladates was conceived and carried out. Here, we could successfully verify that phase-contrast mammography is capable of outperforming conventional mammography at the detection and delineation of both cancerous and benign breast features, including tumor masses, micro-calcified structures, tumor strands and cystic changes. For certain indications, such as small tumor nodules, phase-contrast mammography even prevailed MRI in terms of detection sensitivity and spatial resolution. All of our findings were confirmed by histopathological work-up. We further carved out that phase-contrast mammography profits from both a superior depiction of fine features provided through the differential phase signal, additionally being extremely sensitive towards ultra-small calcifications and cellular changes within the dark-field channel.

In summary, the results of the case study strongly indicate that phase-contrast mammography yields immense potential in the enhancement of early tumor detection, which would be most noticeable in the group of young patients.

To prevent a potential over-diagnosis of microcalcifications due to the subresolution sensitivity of dark-field radiography, we then proposed a tool for the dose-compatible assessment of calcification clusters: we found that the comparison of global absorption and scattering characteristics does indeed enable a classification of the inherent micro-morphology of calcifications as ultra-fine, fine, pleomorphic and coarse structured. Our investigations further demonstrated that a chemically-based differentiation as proposed by recent literature is unjustified. Finally, we showed that the determined micro-structure may be an indicator for early tissue malignancy, which yields the potential to refine conventional microcalcification grading as well as reducing the number of invasive follow-up procedures.

Our study was conducted under the aspect of relying on a diagnostically meaningful imaging sensitivity, as we observed that the female breast can comprise malignant features, which exhibit a highly anisotropic imaging contrast in both the phase-contrast and dark-field channel. Therefore a bi-directional scanning approach was implemented into the work-flow, additionally enabling the retrieval of absolute artefact-free phase mammograms.

9.1.2 Clinical Compatibility of Phase-Contrast Mammography

With the ultimate goal of adjusting phase-contrast mammography to clinical requirements, the laboratory setup was continually optimized throughout this thesis. Improvements included, among others, a dose-saving arrangement of the breast and phase grating and the implementation of a breast-equivalent absorber in the flat-field. As a consequence, we were able to conduct the very first dose-compatible phase-contrast mammograms (2.2 mGy) at a medically reasonable sample compression, additionally meeting the image quality criteria of clinical mammography. We further proposed a fusion algorithm, which enables a comprehensive presentation of the trimodal data, compatible with clinical routine. Finally, by accomplishing the very first phase-contrast tomosynthesis measurements of fresh mastectomies, we verified that the dark-field signal is facilitating depth resolution, by providing complementary information in the discrimination of breast vessels and microcalcifications.

Figure 9.1 visually summarizes the motivation and outcome of our study: within the conventional ex-vivo mammogram (Fig. 9.1a), obtained with a clinical state-of-the-art scanner, multiple small tumor nodules remain undetected by the radiologists, being superimposed by dense breast tissue as typically encountered in the examination of young woman. In contrast, the fused mammogram obtained with phase-contrast mammography provides the radiologists with a superior detection quality of all three tumor nodules (green frame) at a single glance. At the same time it offers a high image acutance (red frame), without losing the typical absorption-character of conventional images (blue frame).

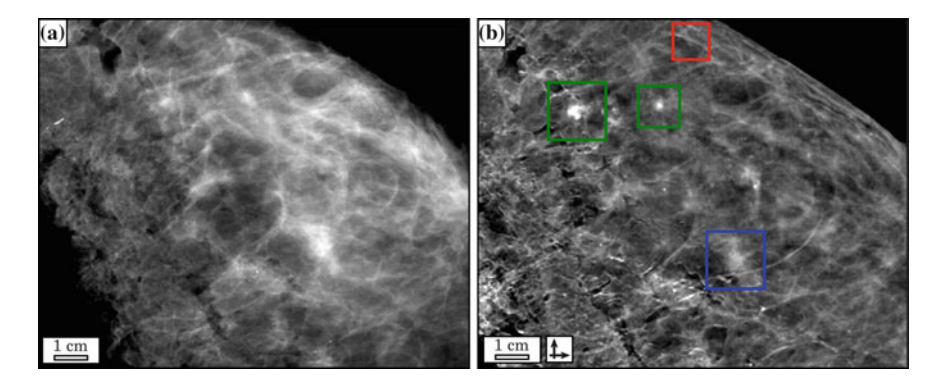


Fig. 9.1 Exemplary case study summarizing the motivation and potential outcome associated with phase-contrast mammography. a Conventional, ex-vivo mammogram obtained from a clinical state-of-the-art scanner. Note that tumor nodules are superimposed by anatomical noise, i.e. dense breast tissue, which renders an unambiguous detection of the latter impossible. **b** Mammogram fused from the experimental absorption, differential phase and dark-field signals, providing a superior depiction of the three tumor nodules (*green framed*) as well as fine tissue strands (*red framed*), while maintaining the typical absorption-character of conventional mammography (*blue framed*). For an in-depth analysis find Chap. 5

9.1.3 Renal Stone Assessment via X-Ray Dark-Field Radiography

With the goal of addressing a major shortcoming present in clinical renal diagnostics, we elaborated on a potential application of dark-field radiography for kidney stone assessment. Hereby, information on the morphological and chemical properties of a stone in question are simultaneously assessed by the dark-field and absorption channel, respectively. By combining both parameters, a significant enhancement in the differentiation of renal stones as well as the detection of radio-lucent calculi could be obtained. By implementing an easy visual discrimination tool for uric acid vs. calcium oxalate stones, while additionally repeating our results with a preliminary abdomen phantom, clinical transferability of X-ray dark-field radiography could be demonstrated.

9.2 Current Limitations and Future Challenges

Many challenges associated with phase-contrast mammography have been overcome during this thesis. However, some major shortcomings remain, which prohibit an immediate development of a clinical system. Therefore they are discussed in the following:

- 1. The current field-of-view is limited to approximately 10 cm round, contingent on the fact that gratings can not be routinely produced in larger dimensions. With the currently available gratings, an undesired scanning of the breast would be mandatory, which however is incompatible with patient comfort.
- 2. Until now, gratings are mostly fabricated on planar substrates, which leads to a pronounced shadowing, i.e. photon starving, at the edges of the source and analyser gratings in the case of beam divergence. Besides, the interferometric visibility is decreased in the outer regions of the gratings, due to a "flattening" of the grating profile seen by strongly inclined X-rays. Considering a large field-of-view application in combination with the stringent dose requirements as present in clinical routine, sufficient image quality is yet unachievable at the outer margins of the breast.

Current research associated with grating fabrication is centred on tackling these issues. This implies the production of large field-of-view gratings via stitching/tiling of the latter [1]. Further, to adapt the cone-beam geometry of compact interferometers and therewith provide an uniform illumination/energy spectrum throughout the overall field-of-view, the fabrication of gratings on bended substrates is industriously investigated [2, 3]. It is worth mentioning that a preliminary slit-scanning system does exist, which utilizes a fringe scanning approach and therefore only requires oblong plain gratings [4].

3. In the case of diagnostic applications, which demand a high spatial resolution and accuracy in the retrieval of phase and dark-field signal, the phase-stepping approach is still preferred over single-shot and fringe scanning techniques. Considering image acquisition times of 5 s per projections, this would result in scan times of several minutes in the case of tomosynthesis, incompatible with patient comfort.

Interlaced phase-stepping approaches are available for phase-contrast CT, that may also allow a parallelization of phase-stepping and tomosynthesis image acquisition to a certain extend [5, 6]. Besides, note that Miao, H. et al. recently reported on a motionless, electromagnetic phase-stepping procedure that can emulate mechanical phase-stepping, while additionally decreasing scan times [7].

4. As demonstrated in this work, phase-contrast mammography requires to be operated in an at least bi-directional manner to secure a diagnostically meaningful detection sensitivity. In practice, this could be achieved by a mutual rotation of all three gratings, however concerns arise with respect to system design and stability.

Note that the aforementioned challenge is obsolete when using two-dimensional gratings, which per se offer an isotropic imaging sensitivity. However, a 2D-structured illumination generally requires a substantially increased number of exposures. Contingent on the fact that the interference pattern has to be sampled in two dimensions, thus alternative linear phase-stepping approaches have been reported [8, 9]. Besides,

anticipating a broad availability of photon-counting detectors in near the future, a splitting of imaging dose into multiple projections would not intrinsically imply an accumulation of photon noise [10].

5. Finally, grating-based imaging has an intrinsic drawback, namely the circumstance that at least 50 % of all dose relevant photons are absorbed by the analyser grating. This is of immense importance considering the ongoing discussion, whether screening mammography is artificially inducing pathological changes within the breast by delivering an unacceptable life-time dose [11].

This is no death warrant for clinical, phase-contrast mammography per se, since phase-contrast imaging offers strongly enhanced contrast even at very hard dose-sparing X-rays [12]. Further, an optimal combination of the complementary trimodal data may provide depiction of essential image content at much decreased imaging doses [13].

9.3 Outlook and Next Steps

As illustrated in this study, phase-contrast mammography definitively yields the potential to replace conventional mammography and overcome its low sensitivity in the "problematic" group of young patients. Besides it may increase the detection quality of early (pre)-cancerous tissue abnormalities, to finally decrease breast cancer mortality rates. Currently it is the only imaging technique conceivable, which meets the general requirements of a screening modality, being operatable in radiographic imaging mode without the need for contrast agents. While MRI and sonography are routinely used for high-risk patients, most experts currently consider both unsuitable as a general screening modality, being too intensive in terms of finical and temporal effort. Note that a recent proof-of-principle study by Kuhl, C. et al. suggests an abbreviated MRI protocol, consisting of only one pre- and one post-contrast acquisition, by which MRI could be adapted to routine breast cancer screening [14].

Nevertheless, phase-contrast mammography yields one big advantage in comparison to other novel imaging approaches. In a potential clinical implementation, phase-contrast mammography would be compatible with the existing work-flow, data pool and education of radiologists, since intrinsically providing the conventional absorption image.

However, considering that the clinical market is inert with respect to innovations—this gets obvious when following the history of tomosynthesis—a direct implementation of phase-contrast mammography is currently unlikely. Prior to this, mostly three remaining questions have to be answered.

Open questions

- Is the production of two-dimensional, bended and large field-of-view gratings on an optically thin substrate practicable?
- Is the gain in diagnostic sensitivity outweighing the overhead in imaging dose, technical and finical effort accompanied by phase-contrast mammography?
- Is phase-contrast mammography specific? More precisely, will the detection of ultra-small calcifications not lead to a hopeless overdiagnosis and over-treatment in clinical routine?

In order to address these concerns, in particular the latter cases, the development of a phase-contrast radiography unit, specifically for the investigations of mass excision, would be expedient. Within an ex-vivo framework a large amount of specimen could be routinely investigated, with the advantage of providing enough data for significant reader studies. Further, the investigated sample cohort would comprise medical indications of both benign and malignant nature, by which the specificity of phase-contrast imaging could be evaluated. Moreover, samples could be placed in formalin during examination, which would allow a reduction of image artefacts so far corrupting many of the phase-contrast and dark-field mammograms. Besides, knowledge could be gained which breast features are best detected in which image channels. Thereby, the development of automatic image fusion algorithms could be strongly promoted. Most importantly, ex-vivo radiography is not bound to clinical requirements with respect to scan time, dose and patient comfort, which would significantly shorten the lead time of a potential implementation. First feasibility studies of investigating excised tissue with phase-contrast radiography haven been carried out recently. Figure 9.2 shows a tumor excision with sonographically-guided wire marking and inconspicuous radiographic finding embedded within formalin. In accordance

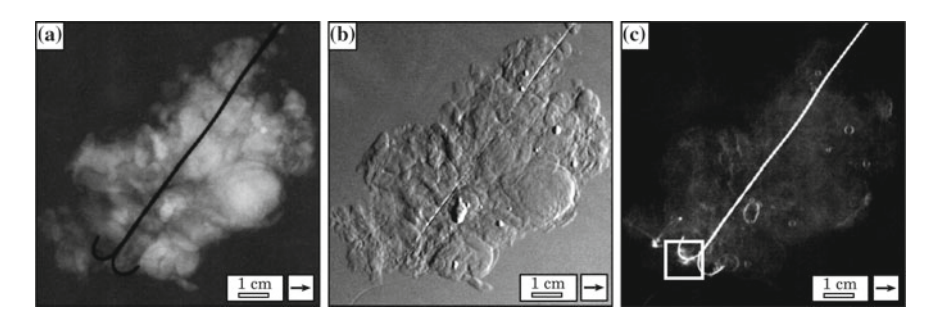


Fig. 9.2 *Preliminary phase-contrast radiography of a tumor excision.* Experimental absorption (a), differential phase (b) and dark-field contrast mammography (c) of a tissue excision embedded in formalin, with sonographically-guided wire marking of the tumorous volume. While the absorption channel shows an inconspicuous finding, highly scattering regions are visible (*white framed*) within the dark-field channel, indicating a perfusion of the tumor with highly dispersed calcium grains

with the clinical examination, the experimental absorption radiogram (Fig. 9.2a) does not show any malignant features. Within the dark-field channel (Fig. 9.2c), however, strongly scattering areas, closely situated to the marked volume, are revealed and indicate a perfusion of the tissue with fine malignant microcalcifications.

Finally, I personally consider phase-contrast mammography as the most promising approach currently investigated and consider the development of a radiograph as indispensable to further progress phase-contrast mammography into a clinical routine.

References

- Meiser, J., et al. (2014). Increasing the field of view of X-ray phase contrast imaging using stitched gratings on low absorbent carriers. *Proceedings of SPIE*, 9033, 903355.
- 2. Thuering, T., et al. (2011). High resolution, large field of view X-ray differential phase contrast imaging on a compact setup. *Applied Physics Letters*, 99, 041111.
- 3. Revol, V., et al. (2011). X-ray interferometer with bent gratings: towards larger fields of view. *Nuclear Instruments and Methods A*, 648, 302–305.
- Koehler, T., et al. (2015). Slit-scanning differential X-ray phase-contrast mammography: proofof-concept experimental studies. *Medical Physics*, 42, 1959–1965.
- Zanette, I., Bech, M., Pfeiffer, F., & Weitkamp, T. (2011). Interlaced phase stepping in phasecontrast X-ray tomography. *Applied Physics Letters*, 98, 094101.
- Xi, Y., & Zhao, J. (2013). Fast grating-based X-ray phase-contrast tomosynthesis. EMBC, 35, 2320–2323.
- Miao, H., et al. (2013). Motionless phase stepping in X-ray phase contrast imaging with a compact source. PNAS, 110, 19268–19272.
- 8. Zanette, I., Weitkamp, T., Donath, T., Rutishauser, S., & David, C. (2010). Two-dimensional X-ray grating interferometer. *Physics Review Letters*, 105, 24810.
- 9. Harmon, K., Bennett, E., Gomella, A., & Wen, H. (2014). Efficient decoding of 2D-structured illumination with linear phase stepping in X-ray phase contrast and dark-field imaging. *PLoS One*, 9, e87127.
- Taguchi, K., & Iwanczyk, J. (2013). Vision 20/20: single photon counting X-ray detectors in medical imaging. *Medical Physics*, 40, 100901.
- 11. Mettler, F., et al. (1996). Benefits versus risks from mammography: a critical reasessment. *Cancer*, 77, 903–909.
- 12. Sarapata, A., et al. (2015). Quantitative imaging using high-energy X-ray phase-contrast CT with a 70 kVp polychromatic X-ray spectrum. *Optics Express*, 23, 523–535.
- 13. Zhao, Y., et al. (2012). High-resolution, low-dose phase contrast X-ray tomography for 3D diagnosis of human breast cancers. *PNAS*, 109, 18290–18294.
- Kuhl, C., et al. (2014). Abbreviated breast magnetic resonance imaging (MRI): first postcontrast subtracted images and maximum-intensity projection - a novel approach to breast cancer screening with MRI. *Journal of Clinical Oncology and Research*, 32, 2304–2310.

Appendix A Supplementary Movies

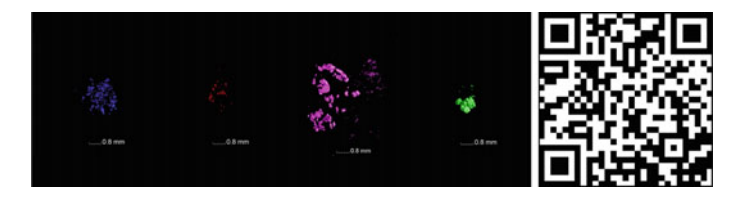


Fig. A.1 Supp. Mov. 1. From left to right Volumetric micro-CT rendering of breast microcalcification clusters with ultra-fine, fine, pleomorphic and coarse microtexture. Available: https://www.youtube.com/watch?v=Xb_ol-pJQDo



Fig. A.2 Supp. Mov. 2. From left to right Absorption, phase and dark-field contrast tomosynthesis of a formalin-fixed lizard. Note the superior depiction of the scales and the organs in the phase and dark-field channel, respectively. Available: https://www.youtube.com/watch?v=A8A52_KvSQE

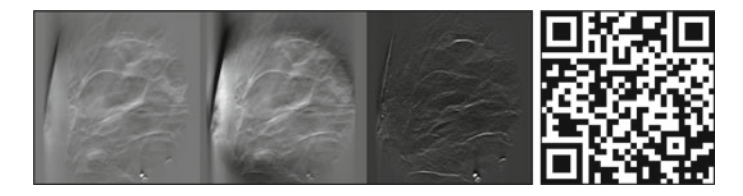


Fig. A.3 Supp. Mov. 3. From left to right Absorption, phase and dark-field contrast tomosynthesis of a freshly dissected mastectomy sample. Note the highly discriminative depiction of fibrous tissue strands within the dark-field channel. Macrocalcifications in the bottom of the field-of-view. Available: https://www.youtube.com/watch?v=zAk5hag6XY4

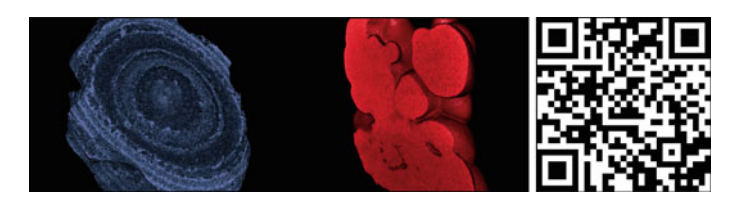


Fig. A.4 Supp. Mov. 4. From left to right Volumetric micro-CT rendering of an uric acid and calcium oxalate kidney stone. Note distinct growth rings in the case of the uric acid stone in comparison to a homogeneous growth pattern in the case of the calcium oxalate calculus. Available: https://www.youtube.com/watch?v=4e9oOZXsf98

Appendix B

Correct Quantitative Evaluation of X-ray Dark-Field Images for Microcalcification Analysis in Mammography

Abstract Note that the following section is a reprint of "Scherer, K. et al. Correspondence: Quantitative evaluation of x-ray dark-field images for microcalcification analysis in mammography. *Nat. Commun.* 5, 10863 (2016)". Together with the results presented Chap. 6 it disputes the main conclusion of a recent study by Wang, Z. et al. (2014) [1]. For reasons of consistency, variables are named as done by Wang, Z. et al.: the entities underlying this thesis, namely $\bar{\epsilon}$, $\bar{\mu}$, $\epsilon_{\rm eff}$ and $\mu_{\rm eff}$ (cf. Chaps. 6 and 8) are renamed to \hat{s} , $\hat{\mu}$, \bar{s} and $\bar{\mu}$, respectively.

Wang, Z. et al. have recently reported an X-ray grating-interferometer imaging approach for mammography combining the information from the X-ray absorption and small-angle scattering signal [1–4]. The authors claim that their approach can distinguish between type I (calcium oxalate dihydrate, $CaC_2O_4 \cdot 2H_2O$) and type II (calcium hydroxyapatite, $Ca_5(PO_4)_3(OH)$) microcalcifications. While such a differentiation would indeed be of great value for clinical mammography, several important deficiencies in the study put the main results and conclusions of the published article in question. The shortcomings in the published work became obvious, after we have unsuccessfully tried to reproduce the results in our own laboratory.

To discriminate between type I and type II calcifications, Wang, Z. et al. use the ratio

$$r = \frac{\hat{s}}{\hat{\mu}} = i \frac{\bar{s}}{\bar{\mu}} \frac{l}{l},\tag{B.1}$$

(Equation 4 in Wang, Z. et al. (2014) [1]) where \bar{s} is the length-independent, effective X-ray scattering parameter and $\bar{\mu}$ the effective X-ray attenuation coefficient. To test their hypothesis that type I and type II calcifications generally exhibit opposite absorption and scatter signals they present (supposedly confirming) experimental results for a phantom made from calcium oxalate dehydrate and calcium hydroxyapatite powder (to mimic type I and type II calcifications, Fig. 1 in Wang, Z. et al. (2014) [1]). However, while the obtained values may be correct for the specific powders used here, the experimental outcome cannot be generalized easily, as the

small-angle scattering signal does not only depend on the chemistry and density of the sample, but also strongly on the micromorphology of the powder (cf. Fig. 6.7). Previously published theoretical and experimental results clearly demonstrate this strong dependence of the scatter signal (and thus the r-value) on the average size of the microstructures [5–7]. Consequently, arbitrarily chosen powders (with respect to the average grain size) cannot reliably model microcalcifications in the human breast, if the actual size distribution is not taken into account (and matched to the one in a real human breast). More specifically, our calculations (based on Malecki, A. et al. (2012) [6]) even show that by varying the average size of the powders microstructures one can actually obtain arbitrary r-values, regardless of the actual chemical and density position. This is also reflected in a recent publication by Michel, T. et al. (2013) [8], which reports on a larger scattering signal in calcium oxalate dihydrate vs. calcium hydroxyapatite, contradicting phantom results of Wang, Z. et al. (2014) [1].

Secondly, but probably even more important, we have identified a major mistake in the analysis of the data from the real breast specimens (Fig. 3 and 5 in Wang, Z. et al. (2014) [1]), which render the main conclusions of the study highly questionable. In their evaluation of the r-value for various microcalcifications, Wang, Z. et al. have neglected the contribution of underlying breast tissue. Correctly, the r-value has to be written as

$$r_{mt} = \frac{\hat{s}_m + \hat{s}_t}{\hat{\mu}_m + \hat{\mu}_t},\tag{B.2}$$

where the subscripts m and t denote contributions from the microcalcification and the tissue. While neglecting \hat{s}_t leads to a relatively small error in the r-value (as the scattering signal of tissue is relatively low), neglecting $\hat{\mu}_t$ leads to a large error and significantly falsifies the classification of the microcalcifications. Some exemplary results from a corresponding experiment in our lab (Fig. B.1) highlight the issue. The blue and the red points represent pixels with \hat{s}_m and $\hat{\mu}_m$ values of two different microcalcifications, and they appear as a cloud with a slope corresponding to the r_m -value of this particular calcification. If now the contributions of the tissue (\hat{s}_t and $\hat{\mu}_t$) are neglected in the analysis, one obtains a slope (r-value) for the two clusters of $r_{(1,Wang)} = r_{(1,mt)} = 0.34 \pm 0.02$ and $r_{(2,Wang)} = r_{(2,mt)} = 0.35 \pm 0.01$, a very similar and small value in both cases (in agreement with Figs. 3 and 5 in Wang, Z. et al. [1]). However, when the contributions from the tissue are now correctly subtracted, the real calcification-values (matching the data cloud) become $r_{(1,m)} =$ 6.63 ± 0.18 and $r_{(2,m)} = 2.48 \pm 0.07$. This means that Wang, Z. et al.'s analysis would have yielded an error of almost 2000% for r_1 and 700% for r_2 , with the consequence of large classification errors, as demonstrated by the example above (before correction: $r_1 \approx r_2$, after tissue correction: $r_1 \gg r_2$). Because of this error in the analysis, the data presented by Wang, Z. et al. can barely be associated with the calcifications themselves but instead is mostly dominated by the attenuation of the breast tissue $(\hat{\mu}_t \gg \hat{\mu}_m)$, which renders a correct classification according to the hypothesis untenable. Accordingly, the presented r-values are small (0.3 < r < 1.0), whereas the real values obtained by a correct analysis show scatter dominated ratios (1.2 < r < 10).

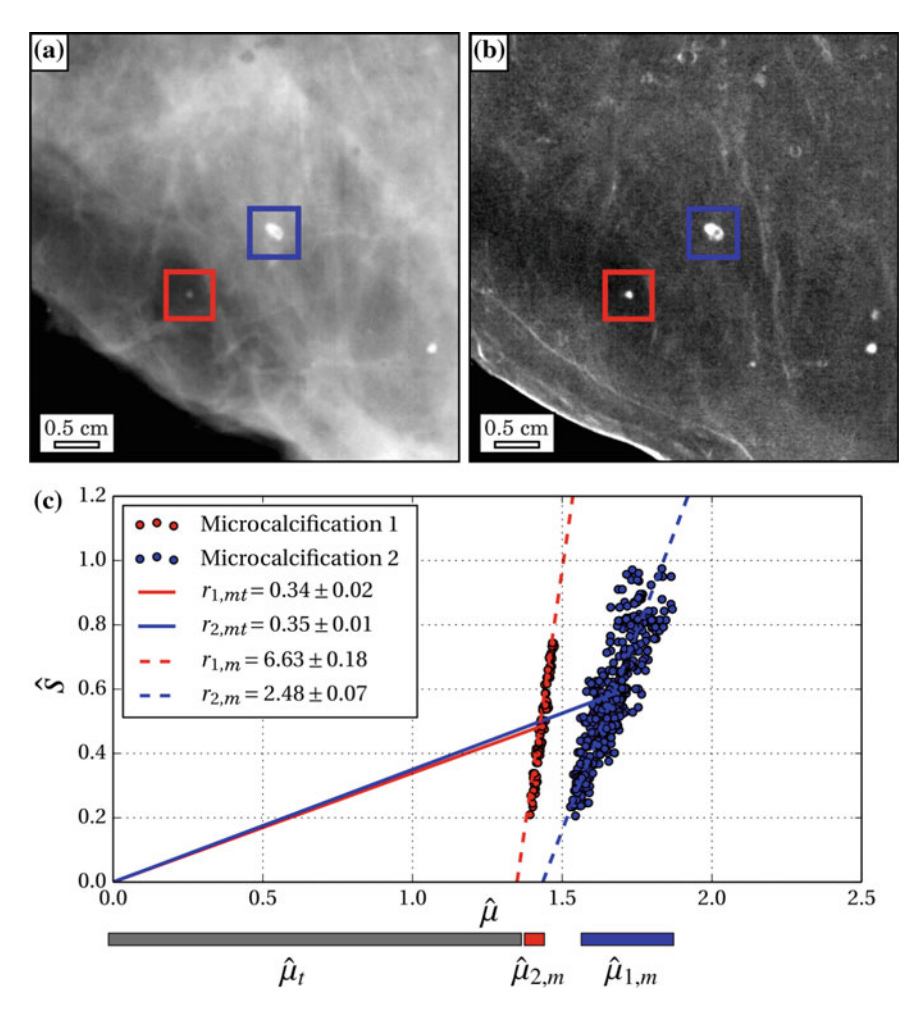


Fig. B.1 Correct quantitative evaluation of microcalcification analysis in X-ray dark-field mammography. **a** Experimental absorption and **b** dark-field mammogram of a freshly dissected breast abladate with microcalcifications. **c** Scatter plots comparing the absorption $\hat{\mu}_m$ to scattering power \hat{s}_m of two exemplary microcalcifications cluster, as indicated by the *blue* and *red frame* in **a** and **b**, respectively. A strongly falsified r-value is obtained (r_{mt}) if contributions of the underlying tissue are neglected in the analysis, since $\hat{\mu}_t \gg \hat{\mu}_m$

In summary, we can conclude that the main claim of this article, namely the successful classification of different microcalcifications into type I and type II by this approach, is unjustified. Both, the experimental results of the phantom and the ones for the human breast samples neglect major contributions to the image signal, and therefore render the main claim and specific experimental results and conclusions presented in this published study highly questionable.

Finally, we note that Wang, Z. et al. have neither discussed nor referenced related and partially contradicting, published results by other groups, in which detailed calculations and experimental verifications of the dependence of the scattering parameter on the sample microstructure are shown [5–8]. Furthermore, the authors have disregarded the fact that the use of the different ratios between attenuation and scattering parameters has already been demonstrated for material or tissue discrimination [9, 10].

References

- 1. Wang, Z., et al. (2014). Non-invasive classification of microcalcifications with phase-contrast X-ray mammography. *Nature Communications*, *5*, 3797.
- 2. Pfeiffer, F., Weitkamp, T., Bunk, O., & David, C. (2006). Phase retrieval and differential phase-contrast imaging with low-brilliance X-ray sources. *Nature Physics*, 2, 258–261.
- 3. Pfeiffer, F., et al. (2008). Hard-X-ray dark-field imaging using a grating interferometer. *Nature Materials*, 7, 134–137.
- 4. Stampanoni, M., et al. (2011). The first analysis and clinical evaluation of native breast tissue using differential phase-contrast mammography. *Investigative Radiology*, 46, 801–806.
- 5. Yashiro, W., Terui, Y., Kawabata, K., & Momose, A. (2010). On the origin of visibility contrast in X-ray Talbot interferometry. *Optics Express*, 18, 16890.
- Malecki, A., Potdevin, G., & Pfeiffer, F. (2012). Quantitative wave-optical numerical analysis
 of the dark-field signal in grating-based X-ray interferometry. Europhysics Letters, 99, 48001.
- 7. Lynch, S., et al. (2011). Interpretation of dark-field contrast and particle-size selectivity in grating interferometers. *Applied Optics*, 50, 4310–4319.
- 8. Michel, T., et al. (2013). On a dark-field signal generated by micrometer-sized calcifications in phase-contrast mammography. *Physics in Medicine and Biology*, *58*, 2713–2732.
- 9. Bech, M., et al. (2010). Quantitative X-ray dark-field computed tomography. *Physics in Medicine and Biology*, 55, 5529–5539.
- Schleede, S., et al. (2012). Emphysema diagnosis using X-ray dark-field imaging at a laserdriven compact synchrotron light source. PNAS, 109, 17880–17885.